# Stony Brook University

# Rotation and Evolution of A and F stars

A Dissertation Presented

by

**Jinmi Yoon**

to

The Graduate School

in Partial Fulfillment of the Requirements

for the Degree of

**Doctor of Philosophy**

in

**Physics**

Stony Brook University

**December 2008**

**Stony Brook University**

The Graduate School

**Jinmi Yoon**

We, the dissertation committee for the above candidate for the
Doctor of Philosophy degree, hereby recommend
acceptance of this dissertation.

**Dr. Deane M. Peterson - Dissertation Advisor**
**Associate Professor, Department of Physics and Astronomy**

**Dr. Frederick M. Walter - Chairperson of Defense**
**Professor, Department of Physics and Astronomy**

**Dr. Gerald Brown**
**Distinguished Professor, Department of Physics and Astronomy**

**Dr. John Thomas Armstrong**
**Navy Prototype Optical Interferometry Principal Investigator,**
**Naval Research Laboratory**

This dissertation is accepted by the Graduate School.

**Lawrence Martin**
**Dean of the Graduate School**

Abstract of the Dissertation

# Rotation and Evolution of A and F stars

by

**Jinmi Yoon**

**Doctor of Philosophy**

in

**Physics**

Stony Brook University

**2008**

Rapid rotation can significantly affect stellar evolution. Perhaps more importantly, rapid rotation obscures the interpretation of the measurements of the intrinsic properties of the star. Thus, it is important to determine the actual rotational velocity of a star, whereas generally only the line of sight projection is known. Reported here are three investigations of the effects of rotation using high resolution spectroscopy and high angular resolution interferometry.

First, a list of potential targets and a series of catalogs of potential calibrators for existing ground-based interferometry were produced. A and F stars are subject to distortion if rotating rapidly, which can add significant uncertainty in interferometric measurements if used as calibrators. The catalogs characterize these uncertainties.

Next, the discovery that Vega is a rapidly rotating pole-on star creates uncertainties over its assumed age and composition. A full spectral synthesis with the Roche model derived from NPOI interferometry demonstrates that the temperature gradient over the surface produces a variety of peculiar line shapes in addition to the flat-bottomed line profiles previously recognized. ELODIE spectra show excellent agreement with the calculations if an additional 10 $\mathrm{km\,s^{-1}}$ of macroturbulence is added to the predicted spectra. The suggestion that Vega has the peculiar composition of a $\lambda$ Boo star is also confirmed. Rapid rotation argues strongly that the star is well mixed. Hence the deduced composition is a bulk property, not limited to its surface, leading to a significant revision of Vega's mass and age as estimated from evolutionary calculations.

Lastly, simultaneously fitting the interferometric and spectroscopic observations with a Roche model providing the maximum possible number of constraints on the model gives a more direct determination of Vega's physical characteristics, particularly its mass. These calculations confirm independently that Vega has a much lower mass, $2.135 \pm 0.074\,\mathrm{M_\odot}$, than generally assumed. This estimated mass strongly supports that Vega is metal poor throughout (Z$\sim$0.008), suggesting the star would have to be more massive by more than $4\sigma$ to be consistent with a solar composition. This suggests it was formed that way and is much older ($471 \pm 57\,\mathrm{Myr}$) as previously assumed. In addition, assuming a uniform composition equal to that derived for the surface and the luminosity and radius obtained here we can derive more precise esti-

mates of Vega's age, $455 \pm 13\,\mathrm{Myr}$, and mass $2.157 \pm 0.017\,\mathrm{M}_{\odot}$, by appealing to the interiors calculations as done in the second investigation.

To God, My Lord

# Contents

# List of Figures

# List of Tables

# Acknowledgements

I sincerely thank my advisor, Prof. Deane M. Peterson, for his guidance in my Ph.D. research. Without his advice, encouragement, and guidance, this research would not have been possible. I have always appreciated his enthusiasm, willingness, and kindness as well as the tremendous support he has showed me throughout my graduate career. I am also thankful to Prof. Fred Walter, Prof. Gerald Brown, Dr. J. Tom Armstrong for serving on my thesis committee and for all their comments and suggestions during each one of my regular thesis update meetings for the past 3 years, especially to Dr. Armstrong who came all the way from Washington D.C. each time. Their feedback and suggestions have led to many improvements in my thesis work as well as the thesis itself. I thank Prof. Michal Simon for all his support and advice since I first arrived at Stony Brook. He has always been a source of encouragement. I also thank Robert J. Zagarello for his contributions to this research project through programming and also for his encouragement. I thank Dr. Robert L. Kurucz for providing the ATLAS12 models and Vega's spectral atlas used in this work and our extensive discussions over our work.

I am glad to have met many people through the astronomy group during my years at Stony Brook. I am thankful to Bill Sherry for helping me with various programming questions and for his advice on research. I also would like to thank my fellow colleagues of the astronomy group Gail Schaefer, Kyunjin Kwak, Chad Bender, Angeliki Pollatou-Field, Tatjana Vivilkin, Stefan Gromoll, Jackie Faherty, Chris Malone, Bryan Kim, Josh Schlied, Yeunwhan Lim, Aaron Jackson, Mark Foley, Lisseth Gavilan, Brendan Krueger for their camaraderie, and for sharing thoughts and fun conversations with me.

I would like to thank my classmates Keunyoung Kim and Sungtae Cho who have helped me endure my first two years of coursework. I am also grateful for my long time friends at Stony Brook, Yeona Kang, Eunbee Cho, and Soyon Kim and at Korea, Eunhee Kim. Through their friendship, it has made even the most difficult times of graduate life bearable.

I sincerely thank my family: all my sisters and brothers in Korea and especially my parents Seungho Yoon and Ohkjah Song. Without my parents'

constant support this research would not have come to completion. I also give a sincere thanks to my husband Tan.

My research was supported by the Naval Research Laboratory and the National Science Foundation.

# Chapter 1

# Introduction

Stellar rotation has been studied for a long time, however the advances are rather slow. The studies of rotation and evolution have been closely associated. Rotation was even used as a major test of the stellar evolution soon after the discovery (Sandage & Schwarzschild, 1952) that stars evolve off the main sequence. The theory of stellar evolution has been very successful, and rotation has been generally considered only a second order effect. However, there are a growing number of discrepancies between current models and observations. The observations suggest that the role of rotation has been greatly underestimated (Maeder & Meynet, 2000).

Many studies have been made of the physical effects of rotation, including meridional circulation, diffusion processes, mass loss, and differential rotation. Most of these studies have focused on the rotation of massive upper main sequence stars combined with mass loss, because the structure of those stars can be strongly influenced by the rotation (Collins, 1970).

One of the limitations to date has been the lack of knowledge of the actual rotational velocities. We only know projected rotational velocity, $v_{eq} \sin i$, and generally do not know the inclination angle, $i$ independently.

Recent advances in the study of the effect of rotation on physical properties have come from newly available high resolution, high signal-to-noise (SNR) spectroscopy. One study (Gulliver, Hill, & Adelman, 1994) revealed that Vega is a nearly pole-on, rapidly rotating star although subsequently the same authors (Hill, Gulliver, & Adelman, 2004) have revised the velocity downward. Even though the high resolution spectroscopy reveals the signature of rapid stellar rotation, it is not a rigorous way to the rotation velocity because one still lacks an independent measurement of the inclination.

However, the development of high angular resolution long baseline interferometers has facilitated the studies of rotating stars because high angular resolution interferometry is capable of obtaining the inclination angle of a star

directly. The Navy Prototype Optical Interferometer (NPOI, Armstrong et al., 1998) and the Center for High Angular Resolution Astronomy (CHARA, ten Brummelaar et al., 2005) recently confirmed through the measurements of triple phase (Peterson et al., 2006b) and squared visibility amplitude (Aufdenberg et al., 2006) respectively, that Vega is a rapidly rotating, nearly pole-on star. Also Altair, already known as a rapid rotator, has been studied using the NPOI (Peterson et al., 2006a) and the CHARA array (Monnier et al., 2007).

The approach here is to combine as many different kinds of data as possible towarding modeling a star. A simultaneous analysis of interferometric data (squared visibility amplitudes and closure phases) with spectroscopic data (various spectral line profiles) provides the maximum number of possible constraints on the models and thus will give a more reliable determination for physical characteristics, especially stellar mass. Ultimately this must be done for many stars. Since we cannot observe the evolution of a specific rotating star, statistical studies of rotating stars at various stages of evolution are required.

The composition of this dissertation is as follows. A brief overview of stellar evolution of intermediate mass stars and the effect of simple rigid rotation on their figures and interferometric observables is given in the next chapter. In Chapter 3 we investigate A and F stars as possible calibrators for ground-based interferometry by estimating the size of the rotational effect on the visibility. This work was carried out in collaboration with D. Peterson, members of the Naval Research Laboratory, and R. Zagarello and reported in Yoon et al. (2006, 2007). Next, we produce a list of A and F star targets for the NPOI for observation of apparent oblateness and surface brightness asymmetry. The detailed calculations are described in Chapter 4. In the following chapter, we describe our spectroscopic study of the effect of rotation on Vega's spectrum and derive afresh its apparent chemical composition. This study was also undertaken with D. Peterson, NRL staff, and R. Zagarello and reported in Yoon et al. (2008). A simultaneous analysis of spectroscopy and interferometry for Vega is described in Chapter 6. We provide a brief summary of the dissertation and remark on possible the future work in Chapter 7.

# Chapter 2

# Theory of A and F stars

## 2.1 Theory of Rotating Stars

### 2.1.1 Roche Model

It is well known that stars earlier than F5 tend to rotate rapidly (Walker, 1965) and it is usually assumed that uniformly rotating Roche models are good approximations to the figures of such stars whose envelopes are radiative. In this case it is assumed that all the mass M is concentrated in a point at the center of the star. Under these assumptions, the centrifugal forces reduce the effective gravity according to the latitude thereby introducing deviations from sphericity (von Zeipel, 1924). The equipotential surface ($\psi(\theta)$), which involves gravitational and rotational terms, is then given by

$$\psi(\theta) = \frac{GM}{R(\theta)} + \frac{\Omega^2 R^2(\theta)\sin^2\theta}{2} = \frac{GM}{R_p}, \tag{2.1}$$

where $R(\theta)$ is the stellar radius at co-latitude $\theta$, G is the gravitational constant, $R_p$ is the polar radius, and $\Omega$ is angular velocity. The last equality is obtained by assuming a vanishing centrifugal term at the pole (Collins, 1963; Hardorp & Strittmatter, 1968). The effective surface gravity $g(\theta)$ (Collins, 1963) is given then by

$$|g(\theta)| = \sqrt{(\frac{GM}{R^2} - \Omega^2 R\sin^2\theta)^2 + (\Omega^4 R^2 \sin^2\theta\cos^2\theta)}. \tag{2.2}$$

By setting $\theta = 90^\circ$ (the equator) and substituting $R_{eq,B}$ into $R$ at critical rotation, $\Omega_c^2 = \frac{GM}{R_{eq,B}^3}$, where the gravitational force balances centrifugal force, Equation (2.2) reduces to a relationship between the polar radius and the

equatorial radius at breakup,

$$R_{eq,B} = \frac{3}{2} R_p. \tag{2.3}$$

### 2.1.2 von Zeipel Theory

For the Roche model to be useful, we need to be able to calculate emergent spectra. We assume the atmosphere can be approximated by plane parallel model atmospheres with local values of effective temperature $T_{eff}(\theta)$ and gravity $g(\theta)$. The effective temperature is given by

$$F(\theta) = \sigma T_{eff}^4(\theta) \tag{2.4}$$

where $F(\theta)$ is the local stellar radiative flux, and $\sigma$ is the Stefan-Boltzmann constant. According to von Zeipel (1924), the radiative flux at particular point on the surface is given by

$$F(\theta) = (const) \cdot |g(\theta)|. \tag{2.5}$$

The effective temperature is thus $T_{eff} \propto g(\theta)^\beta$, where $\beta = 0.25$ applies for radiative envelopes, and hence is defined over the surface with the specification of the effective temperature of the pole, $T_p$. Rapidly rotating upper main sequence stars display what is called "gravity darkening" due to this effect, in addition to the usual limb darkening. The von Zeipel theory has been successful in describing close binary systems, and recently has been tested in isolated, rapidly rotating stars (Peterson et al., 2006a,b; Aufdenberg et al., 2006; van Belle et al., 2006; Monnier et al., 2007).

Adding two angles to describe the viewing geometry, position angle (P.A., the projection of the rotational axis on the sky measured from the North through East), and inclination ($i$, the tilt of the rotational axis) completes the description of a rotating star. We use ATLAS model atmospheres (Kurucz, 1993, 2005) to calculate the surface brightness. The plane parallel approximation breaks down at the equator as rotation approaches breakup (Collins, 1963), so we limit our calculations from reaching critical angular velocity.

## 2.2 Interferometric Observables

The Roche model coupled with the von Zeipel theorem allows us to predict quantities measurable by an interferometer including those related to oblateness and surface brightness asymmetry. The interferometric observables are

the amplitude and the triple phase (also called closure phase) of the visibility of the surface brightness distribution on the sky. The complex visibility is the Fourier transform of the object's surface brightness distribution, $I_\lambda$ integrated perpendicular to the projected direction of the baseline (Born & Wolf, 1999). The visibility at a wavelength $\lambda$ is usually given by

$$V_\lambda(u,v) = |V_\lambda(u,v)| \exp(i\phi(u,v)) = \int_{-\infty}^{\infty}\int_{-\infty}^{\infty} I_\lambda(x,y) \exp(i2\pi(ux+vy))dxdy \tag{2.6}$$

where $(x, y)$ are coordinates on the projected on the plane of the sky and $(u = B_x/\lambda, v = B_y/\lambda)$ are the spatial frequency coordinates corresponding to $(x, y)$ where $B_x$ and $B_y$ are the projected baselines onto x and y coordinates. The quantity $|V_\lambda| = \frac{S_\lambda^{max} - S_\lambda^{min}}{S_\lambda^{max} + S_\lambda^{min}}$ is the visibility amplitude or modulation and $\phi$ is the phase of visibility, and $S_\lambda^{max,min}$ are the maximum and minimum values of the measured power. In practice, squared visibility amplitudes are measured, because these quantities can be corrected for statistical bias (Colavita, 1999).

Phases are particularly sensitive to any asymmetry in the intensity distribution of the object. If the object is centrosymmetric, the triple phase shows the "top hat" behavior because the visibility is then real and takes on positive and negative values while the amplitude is defined to be positive, thus the individual phases switch between 0°, or 180°. As has been known for some time (Jennison, 1958), the visibility phases summed over closed triangles of telescope apertures, the closure phase, is free from atmospheric phase effects although there is the loss of information. The closure phases also show the top hat behavior for centrosymmetric objects.

A differential phase is another measurable sensitive to asymmetric structure of the stars. This is calculated as the difference between phases on a single baseline as the baseline length or wavelength is changed. This is also free of atmospheric effects and residual instrumental effects are easily calibrated. It does not suffer so much information loss as closure phases.

## 2.3 Evolution of Intermediate Mass Stars

### 2.3.1 Rotation Effects on the Zero Age Main Sequence Stars

To study the evolution of uniformly rotating stars, we need know their true luminosity and polar radius. However, rotation affects a star's evolution to some extent. Studies (e. g., Sackmann, 1970) have shown that the deviation

of total luminosity and polar radius due to uniform rotation compared to the radius and luminosity of the corresponding non-rotating star is small on the Zero Age Main Sequence (ZAMS). For stars having $1.8M_{\odot} < M < 3.0M_{\odot}$ such as Vega or Altair these studies have shown that the changes in luminosity and polar radius due to rotation are less than 5.9% and 1.7% respectively (Sackmann, 1970). We obtain the total luminosity and radius that would apply to a non-rotating counterpart of the same mass by using Roche models to estimate the luminosity and polar radius of the rotating star and then make adjustments as required to allow for the changes to the interior structure (Peterson et al., 2006a). With the corrected luminosity and the radius, the other parameters of the non-rotating counterpart such as the mass can be estimated using evolutionary grids such as BASTI database[1].

While these corrections were well justified in the case of Altair (Peterson et al., 2006a) which was shown to be only slightly evolved off the ZAMS, the situation is cloudier for Vega which, as we shall see, is in the late phase of the core hydrogen burning, well off the ZAMS. Since no evolutionary tracks have yet been calculated for rapidly rotating stars in the $2M_{\odot}$ range, whether in uniform rotation or more generally accounting for angular momentum conservation (Meynet & Maeder, 1997) it is not clear what corrections apply to Vega's measured luminosity and polar radius to properly identify the corresponding non-rotating model. The ZAMS calculations show the corrections are small and we assume that continues to be true as these stars evolve. Hence we do not apply any corrections in the case of Vega when identifying the appropriate non-rotating models. Fortunately, as we will see, Vega appears to be rotating a bit slower than Altair in terms of its fractional angular rotation, and its fractional rotation would have been much slower than Altair when on the ZAMS, suggesting that we are not introducing serious uncertainties.

### 2.3.2 The Evolution of Non-rotating, Intermediate Mass Stars

We focus here on the evolution of the main sequence phase and the end of the main sequence phase of intermediate mass stars. The evolution of such stars has been described by Iben (1967) among others and summarized Carroll & Ostlie (2007). The evolution of intermediate mass stars on the main sequence is similar to that of the low mass stars, and is dominated by the fusion of hydrogen into helium in their cores. During core hydrogen burning, the temperature and pressure increase according to the ideal gas law, thus lu-

[1] `http://www.te.astro.it/BASTI/index.php`

minosity increases slightly along with radius (the phase from the ZAMS before the loop region in evolutionary tracks).

However, there is a significant difference between low mass and intermediate mass stars; the intermediate mass stars have a convective core due to the highly temperature dependent CNO reactions while the low mass stars are dominated by the less temperature-dependent pp chain and are not unstable to convection in their core. The convection zone continually mixes the material, thus keeping the core almost homogeneous because the convective turnover timescale is much shorter than the nuclear timescale.

When the mass fraction of hydrogen reaches about X = 0.05 in the core hydrogen burning effectively ceases and the entire star begins to contract, resulting in a decrease in radius. With the release of some gravitational potential energy due to this contraction, the luminosity increases slightly and the effective temperature increases. This stage of overall contraction is defined to be the end of the main sequence phase of evolution. The ignition of the hydrogen burning shell is quite rapid so the overlying envelope is forced to expand slightly by absorbing energy released from the shell, thus luminosity decreases briefly, and the effective temperature decreases. The overall contraction and the brief expansion cause the loop region in the evolutionary tracks shown in 2.1 and 2.2.

The luminosity produced during the hydrogen shell burning exceeds that during the hydrogen core burning so the luminosity continues to rise (the right side of the loop region of the evolutionary tracks). Some of the energy goes into a slow expansion of the envelope, resulting in the effective temperature decreasing slightly and the evolutionary track bends to the right. All the regions of evolutionary tracks described above are shown in Figures 2.1 and 2.2.

### 2.3.3 Evolutionary models

Many refinements have been added to stellar evolution calculations since the early detailed work by Iben. Those include better treatments of convection, improved nuclear reaction rates, more complete treatment of the equation of state, the inclusion, where applicable, of the effects of mass loss, and a more accurate accounting of the effects of chemical compositions. Not all stars are well described as having a solar composition, nor even a scaled-solar composition. Nevertheless, the evolutionary grids available in the literature are limited to essentially scaled-solar composition and to compositions where the $\alpha$-rich nuclei ("$\alpha$-enhanced") have been increased from solar by a constant factor (typically a factor of 4). In this dissertation we use primarily the "BASTI" grids (Pietrinferni, 2004) which provide the most detailed tab-

ulations for stars in this mass range with both scaled-solar and $\alpha$-enhanced compositions (Pietrinferni, 2006).

How stellar evolutionary tracks depend on the details of the compositions and the overall metallicities is of interest. Figure 2.1 shows the evolutionary tracks of the scaled-solar metal distribution models based on BASTI grids for three masses: 1.5, 2.0, and $2.4M_{\odot}$. Stars at all three masses have fully developed convective cores and show the looping topology where shell hydrogen burning commences. In addition, the effect of metallicity on stellar evolutionary tracks is also shown using three metallicities of Z =0.008, 0.01, and 0.02, all scaled-solar, the last corresponding to the solar mixture. It appears that a star with varying metallicity can mimic the evolution of different mass stars. As a result, masses inferred by locating a star within an evolutionary grid can be in error if an inappropriate metallicity is adopted. In turn, average metallicities can be determined if we can determine the luminosity, radius and mass of a star independently.

For sufficiently low metallicities (Z $<$ 0.002) scaled-solar compositions can not be distinguished from those with $\alpha$-enhanced compositions. For higher metallicities this degeneracy is lifted (Pietrinferni, 2006). One can see these effects in Figure 2.2, which shows the evolutionary tracks of a $2M_{\odot}$ star with different metallicities as well as different metal distribution models. So it is important to use appropriate metal distribution models. However, as we can also see in Figure 2.2, the evolutionary track of the scaled-solar model at Z=0.008 is very similar to that of the $\alpha$-enhanced model at Z=0.010 while the evolutionary tracks of solar metallicity are quite different from the tracks of the low metallicities. One concludes that the effect of the details of the mixture on evolutionary tracks is not nearly so significant as that of the overall metallicity on the evolutionary tracks.

## 2.4 Macroturbulence

The macroturbulence is first introduced here (as described in § 5.4.2) as being needed for matching the observed line profiles and is used as a free parameter in the models for Vega described in Chapter 6. This turbulence is distinguished from microturbulence as being produced by cells which are large enough to capture incoming photons. We assume the circulation currents induced by rapid rotation, subject to the corriolis effect, cause the large cells. Each such cell produces a complete spectrum which is displaced by Doppler shift corresponding to the local velocity in the cell. Lines broadened by macroturbulence are made shallower, however the broadening does not change the

total absorption (equivalent width) of the spectral lines unlike microturbulence (Gray, 2005). The spectrum broadened by macroturbulence can be obtained by convolving the spectrum without macroturbulence with a Gaussian at the appropriate dispersion. The theory of macroturbulence is not well developed so two simple approximations are considered here, namely isotropic macroturbulence and horizontal (velocities are perpendicular to the local normal) macroturbulence. In the latter case, the projected velocity dispersion has a view-angle dependence given by

$$\mathrm{V}_{Mac}(\mu) = \mathrm{V}_{Mac0} \cdot \sqrt{(1-\mu^2)} \tag{2.7}$$

where $\mathrm{V}_{Mac0}$ is a constant and $\mu$ is the cosine of the angle between the line of sight and the local normal. As Equation (2.7) shows, the broadening due to horizontal macroturbulence is maximum at the limb.

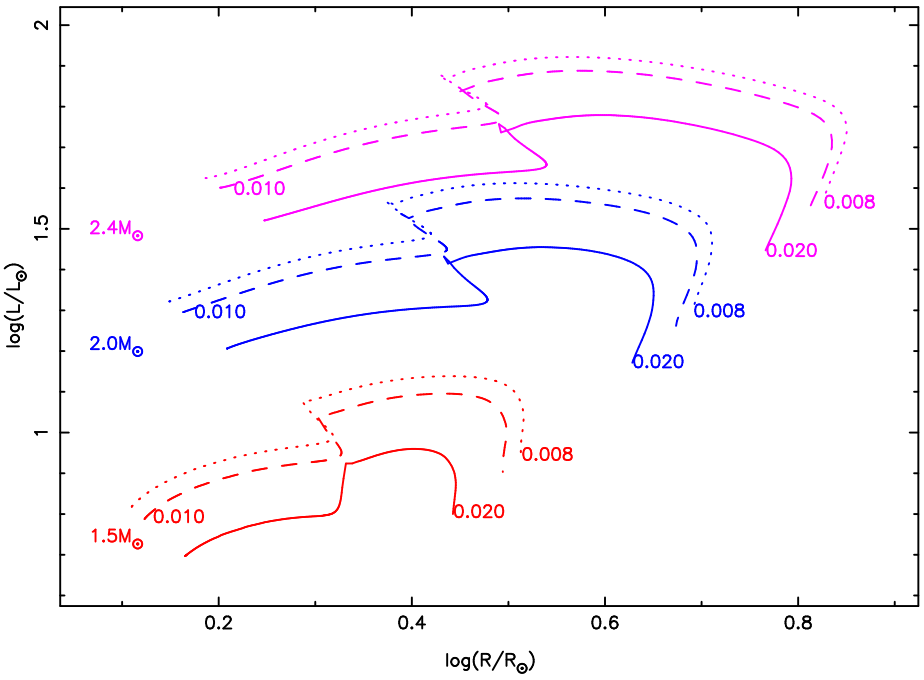


Figure 2.1 Shown are evolutionary tracks for M=1.5, 2.0, and 2.4$M_{\odot}$ (color-coded by red, blue and pink respectively) with Z = 0.008 (dotted lines), 0.010 (dashed lines), and 0.020 (solid lines) for scaled-solar metal distributions. The different metallicities can mimic the different mass stars. (Courtesy: Robert J. Zagarello)

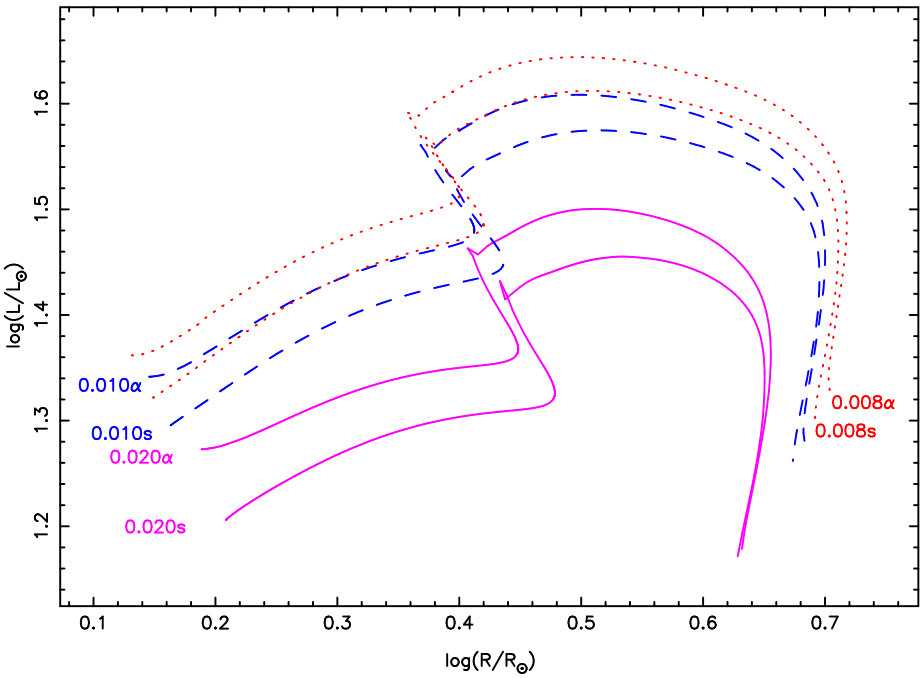


Figure 2.2 Plotted are evolutionary tracks for $M = 2.0M_{\odot}$ with Z = 0.008, 0.010, and 0.020 of both scaled-solar and $\alpha$-enhanced metal distributions. The solid lines, dashed lines, and dotted lines show the tracks of solar metallicity (Z=0.020), Z=0.010, and Z =0.008 respectively. The designations of "s" and "$\alpha$" mean scaled-solar and $\alpha$-enhanced models respectively. This shows how metallicity variations can affect mass determinations and that the details of the mixture (i. e., scaled-solar versus $\alpha$-enhanced) are not nearly so important. (Courtesy: Robert J. Zagarello)

# Chapter 3

# Early type stars as calibrators for ground-based interferometry

## 3.1 Introduction

A critical step in the practice of ground-based optical interferometry is the measurement of suitable calibrators (i. e., Mozurkewich et al., 2003). These allow compensation for various instrumental and atmospheric effects which reduce the measured fringe contrast. The ideal calibrator is bright (short of inducing non-linearities in the detector) and either has an accurately known visibility or a diameter which can be reliably estimated to be small. In the latter case, stars which are bright and have small angular diameters are necessarily high surface brightness objects, i. e., early type stars.

Early type stars bring their own problems. In practice the need to have calibrators relatively close to the science targets results in objects with larger diameters than are optimal being chosen. Unfortunately, as has been known almost since the inception of spectroscopy, stars earlier than F5 tend to rotate rapidly. This leads to oblate figures and significant gradients in surface temperature (von Zeipel, 1924), resulting in visibilities that deviate from predictions by more than the error estimates and, even worse, visibilities that can change significantly with hour angle. Reflecting this fact, many lists of calibrators (e. g., Bordé et al., 2002; Mérand, Bordé, & Coudé du Foresto, 2005) have excluded hot stars for the most part.

The actual rotation state of individual stars is rarely known since the spectra give only the projected equatorial velocities, $v \sin i$, usually interpreted only through line widths. Nevertheless, projected velocities can provide useful constraints on the range of the effects on the visibilities. In this chapter we use the theory developed by von Zeipel (1924) to estimate the visibilities over the range of parameters consistent with a star's observed magnitude, color,

projected rotational velocity and parallax, and by placing each object in appropriate evolutionary grids.

In the next section we describe the models and discuss their accuracy by comparing the diameters deduced from our calculated visibilities with measurements found in the literature. Further, we have found that in many cases the existence of a lower limit to the (polar) surface gravity imposed by the Zero Age Main Sequence provides an important constraint on the range of possible inclinations and we describe its impact on the simulations in § 3.3. In § 3.4 we discuss the results for some representative examples.

We have compiled catalogs, available in electronic format[1], of early type stars that might be used as calibrators. Using typical parameters for some currently operating interferometers, we characterize for each object the range of visibilities that might be induced by rotation. In § 3.5 we describe the selection of these objects and the format of the catalogs.

A preliminary report of this research has recently appeared (Yoon et al., 2006) where we focused on the more practical aspects of rotation and the calibration problem. Some details which we skip here may be found in that report.

## 3.2 The Early Type Stars as Calibrators

### 3.2.1 The Theory of Rotating Stars

The theory of rotating stars was studied by von Zeipel in 1924. He showed that if in solid body rotation, stars will adopt the figure of a Roche spheroid to first order. Further, he showed that if radiative equilibrium holds the emergent flux varies over the surface proportionally to effective gravity, that is, effective temperature is proportional to the fourth root of the local effective gravity. This theory has been tested not only in close binary systems but also through interferometric observations of isolated stars (e. g., Domiciano de Souza et al., 2005; Peterson et al., 2006a,b; van Belle et al., 2006).

### 3.2.2 The Visibility Calculations

The calculation of the visibilities was carried out as described in Peterson et al. (2006a). Briefly, given values for the Roche parameters (e. g., § 3.3.1), the position angle of the rotational axis, and the orientation of the projected

[1]See at http://www.journals.uchicago.edu/doi/full/10.1086/518270

interferometer baseline, we construct a grid of points across the projected disk of the star, with axes parallel and perpendicular to the projected baseline.

Following the developments in Collins (1963) and Hardorp & Strittmatter (1968), we calculate local surface values of effective temperature, effective gravity, and the direction of the normal at the grid points and, using the Kurucz (1993) models as parametrized by Van Hamme (1993), the specific intensity along the viewing angle. Intensities perpendicular to the baseline are summed, creating the "strip brightness distribution" (SBD). The Fourier transform of each pixel along the baseline, taken as a hat function, is calculated and the result weighted according to the normalized SBD, multiplied by a phasor according to the "shift theorem" (Bracewell, 1965) and summed to produce an approximate complex visibility, $\tilde{V}$ (Born & Wolf, 1999). The squared visibility is then simply, $V^2 = \tilde{V}\tilde{V}^*$. We do not treat the related issue of the problems created for phase measurements due to rotation of the calibrators (Peterson et al., 2006a).

### 3.2.3 The Visibility Calibration

In what follows we calculate the variations of the visibilities that are expected for a given star over the possible range of rotation parameters. The primary purpose of these calculations is to characterize the range of visibilities but it is also of interest to know how reliable the calculated visibilities are themselves.

A good check is to compare the angular diameters we would predict in the absence of rotation with the measured diameters reported in the literature. To this end we list in Table 3.1 the long baseline angular diameters ($\theta_{meas}$) for all stars listed in the Catalog of High Angular Resolution Measurements (Richichi, Percheron, & Khristoforova, 2005) in this color range, taking care to eliminate multiple references to the same measurements. Since our calculated diameters ($\theta_{calc}$) implicitly include limb-darkening, in the few cases where only uniform disk diameters are quoted it is necessary to correct for limb-darkening effects. This was done with the simple approximation between uniform disk diameters and limb-darkened disk diameters given by Hanbury Brown et al. (1974), using linear limb-darkening coefficients appropriate for the star's temperature and the bandpass of the observations from Van Hamme (1993).

The comparison between our photometric-based calculated diameters and the measurements is shown in Figure 3.1. Systematic differences are quite small. We have solved, separately, for possible additive ($\theta_{meas} = \theta_{calc} + a$ ) or multiplicative ($\theta_{meas} = b\,\theta_{calc}$ ) offsets. The solid line in Figure 3.1 shows the best least squares fit for the additive case, $a = 0.084 \pm 0.026$ mas. The result

for the multiplicative offset, $b = 1.019 \pm 0.007$, which for clarity we do not show, is comparably small. We conclude that our visibility calculations are systematically reliable for stars in this spectral region.

On the other hand it is evident that the scatter is fairly large in Figure 3.1 and indeed we deduce reduced $\chi^2_\nu$'s of 12.15 and 13.93 for the additive and multiplicative cases, respectively. This we attribute primarily to the effects of rotation, which is explicitly not modeled in the calculations or measurements. This explanation can easily accommodate $\beta$ Cas, and $\alpha$ Aql. The large residuals for $\alpha$ CMi (Procyon), at F5V the coolest object in this list, are a puzzle, and may originate in the effects of shallow convection as discussed by Robinson et al. (2005) and Aufdenberg, Ludwig, & Kervella (2005).

## 3.3 Simulations and Interpretation

In order to consistently estimate the visibilities and accurately estimate the variations induced by rotation, we cannot simply use angular diameters provided by the usual color-magnitude-diameter relations (i. e., Barnes, Evans, & Moffet, 1978; Mozurkewich et al., 2003). Instead we must calculate models consistent with each star's color and magnitude and with its other measured properties, over the range of allowed inclinations and position angles. We describe those calculations next.

### 3.3.1 The Simulations

Roche models require several parameters: inclination angle, $i$, mass, $M$, angular diameter, $\theta$ (or equivalently the radius, $R$, through the parallax, $p$), polar effective temperature, $T_{eff,p}$, and the dimensionless angular velocity, $\omega$ ($= \Omega/\Omega_B$ where $\Omega_B$ is the angular velocity at break-up). Starting with initial guesses of mass and temperature we iterate until we match $v \sin i$ by varying the angular velocity parameter ($\omega$) or inclination angle ($i$). Within this iteration the program must also iterate for consistent values of $T_{eff,p}$ and $\theta_p$ to match the observed V magnitudes and B-V colors. With values for $\omega$, $i$, $T_{eff,p}$, $\theta_p$, parallax, and an assumed mass we can calculate the polar radius and luminosity. Interpolation in the Claret grid (Claret, 2004) assuming solar composition yields a new mass estimate(e. g., Peterson et al., 2006a). The entire process typically converges to a fraction of a percent in mass in a few iterations.

Once the low inclination limit is established (at $\omega = 0.999$ or as limited by the ZAMS gravity, see below) we sample the visibilities over the allowed

range of inclinations and position angles. To keep calculations as realistic as possible, in the catalogs and the examples discussed below the visibilities are calculated assuming the object is on the meridian and we account explicitly for its zenith distance for each specific observatory.

### 3.3.2 The ZAMS Constraint

In the process of these simulations we have found that the deduced polar gravity, $\log g_p$, increases monotonically as the inclination angle decreases with the projected velocity held fixed. Figure 3.2 shows two examples of this, for $\beta$ Leo (HR 4534) and $\zeta$ Vir (HR 5107). Panel (a) illustrates the case of $\beta$ Leo whose polar gravity (solid line) always exceeds the polar gravity of the predicted Zero Age Main Sequence (ZAMS, dotted line). In such cases we assume they are viewed equator-on only and are considered to be on the ZAMS within observational error and uncertainties in composition. $\zeta$ Vir, shown in the panel (b), illustrates the case where the potential range of the inclinations is terminated before reaching the inclination ($i \sim 30°$) corresponding to break-up, here taken to be $\omega = 0.999$. Thus the potential range of the inclinations of this object is between $i = 30°$ and $i = 90°$.

### 3.3.3 Statistical Calculations

Once the range of possible inclinations is established, $V^2$ is tabulated over a grid of 20 evenly spaced position angles and 20 inclinations. From this tabulation, we generate histograms constructed by dividing the range of squared visibilities into ten bins. The probability density function, $P_k$ of squared visibilities being the $k$ th bin is given by

$$P_k = P(V_k^2 \leq V^2 < V_{k+1}^2) = \frac{\sum_l^{n_k} \sin\, i_l}{\sum_j^N \sin\, i_j}\,, \tag{3.1}$$

$$P = \sum_{k=1}^{10} P_k = 1\,, \tag{3.2}$$

where $N$ and $n_k$ are the total number of inclination and position angle samples and the number that satisfy $V_k^2 \leq V^2 < V_{k+1}^2$ respectively. And $i_j$ and $i_l$ are the inclination angles at the sample points. We calculate the maximum ($V_{max}^2$), minimum ($V_{min}^2$), average ($\overline{V^2}$), and 68.3% (1-$\sigma$) confidence interval of $V^2$, found by splitting the out-of-range probability equally on the two sides ($-\sigma$ and $+\sigma$). The weighted average of $V^2$, $\overline{V^2}$, of the star, corresponding to the

inclination angles, is obtained from

$$\overline{V^2} = \frac{\sum_j^N V_j^2 \sin\, i_j}{\sum_j^N \sin\, i_j}\,, \tag{3.3}$$

where $V_j^2$ is the squared visibility at the $j$ th sample. The assumption here is that the rotational axis is randomly oriented in space over the range of allowed inclinations and position angles (e. g., Deutsch, 1970).

## 3.4 Results

We illustrate the range of results with four cases listed in Table 3.2. They include a slow rotator (HR 1673), an intermediate rotator (HR 8615), a moderately fast rotator (HR 3974) and, a fast rotator (HR 7740). We have used the instrument parameters appropriate for the 80 m baseline at the Navy Prototype Optical Interferometer (NPOI, Armstrong et al., 1998), operating at a wavelength of 500 nm. Note that by usual standards these 4 objects would at first glance be good calibrator choices for the 80 m baseline at the NPOI, with angular diameters nominally in the range 0.5-0.6 mas.

To put the calculations into context we note that estimates of inferred angular diameters using surface brightness-angular diameter relations are typically uncertain by a few percent. Adopting the 3% uncertainty suggested by Mozurkewich et al. (2003), a star with a uniform disk angular diameter of $\theta$=0.55 mas, measured with a 80 m baseline at 500 nm has a visibility, $V^2 = 0.63$, which is uncertain by about $\pm 0.02$. The effects of rotation on the visibilities can be substantially larger than this.

Table 3.2 presents the results of the simulations for these four objects where $V^2_{max}$, $V^2_{min}$, $\overline{V^2}$, and $\pm\sigma$ values of the squared visibilities of each star are given. The histograms for the distribution of the $V^2$'s, derived from these calculations are shown in Fig. 3.3. The bin size for the histograms is a tenth of the range maximum to minimum of squared visibility if the range is larger than 2 percent of $\overline{V^2}$, and otherwise fixed at 0.2% of the average if the range is less than 2% of $\overline{V^2}$.

The usual assumption, that slow projected rotation assures no significant effects from rotation, is not so reliable. The slow rotator, HR 1673 (panel a)), illustrated in Fig. 3.3, shows an extended, low probability tail in squared visibility. Even though the 1-$\sigma$ confidence interval for this object is very small, there is a finite chance of introducing a 4% error. In the simulations for this star the inclination was cut off at an inclination of $i = 2.45°$, with smaller

inclinations pushing the models below the ZAMS. Even with critical rotation excluded, the high inclination that is accessible can generate significant uncertainties in the visibilities.

Panel b) in Fig. 3.3 shows the corresponding histogram for HR 8615, which would normally be considered a slow rotator for these stars, with a projected rotational velocity of $85\,\mathrm{km\,s^{-1}}$. The histograms show a rather different story, with a wing on the distribution to higher squared visibilities amounting to 10% of the mean value. Thus, although this object appears to be as reasonable a candidate for a calibrator as HR 1673, it should be used only if nothing else is available.

For the moderately fast rotator, $v \sin i = 268\,\mathrm{km\,s^{-1}}$, HR 7740 (panel c)) we see the expected effects on the predicted squared visibilities. Significant flattening is predicted at all inclinations, so the visibility measurements vary significantly over the possible combinations of inclinations and position angles. In spite of a small predicted angular diameter, 0.533 mas, the range in the visibilities must be considered if calibrating with this star.

Finally, panel d) shows how the ZAMS constraint affects the visibility range of a star with moderately fast projected rotation, $v \sin i = 148\,\mathrm{km\,s^{-1}}$, HR 8615. This star appears to lie near, but slightly below the ZAMS (which we interpret to mean that it is on the ZAMS to observational limits) which greatly limits the predicted range of visibilities. We predict HR 8615 would be a good calibrator in spite of its significant projected velocity. The double horned shape of the resulting histogram is characteristic of stars which display significant rotation and are near the ZAMS.

From these examples it is clear that that the probability density functions for the squared visibilities are distinctly non-Gaussian and there is a significant question how best to characterize their shapes. For the catalogs we have decided to limit the quantitative description to simply listing the mean, the 1-$\sigma$ confidence interval and the extreme values of the squared visibilities. Since these are a rather minimal set of parameters given the obviously complex shapes involved, and we have decided to include graphs of the histograms for these objects with the archived tables.

We have assumed solar composition throughout these calculations. To see how sensitive these results are to composition, we have run the simulations in a few representative cases with Z = 0.03 (using for this purpose the Padova grid (Girardi et al., 2000) where Z=0.019 is solar composition). With the higher metallicity the deduced masses are larger as expected. However, the deduced diameters decrease only slightly and in turn the visibilities are minimally affected. In the range of diameters encountered here, the mean squared visibilities increase by typically 0.3% with an occasional case reaching 1%. We

conclude that the predictions here are not sensitive to composition so long as it is not too far from solar.

## 3.5 Catalogs

The extent to which rotation introduces errors in the calibration process depends on the wavelengths and baselines used. We consider three instruments here, the NPOI working at 500 nm, the Center for High Angular Resolution Astronomy (CHARA, ten Brummelaar et al., 2005) array at the K band, and the Very Large Telescope Interferometer (VLTI, Glindemann et al., 2003) at the K band.

For the northern instruments, our input list of potential calibrators satisfies the following criteria: (1) luminosity class III, IV, and V stars in the color range B-V$\leq$ 0.45 as listed in the Bright Star Catalogue (BSC, Hoffleit & Warren, 1991), (2) declinations above $-15°$, (3) angular size, $\theta_{BEM}$, estimated using the surface brightness-angular diameter relation of Barnes, Evans, & Moffet (1978), between 0.5 mas and 1.0 mas, and (4) distance closer than 100 pc, the last eliminates significant reddening. We then pruned the list of any stars with companions with separations, $\rho \leq 1''$ and magnitude differences, $\Delta m < 5.0$, and of all confirmed spectroscopic binaries.

A separate list with the same characteristics but with a declination range of $-90° \leq \delta \leq +15°$, was used for the VLTI catalog.

The spectroscopic binary (SB) issue is complicated for the B, A, and F stars and requires further comment. The A stars in particular are subject to a variety of non-radial pulsation modes ($\delta$ Scuti, $\delta$ Delphini, etc.) and inhomogeneous surface composition which, coupled with rotation, lead to time variable structure in the line profiles. These have on numerous occasions lead to reports of multiple spectra, radial velocity variability, and even preliminary SB1 orbits which were later questioned or retracted (e. g., Abt & Levy, 1974). Unfortunately, once listed, the "SB" classification has rarely been expunged from the BSC. The majority of the A stars in our original candidate list were characterized as SB. We have therefore removed objects reported as SB (of any flavor) only if a critical evaluation of the orbit has lead to the object's inclusion in the 9th Spectroscopic Binary Catalogue (Pourbaix et al., 2005). Failing this, we have retained the object in our catalog. As a result, we expect that there will be binaries lingering in these lists and we repeat the caution to always observe a check star as well as a primary calibrator. K-band observations will be particularly susceptible to these problems.

We have calculated catalogs for 5 specific configurations. Our main interest

is in establishing reliable calibrators for the NPOI and three of the configurations are for the 64 m, 80 m, and 100 m baselines ("AE-W7", "E6-W7", and "E7-W7", Armstrong et al., 1998). In addition, to illustrate the wavelength dependence of the results a catalog has been compiled for the 331 m CHARA arm ("S1-E1", ten Brummelaar et al., 2005). A wavelength of $2.22\,\mu m$ was adopted, typical of the K band but offset enough from band center to avoid $Br\gamma$ which is a very strong feature in these objects. Finally, to extend this to the southern hemisphere we have compiled a fifth catalog using the parameters for the 140 m VLTI arm ("B3-MO", Glindemann et al., 2003) also at $2.22\,\mu m$.

While these 5 catalogs are directly usable for the instruments and configurations indicated, they also provide some general guidance as to the reliability of individual objects as calibrators.

The catalogs consist of a text file of stars and their visibility information as shown in Table 3.2 and a separate archive of postscript files containing histograms. Table 3.3 shows the first few entries of the NPOI 80 m baseline catalog, which includes HR number, name, $\alpha$ and $\delta$ (2000), spectral type, V magnitude, B-V color, projected rotational velocity ($v \sin i$, primarily from the BSC), parallax ($p$), $V^2_{max}$, $V^2_{min}$, $\overline{V^2}$, $-\sigma$, and $+\sigma$ (columns 1 through 14, respectively). The last two columns, labeled "Q", and "E" give a rough indication of the quality of each object as a calibrator. In column labeled "Q" the calibrator is classified as " A" if $\Delta\sigma/\overline{V^2} \leq 0.02$, "B" if $0.02 < \Delta\sigma/\overline{V^2} \leq 0.04$, and "C" otherwise, where $\Delta\sigma = (+\sigma) - (-\sigma)$. The last column, "E", classifies a calibrator "+", "0", or "-", respectively, if $(V^2_{max} - V^2_{min})/\Delta\sigma \leq 2$, between 2 and 4, or greater than 4. The "E" classification is meant to warn of cases where one might be "Exposed" to large error in $V^2$, even when $\Delta\sigma$ is small and the probability of such exposure is small. The histograms have a format similar to the figures shown in this chapter.

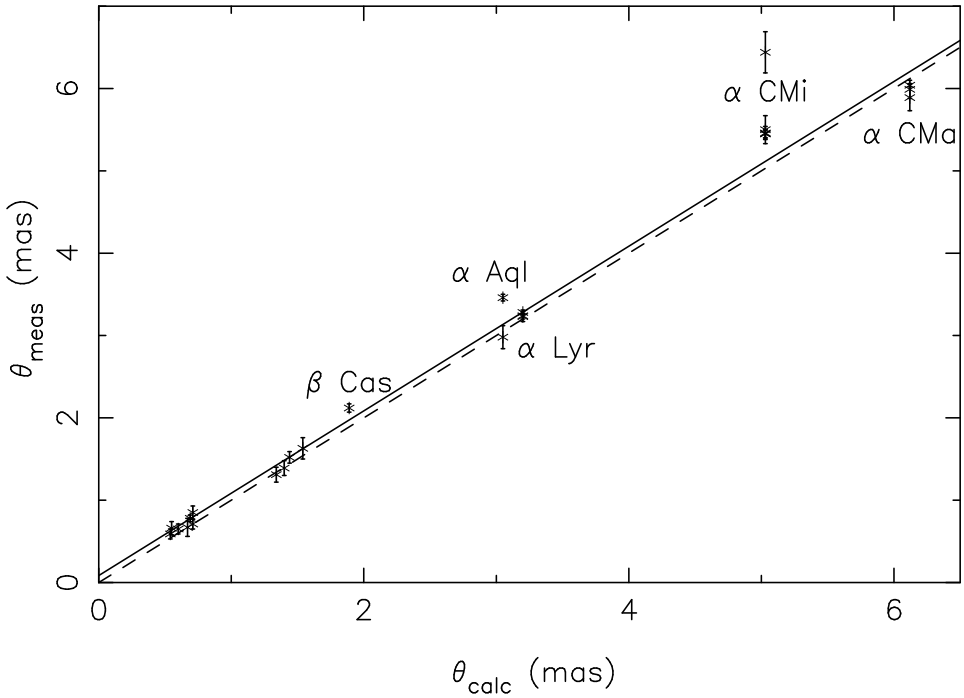


Figure 3.1 The comparison between measured and calculated angular diameters of early type stars. The dashed line of unit slope represents perfect agreement, while the solid line shows the least square fit of the measurements to the calculated values with an additive offset (of $0.084 \pm 0.026$ mas). The deviations of $\beta$ Cas and $\alpha$ Aql are probably due to rotation.

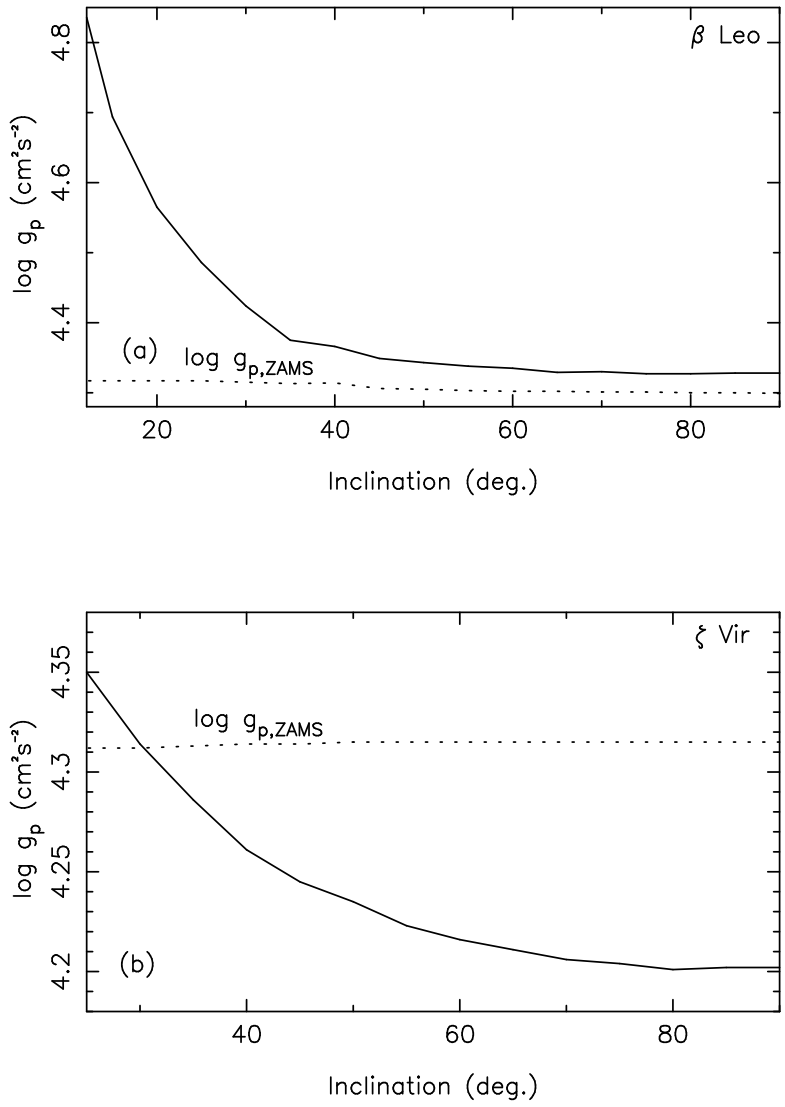


Figure 3.2 Shown are the relationships between polar gravity (the logarithm) and inclination of $\beta$ Leo (a) and $\zeta$ Vir (b) (solid lines). The inclination covers the range from equator-on to break-up ($\omega = 0.999$). The dotted line shows the polar gravity at the ZAMS. $\beta$ Leo has a larger polar gravity than if it were on the ZAMS with its predicted mass for all inclinations. In such cases we assume it is viewed at $i = 90°$. The permitted range of inclinations for $\zeta$ Vir is terminated well before break-up ($\omega = 0.978$) by the ZAMS constraint.

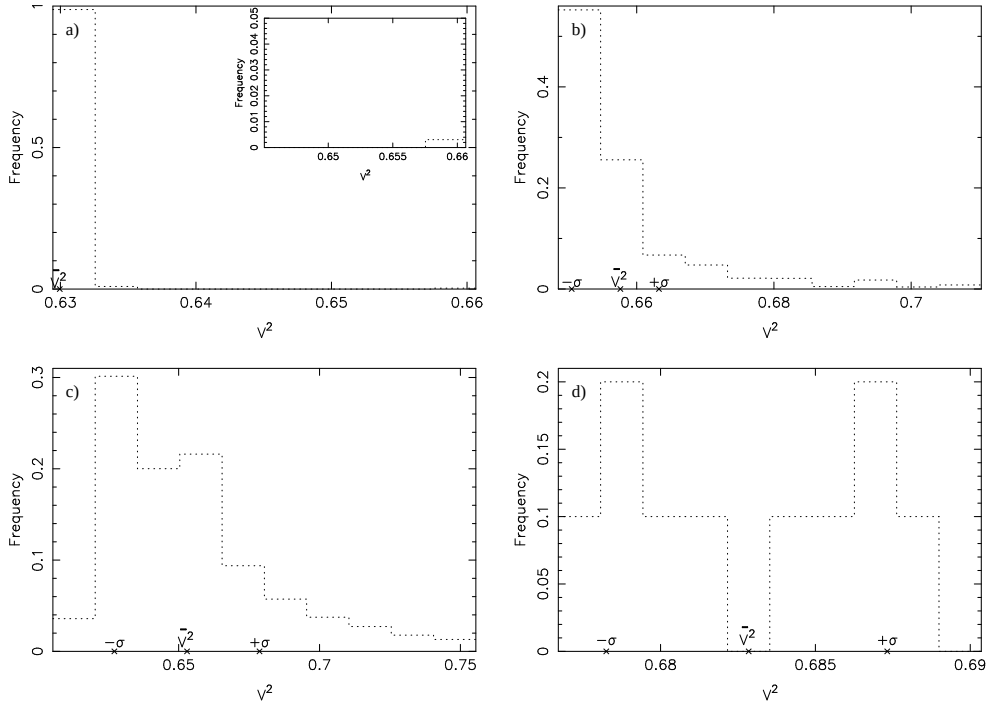


Figure 3.3 Histograms of squared visibilities. a) HR 1673 (68 Eri) is a slow rotator with $v \sin i = 10\,\mathrm{km\,s^{-1}}$. In spite of its slow rotation and narrow range of $\pm\sigma$, the histogram displays an extended tail, albeit of low probability, as shown in the inset. These extreme visibilities result from the fact that star could be seen nearly pole on. b) histogram for HR 8615 (31 Cep), an intermediate velocity rotator with $v \sin i = 87\,\mathrm{km\,s^{-1}}$. This star can be a calibrator, but the full range of squared visibilities should be properly considered because of the extended tail of possible $V^2$ values, and particularly the asymmetric distribution. c) HR 7740 (33 Cyg) is a fast rotator with $v \sin i = 268\,\mathrm{km\,s^{-1}}$. As expected, the rotation significantly affects the visibilities. d) moderately rotating star, HR 3974 (21 LMi) with $v \sin i = 148\,\mathrm{km\,s^{-1}}$ which is on or very near the ZAMS and is therefore assumed seen equator-on. This can be a good calibrator because of the small predicted range in $V^2$, owing to the constrained range of inclination.

Table 3.1. Measured values and calculated values of angular diameter.

| HR | Name | $\theta_{calc}$ | $\theta_{meas}$ | Bandpass | References |
|---|---|---|---|---|---|
| 21 | 11 $\beta$ Cas | 1.89 | 2.12 ± 0.05 | 740 nm | Nordgren et al. (1999) |
| 82 | 27 $\rho$ And | 0.55 | 0.66 ± 0.08* | H, K | Lane, Boden, & Kulkarni (2001) |
| 269 | 37 $\mu$ And | 0.67 | 0.67 ± 0.11* | H, K | Lane, Boden, & Kulkarni (2001) |
| 2421 | 24 $\gamma$ Gem | 1.40 | 1.39 ± 0.09 | 443 nm | Hanbury Brown, Davis, & Allen (1974) |
| 2491 | 9 $\alpha$ CMa | 6.12 | 6.04 ± 0.02 | K | Kervella et al. (2003) |
| | | | 5.89 ± 0.16 | 443 nm | Hanbury Brown, Davis, & Allen (1974) |
| | | | 5.99 ± 0.11 | 800, 451 nm | Mozurkewich et al. (2003) |
| 2943 | 10 $\alpha$ CMi | 5.03 | 5.45 ± 0.05 | K | Kervella et al. (2004), |
| | | | 5.45 ± 0.05 | 451, 550, 800 nm | Mozurkewich et al. (2003) |
| | | | 5.50 ± 0.17 | 443 nm | Hanbury Brown, Davis, & Allen (1974) |
| | | | 6.44 ± 0.25 | 706 nm | Shao et al. (1988) |
| | | | 5.46 ± 0.08 | 740 nm | Nordgren, Sudol, & Mozurkewich (2001) |
| 4090 | 30 LMi | 0.54 | 0.59 ± 0.06* | H, K | Lane, Boden, & Kulkarni (2001) |
| 4534 | 94 $\beta$ Leo | 1.34 | 1.31 ± 0.09* | 443 nm | Hanbury Brown, Davis, & Allen (1974) |
| 5447 | 28 $\sigma$ Boo | 0.69 | 0.78 ± 0.04* | H, K | Boden, Creech-Eakman, & Queloz (2000) |
| 6556 | 55 $\alpha$ Oph | 1.54 | 1.63 ± 0.13 | 443 nm | Hanbury Brown, Davis, & Allen (1974) |
| 6629 | 62 $\gamma$ Oph | 0.60 | 0.65 ± 0.06* | H, K | Lane, Boden, & Kulkarni (2001) |
| 7001 | 3 $\alpha$ Lyr | 3.20 | 3.23 ± 0.03 | 451, 500, 800 nm | Mozurkewich et al. (2003) |
| | | | 3.24 ± 0.07 | 438.5 nm | Hanbury Brown, Davis, & Allen (1974) |
| | | | 3.28 ± 0.01 | K | Ciardi et al. (2001) |
| 7469 | 13 $\theta$ Cyg | 0.71 | 0.71 ± 0.06* | H, K | Boden & Lane (2001) |
| | | | 0.85 ± 0.08* | H, K | Torres et al. (2002) |
| 7557 | 53 $\alpha$ Aql | 3.05 | 3.46 ± 0.04 | 451, 550, 800 nm | Mozurkewich et al. (2003) |
| | | | 2.98 ± 0.14 | 460.8 nm | Hanbury Brown, Davis, & Allen (1974) |
| 8162 | 5 $\alpha$ Cep | 1.44 | 1.52 ± 0.07* | 656 nm | Vakili et al. (1998) |

*We have corrected these measurements to account for limb-darkening as described in the text.

Table 3.2. Examples of the effects of rotation on potential calibrators as measured by the maximum, minimum, weighted average, and $\pm\sigma$ values of $V^2$ using the NPOI (80 m baseline at $\lambda = 500$ nm)

| HR | Name | SpType | V | B-V | $v \sin i$[a] | $\theta_{BEM}$[b] | $p$[c] | $V^2_{max}$ | $V^2_{min}$ | $\overline{V^2}$ | - $\sigma$ | $+\sigma$ |
|---|---|---|---|---|---|---|---|---|---|---|---|---|
| 1673 | 68 Eri | F2V | 5.12 | 0.44 | 10 | 0.606 | 39.99 | 0.6610 | 0.6298 | 0.6306 | 0.6304 | 0.6306 |
| 3974 | 21 LMi | A7V | 4.48 | 0.18 | 148 | 0.546 | 35.78 | 0.6881 | 0.6778 | 0.6829 | 0.6783 | 0.6874 |
| 7740 | 33 Cyg | A3IV-Vn | 4.30 | 0.11 | 268 | 0.533 | 21.41 | 0.7555 | 0.6054 | 0.6530 | 0.6272 | 0.6787 |
| 8615 | 31 Cep | F3III-IV | 5.08 | 0.39 | 85 | 0.571 | 17.70 | 0.7102 | 0.6486 | 0.6576 | 0.6505 | 0.6632 |

[a] $v \sin i$ is in units of $\mathrm{km\,s^{-1}}$.

[b] Angular diameter, $\theta_{BEM}$, in units of mas, from the Barnes, Evans, & Moffet (1978) relation, for guidance only.

[c] Parallax, $p$ is in units of mas from HIPPARCOS (ESA, 1997).

Table 3.3. Example of Catalogs: NPOI 80 m baseline

| HR | Name | $\alpha$ | $\delta$ 2000 | SpType | V | B-V | $v \sin i$ | $p$ | $V^2_{max}$ | $V^2_{min}$ | $\overline{V^2}$ | - $\sigma$ | $+\sigma$ | Q[a] | E[b] |
|---|---|---|---|---|---|---|---|---|---|---|---|---|---|---|---|
| 82 | 27$\rho$ And | $00^h\,21^m\,07^s.3$ | $+37^\circ\,58'\,07''$ | F5III | 5.18 | 0.42 | 41 | 20.42 | 0.7019 | 0.6494 | 0.6528 | 0.6502 | 0.6540 | A | - |
| 269 | 37$\mu$ And | $00^h\,56^m\,45^s.2$ | $+38^\circ\,29'\,58''$ | A5V | 3.87 | 0.13 | 72 | 23.93 | 0.5870 | 0.5221 | 0.5297 | 0.5242 | 0.5330 | A | - |
| 343 | 33$\theta$ Cas | $01^h\,11^m\,06^s.2$ | $+55^\circ\,08'\,59''$ | A7V | 4.33 | 0.17 | 102 | 23.73 | 0.6910 | 0.6338 | 0.6426 | 0.6358 | 0.6469 | A | - |
| 417 | 48$\omega$ And | $01^h\,27^m\,39^s.4$ | $+45^\circ\,24'\,24''$ | F5IV | 4.83 | 0.42 | 69 | 35.33 | 0.6183 | 0.5496 | 0.5563 | 0.5510 | 0.5598 | A | - |
| 531 | 53$\chi$ Cet | $01^h\,49^m\,35^s.1$ | $-10^\circ\,41'\,11''$ | F3III | 4.67 | 0.33 | 61 | 42.35 | 0.6152 | 0.6080 | 0.6103 | 0.6089 | 0.6115 | A | 0 |

[a]Letters A, B and C characterize the $1-\sigma$ width of the visibility distribution, see text.

[b]Characters +, 0, and - indicate how extended the tails in the visibility distributions are, see text.

# Chapter 4

# Potential target list of A and F stars for the Navy Prototype Interferometer

## 4.1 Introduction

Recently the NPOI has begun making measurements which will challenge and ultimately revisit our understanding of the physical processes governing the distribution and evolution of angular momentum within stars. It has resolved the photospheres of two of the brightest main sequence A stars, Vega and Altair. Both are rotating surprising rapidly at over 90% of breakup in units of angular velocity.

It is now time to consider how to use the NPOI to best lay out how the rotational characteristics of A and F stars change as they evolve off the main sequence. It appears that even with the geometry used for the Vega and Altair observations, the gross rotational parameters of a number of other bright A and F stars can be determined by NPOI. With the addition of an 80-meter baseline and imminent addition of an 100-meter baseline, this list can be substantially expanded. Thus it is time to define a list of potential NPOI targets that will optimally characterize the rotational evolution of this group of objects. This chapter provides such a list and the methodology used to create it.

In the next section, the criteria for the NPOI observation are described and the instrumental configurations of the NPOI are mentioned in the following section. The computations for the detection probabilities of apparent oblateness and surface brightness asymmetry are explained in § 4.4. The last two sections summarize the results and the final target lists for available triangle configurations.

## 4.2 Criteria

The criteria for the NPOI target list are similar to those of the calibrators list for the instrument, but with some changes. The detailed criteria for the targets are as follows. For the NPOI, a list of potential targets was first produced which satisfied the following criteria: (1) luminosity class III, IV, and V stars in the color range $-0.05 \leq$ B-V $\leq 0.45$ as listed in the BSC (Hoffleit & Warren, 1991), (2) declinations above $-15°$, (3) angular size, $\theta_{BEM}$, estimated using the surface brightness-angular diameter relation of Barnes, Evans, & Moffet (1978), larger than 0.4 mas, and (4) distance closer than 100 pc, the last eliminates significant reddening. We then pruned the list of any stars with companions with separations, $\rho \leq 1''$ and magnitude differences, $\Delta m < 5.0$, and of all confirmed spectroscopic binaries. With regard to the spectroscopic binary issue, see the comments described in § 3.5.

## 4.3 Instrument Configurations

The NPOI is currently used in a variety of configurations with typically four active stations. For a fixed configuration three independent triangles can be formed. In order to focus on specific, but typical measurements we consider two triangles, one using stations "E6-AW-W7" having a longest baseline of 80-meters and the other with "AN-E7-W7" whose longest baseline is 100-meters. Below we will refer to these configurations as simply 80 m and 100 m. We consider only the reddest 17 channels covering from 560 nm to 850 nm (Armstrong et al., 1998), as is the current practice.

## 4.4 Simulations

The Roche models were calculated as described in § 3.3 and visibilities as in § 3.2.2. Measuring diameters at various baseline orientations the squared visibility amplitude provides information on a star's oblateness. In contrast asymmetry in the surface brightness distribution is best detected through visibility phase measurements. By computing the probabilities for detecting oblateness and asymmetry of a star, we can identify potential targets for the NPOI observation.

In order to compute these probabilities, we need to assume a couple of things. We do not know the orientation of the star so we assume that the rotation axis is randomly distributed and we test the null hypothesis described in § 4.4.1 at 12 position angles with a step of 15 °, which covers all possibilities

because of axial symmetry. We compute the probabilities for the detections by finding the inclination range, which gives definite detections at a given position angle. By averaging the probabilities over the position angles, the final probabilities of oblateness and asymmetry of the stars are obtained. The detail calculations for oblateness and asymmetry at a given position angle follow.

### 4.4.1 Oblateness

To calculate the probability for detecting oblateness due to rotation, a null hypothesis test was performed. The null hypothesis is that the star is a normal limb-darkened sphere. Here we assume a square-root limb-darkening law because stars whose effective temperature are hotter than 8500 K are well described by this limb-darkening law (Díaz-Cordovés & Giménez, 1992), which is given by

$$I_\lambda(\mu) = I_\lambda(1)(1 - x_\lambda(1-\mu) - y_\lambda(1-\sqrt{\mu})) \tag{4.1}$$

where $\lambda$ is a wavelength, $\mu$ is a limb-darkening angle, and $x_\lambda$ and $y_\lambda$ are limb-darkening coefficients. The squared visibility can then be obtained analytically,

$$V^2 = d^2 \left[ a\frac{J_1\left(\frac{\pi B_\perp \theta}{\lambda}\right)}{\frac{\pi B_\perp \theta}{\lambda}} + b\frac{J_{3/2}\left(\frac{\pi B_\perp \theta}{\lambda}\right)}{\left(\frac{\pi B_\perp \theta}{\lambda}\right)^{3/2}} + c\frac{J_{5/4}\left(\frac{\pi B_\perp \theta}{\lambda}\right)}{(\frac{\pi B_\perp \theta}{\lambda})^{5/4}} \right]^2 \tag{4.2}$$

where

$$a = 2(1 - x_\lambda - y_\lambda) \tag{4.3}$$

$$b = \sqrt{\frac{\pi}{2}} \tag{4.4}$$

$$c = 2^{5/4}\frac{\pi}{4}\Gamma(1/4)y_\lambda \tag{4.5}$$

$$d = \left(\frac{1 - x_\lambda - y_\lambda}{2} + \frac{x_\lambda}{3} + \frac{4\pi y_\lambda}{5}\right)^{-1}. \tag{4.6}$$

For the hypothesis test, we consider the visibilities which a Roche model produces as the measured visibilities and the visibilities which a limb-darkened spherical model predicts as the theoretical visibilities. Here the Roche model produces a visibility as a function of baseline, wavelength, hour angle, and position angle. At a given position angle, we produce visibilities over 3 baselines for the chosen triangle, 17 channels, and 3 hour angles (meridian, $-3^h$, and $+3^h$). Then we fit the measured visibilities to the Roche model visibilities

which are theoretical visibilities, calculate the chi-square of the fit and minimize the $\chi^2$ at a given position angle. Here we assumed that the measurement error of $V^2$ is an empirical value, 0.0003. We choose a 95% confidence interval for the $\chi^2$ and if the fit is not within the confidence interval we reject the null hypothesis. If we reject the hypothesis, we can consider that the star is not a limb-darkened sphere, and that we have detected oblateness. If we accept the hypothesis, the star is consistent with a limb-darkened sphere without detectable oblateness.

### 4.4.2 Asymmetry

While calculating the probability for oblateness, we also look for surface brightness asymmetry using either triple phases technique or the differential phase technique. We consider both techniques because triple (closure) phase is the technique currently in use while the differential phase technique improves the detectability.

The triple phase is the sum of three measured visibility phases around a closed triangle of baselines and it is an intrinsic property of a star. As for all phases, the triple phase shows a top-hat behavior, i. e., its value is unity or zero when the star's brightness distribution is centrosymmetric. This occurs for example when a rotating star is seen equator-on, while we observe increasing deviations from simple sign flips in triple phase at the different position angles as one approaches the inclination angle near break-up (while preserving $v \sin i$). For the detection of asymmetry, we check whether the triple phase deviation is larger than $1^\circ$ and if it is, we conclude it shows the asymmetry. Therefore the criterion for the detection via the triple phase, $\phi_{123}$, at a given triangle of baselines is given by,

$$d\phi_{123} > 1.^\circ + 29.^\circ \exp(-V_1 V_2 V_3 / 0.01) \tag{4.7}$$

where the second term on the right hand side compensates for an increase in the measurement error when the triple amplitude goes near a zero, $V_1 V_2 V_3$ is the triple visibility amplitude, and the denominator, 0.01 in the exponent is empirically determined. The significant deviation in phase is larger than $3^\circ$ but the closure phase is already additive phase of three independent baseline phases so $1^\circ$ is enough for a signal of asymmetry.

The differential phase technique seeks a variation of the phase from a single baseline as a function of wavelength. This technique is also free from atmospheric and instrumental effects to first order. The differential phase technique has more phase information than the triple phase because the number of baselines is more than the number of triangle configurations for the triple phase,

particularly for a small number of stations. The criterion for detection of asymmetry via the differential phase, $\Delta\phi_i = \phi(\lambda_{i+1}) - \phi(\lambda_i)$ is given by,

$$\Delta\phi_i > 3(1.^\circ + 29.^\circ \exp(-V^2/0.01)) \tag{4.8}$$

where $V^2$ is the squared visibility at the given baseline and the denominator in the exponent, 0.01 is also empirically determined.

These two criteria are applied to check the detectability of asymmetry during the simulations. The procedure for calculating probability of asymmetry is same as that of oblateness, which we describe next.

### 4.4.3 Calculations of Probabilities

First we calculate the visibilities of each star at equator-on ($i = 90^\circ$) where the oblateness and asymmetry of the star are the smallest ($\omega$ is smallest since we force the model to match $v \sin i$ by changing the angular velocity parameter). If at least one visibility among visibilities which are produced over 3 baselines, 17 channels, and 3 hour angles shows a detection, that is a rejection of the null hypothesis that the star is a limb-darkened sphere, the probability of detection at that position angle is unity.

Next, we simulate a star at break-up. Here we take $\omega = 0.99$ and find the inclination angle, $i_B$, which gives the correct $v \sin i$. As the inclination angle varies from $i = 90^\circ$ to $i_B$, maintaining the projected velocity, the range of squared visibilities increases as a function of position angle because of both intensity variations over the surface as well as actual geometrical flattening. At the same time the deviation from the top-hat behavior of a triple phase increases.

For both cases of the equator-on and break-up, we check the ZAMS constraint as described in § 3.3.2. If the polar surface gravity for the two cases are both larger than or equal to the gravity on the ZAMS, we assume the star is an equator-on ZAMS star. Otherwise we search for the critical inclination angle, $i_{cr}$, which gives a surface gravity the same as that on ZAMS if the polar gravity at the break-up is larger than that at the ZAMS and the gravity at equator-on is smaller than that, allowed inclinations then range between $i_{cr}$ and 90°. Otherwise the allowed range is between $i_B$ and 90°.

The calculation of the probabilities can be divided three cases based on the null hypothesis at each position angle; 1) reject the null hypothesis at both equator-on and at break-up, 2) acceptance at both $i = 90^\circ$ and $i_B$, and 3) rejection at $i = 90^\circ$ and acceptance at $i_B$, which means we should find a threshold angle, $i_{th}$ which gives the detection for oblateness or asymmetry.

The first case and second case, we just average out the probabilities of unity or zero over the 12 position angles. For the third case, we find the threshold angle by a simple bisection method. By assuming that within the range of allowed inclinations, from $i_B$ (or $i_{cr}$ if ZAMS constraint limits the inclination angle) to $i = 90°$, the rotational axis is uniformly distributed in space, then the probability of detection at the position angle is given simply as

$$P_{iPA} = \frac{\int_{i_{th}}^{i_B} \sin\ i di}{\int_{90°}^{i_B} \sin\ i di} = \frac{\cos i_B - \cos i_{th}}{\cos i_B}. \tag{4.9}$$

where $P_{iPA}$ is the probability at i-th position angle. This definition is applicable to both oblateness and asymmetry. By assuming that the rotational axis is randomly oriented in position angle the final probability, P, is given by,

$$P = \frac{1}{12} \cdot \sum_{iPA=1}^{12} P_{iPA}. \tag{4.10}$$

## 4.5 Results

Table 4.1 shows the preliminary targets which satisfy the criteria for the NPOI observation of oblateness and asymmetry. It includes HR number, name, $\alpha$ and $\delta$ (2000), spectral type, V magnitude, B-V color, projected rotational velocity ($v \sin i$, primarily from the BSC), parallax ($p$). From the calculations described in § 4.4, we needed to derive the physical properties of the stars as well as the detection probabilities. Table 4.2 and Table 4.3 show the calculation of the physical properties and probabilities for oblateness and asymmetry based on 80 m and 100 m baselines respectively. The tables include HR number, angular velocity rate at equator-on, $\omega_{90}$, critical inclination angle, $i_c$, threshold angle for oblateness detection, $i^{th}_{obl.}$, threshold angle for asymmetry detection via triple phase, $i^{th}_{asy.}$, threshold angle for asymmetry detection via differential phase, $i^{th}_{\Delta\phi}$, polar effective temperature at $i = 90°$, $T_{90}$, polar effective temperature at critical angle, $T_c$, deduced mass at $i = 90°$, $M_{90}$, deduced mass at critical angle, $M_c$, major angular diameter at $i = 90°$, $\theta^{90}_{max}$, minor angular diameter at $i = 90°$, $\theta^{90}_{min}$, major angular diameter at $i_c$, $\theta^{c}_{max}$, minor angular diameter at $i_c$, $\theta^{c}_{min}$, probability for detecting oblateness, $P_{obl.}$, probability for detecting asymmetry via triple phase technique, $P_{asy.}$, probability for asymmetry via differential phase technique, $P(\Delta\phi)$, and comments. For that last column, comments show the value of $\omega$ if the inclination is limited by the ZAMS constraint.

## 4.6 Final Target Lists

For the NPOI observations of apparent oblateness and surface brightness asymmetry on A and F stars, lists of potential targets with at least 25% detection probability are shown in Table 4.4, 4.5, and 4.6.

Twenty two objects show 100% detection of oblateness and probably 31 more objects are detectable for oblateness. Three of the targets, $\beta$ Cas, $\alpha$ Oph, and $\alpha$ Cep, should show measurable triple phase signals according to the simulations with a triangle including the longest 80 m baseline. With differential phase techniques detection probabilities improve to where 23 more objects might show measurable asymmetry (with 12 predicted to have at least 50% detection probability).

As we expected a triangle configuration including the longest 100 m baseline, substantially improves the detection statistics for both oblateness and asymmetry. As shown in Table 4.3, 45 targets would show 100% detectability for oblateness and there are more probable targets for the detection. For asymmetry via the triple phase technique, two more objects could show measurable asymmetry than those at 80 m baseline. The differential phase technique shows that 33 objects might show asymmetry with 22 predicted to have at least 50% detection probability.

Through the investigations with those targets, the study of rotational effects on A and F stars can be developed.

Table 4.1. The Preliminary targets for NPOI observation

| HR | Name | $\alpha$ | $\delta$ 2000 | SpType | V | B-V | $v \sin i$ | $\pi$ |
|---|---|---|---|---|---|---|---|---|
| 15 | 21Alp And | 000823.3 | +290526 | B8IVpMnHg v | 2.06 | -0.11 | 56 | 33.60 |
| 21 | 11Bet Cas | 000910.7 | +590859 | F2III-IV | 2.27 | 0.34 | 70 | 59.89 |
| 82 | 27Rho And | 002107.3 | +375807 | F5III | 5.18 | 0.42 | 41 | 20.42 |
| 269 | 37Mu And | 005645.2 | +382958 | A5V | 3.87 | 0.13 | 72 | 23.93 |
| 343 | 33The Cas | 011106.2 | +550859 | A7V | 4.33 | 0.17 | 102 | 23.73 |
| 403 | 37Del Cas | 012549.0 | +601407 | A5III-IV v | 2.68 | 0.13 | 113 | 32.81 |
| 417 | 48Ome And | 012739.4 | +452424 | F5IV | 4.83 | 0.42 | 69 | 35.33 |
| 531 | 53Chi Cet | 014935.1 | -104111 | F3III | 4.67 | 0.33 | 61 | 42.35 |
| 553 | 6Bet Ari | 015438.4 | +204829 | A5V | 2.64 | 0.13 | 79 | 54.74 |
| 569 | 9Lam Ari | 015755.7 | +233546 | F0V | 4.79 | 0.28 | 99 | 24.49 |
| 575 | 48 Cas | 020157.4 | +705425 | A3IV | 4.54 | 0.16 | 67 | 27.91 |
| 623 | 14 Ari | 020925.3 | +255623 | F2III | 4.98 | 0.33 | 154 | 10.19 |
| 646 | 17Eta Ari | 021248.1 | +211239 | F5V | 5.27 | 0.43 | 9 | 33.19 |
| 664 | 9Gam Tri | 021718.9 | +335050 | A1Vnn | 4.01 | 0.02 | 208 | 27.73 |
| 813 | 87Mu Cet | 024456.5 | +100651 | F0IV | 4.27 | 0.31 | 54 | 38.71 |
| 838 | 41 Ari | 024959.0 | +271538 | B8Vn | 3.63 | -0.10 | 180 | 20.45 |
| 840 | 16 Per | 025035.1 | +381907 | F2III | 4.23 | 0.34 | 149 | 25.54 |
| 855 | 20 Per | 025342.6 | +382015 | F4IV | 5.33 | 0.41 | 63 | 13.87 |
| 984 | 13Zet Eri | 031550.0 | -084911 | A5m | 4.80 | 0.23 | 66 | 27.18 |
| 1069 | 36 Per | 033226.3 | +460325 | F4III | 5.31 | 0.40 | 29 | 27.46 |
| 1251 | 38Nu Tau | 040309.4 | +055921 | A1V | 3.91 | 0.03 | 69 | 25.24 |
| 1298 | 38Omi1Eri | 041151.9 | -065015 | F2II-III | 4.04 | 0.33 | 96 | 25.98 |
| 1387 | 65Kap1Tau | 042522.1 | +221738 | A7IV-V | 4.22 | 0.13 | 81 | 21.27 |
| 1392 | 69Ups Tau | 042618.5 | +224849 | A8Vn | 4.28 | 0.26 | 196 | 21.07 |
| 1394 | 71 Tau | 042620.8 | +153706 | F0V | 4.49 | 0.25 | 192 | 20.86 |
| 1412 | 78The2Tau | 042839.7 | +155215 | A7III | 3.73 | +0.18 | 78 | 21.89 |
| 1412 | 78The2Tau | 042839.7 | +155215 | A7V | 4.76 | +0.18 | 110 | 21.89 |
| 1444 | 86Rho Tau | 043350.9 | +145040 | A8V | 4.65 | 0.25 | 117 | 21.39 |
| 1473 | 90 Tau | 043809.5 | +123039 | A6V | 4.27 | 0.12 | 79 | 21.79 |
| 1560 | 61Ome Eri | 045253.7 | -052710 | F4III+A6III | 4.39 | 0.25 | 153 | 14.39 |
| 1637 | 9 Aur | 050640.6 | +513552 | F0V | 5.00 | 0.33 | 14 | 38.14 |
| 1641 | 10Eta Aur | 050630.9 | +411404 | B3V | 3.17 | -0.18 | 132 | 14.87 |
| 1666 | 67Bet Eri | 050751.0 | -050511 | A3III | 2.79 | 0.13 | 179 | 36.71 |
| 1673 | 68 Eri | 050843.6 | -042722 | F2V | 5.12 | 0.44 | 10 | 39.99 |
| 1676 | 15 Ori | 050942.0 | +153550 | F2IV | 4.82 | 0.32 | 53 | 10.24 |
| 1790 | 24Gam Ori | 052507.9 | +062059 | B2III | 1.64 | -0.22 | 59 | 13.42 |
| 1791 | 112Bet Tau | 052617.5 | +283627 | B7III | 1.65 | -0.13 | 71 | 24.89 |
| 1998 | 14Zet Lep | 054657.3 | -144919 | A3Vn | 3.55 | 0.10 | 202 | 46.47 |
| 2085 | 16Eta Lep | 055624.3 | -141004 | F1III | 3.71 | 0.33 | 20 | 66.47 |
| 2095 | 37The Aur | 055943.3 | +371245 | A0pSi | 2.62 | -0.08 | 49 | 18.83 |
| 2124 | 61Mu Ori | 060223.0 | +093851 | A2V | 4.12 | 0.16 | 24 | 21.49 |
| 2220 | 71 Ori | 061450.9 | +190923 | F6V | 5.20 | 0.44 | 13 | 47.33 |
| 2241 | 74 Ori | 061626.6 | +121620 | F5IV-V | 5.04 | 0.42 | 17 | 51.00 |
| 2264 | 45 Aur | 062146.1 | +532708 | F5III | 5.36 | 0.43 | 14 | 17.54 |
| 2298 | 8Eps Mon | 062346.1 | +043534 | A5IV | 4.44 | 0.18 | 124 | 25.39 |
| 2421 | 24Gam Gem | 063742.7 | +162357 | A0IV | 1.93 | 0.00 | 32 | 31.12 |
| 2484 | 31Xi Gem | 064517.4 | +125344 | F5III | 3.36 | 0.43 | 70 | 57.02 |
| 2540 | 34The Gem | 065247.3 | +335740 | A3III | 3.60 | 0.10 | 128 | 16.59 |
| 2564 | 38 Gem | 065438.7 | +131040 | F0Vp | 4.65 | 0.30 | 126 | 35.79 |
| 2763 | 54Lam Gem | 071805.6 | +163225 | A3V | 3.58 | 0.11 | 154 | 34.59 |
| 2777 | 55Del Gem | 072007.4 | +215856 | F2IV | 3.53 | 0.34 | 111 | 55.45 |

Table 4.1—Continued

| HR | Name | $\alpha$ | $\delta$ 2000 | SpType | V | B-V | $v \sin i$ | $\pi$ |
|---|---|---|---|---|---|---|---|---|
| 2849 | 22 Lyn | 072956.0 | +494021 | F6V | 5.36 | 0.45 | 12 | 50.25 |
| 2852 | 62Rho Gem | 072906.7 | +314704 | F0V | 4.18 | 0.32 | 68 | 54.06 |
| 2890 | 66Alp Gem | 073436.0 | +315319 | A2Vm | 2.88 | 0.04 | 30 | 66.00 |
| 2891 | 66Alp Gem | 073436.0 | +315318 | A1V | 1.98 | 0.03 | 14 | 66.00 |
| 2927 | 25 Mon | 073716.7 | -040640 | F6III | 5.13 | 0.44 | 20 | 16.11 |
| 2930 | 71Omi Gem | 073909.9 | +343503 | F3III | 4.90 | 0.40 | 89 | 20.62 |
| 3015 | 4 Pup | 074556.9 | -143350 | F0V | 5.04 | 0.33 | 101 | 13.80 |
| 3314 | | 082539.6 | -035423 | A0V | 3.90 | -0.02 | 125 | 26.09 |
| 3572 | 65Alp Cnc | 085829.2 | +115128 | A5m | 4.25 | 0.14 | 68 | 18.79 |
| 3619 | 15 UMa | 090852.3 | +513617 | F0IVm vs | 4.48 | 0.27 | 37 | 34.12 |
| 3624 | 14Tau UMa | 091055.1 | +633049 | F3-4IIIm vs | 4.67 | 0.35 | 18 | 26.79 |
| 3690 | 38 Lyn | 091850.7 | +364809 | A3V | 3.82 | 0.06 | 165 | 26.75 |
| 3757 | 23 UMa | 093131.7 | +630343 | F0IV | 3.67 | 0.33 | 140 | 43.20 |
| 3888 | 29Ups UMa | 095059.4 | +590219 | F2IV | 3.80 | 0.29 | 110 | 28.35 |
| 3974 | 21 LMi | 100725.8 | +351441 | A7V | 4.48 | 0.18 | 148 | 35.78 |
| 4033 | 33Lam UMa | 101705.8 | +425452 | A2IV | 3.45 | 0.03 | 48 | 24.27 |
| 4054 | 40 Leo | 101944.1 | +192815 | F6IV | 4.79 | 0.45 | 16 | 47.24 |
| 4084 | | 103104.6 | +823331 | F2V | 5.26 | 0.37 | 107 | 46.54 |
| 4090 | 30 LMi | 102554.9 | +334746 | F0V | 4.74 | 0.25 | 31 | 15.76 |
| 4132 | | 103313.9 | +402532 | A7IV | 4.75 | 0.23 | 132 | 29.13 |
| 4141 | 37 UMa | 103509.7 | +570458 | F1V | 5.16 | 0.34 | 87 | 37.80 |
| 4295 | 48Bet UMa | 110150.5 | +562257 | A1V | 2.37 | -0.02 | 39 | 41.07 |
| 4310 | 63Chi Leo | 110501.0 | +072010 | F2III-IV v | 4.63 | 0.33 | 25 | 34.54 |
| 4357 | 68Del Leo | 111406.5 | +203125 | A4V | 2.56 | 0.12 | 181 | 56.52 |
| 4359 | 70The Leo | 111414.4 | +152546 | A2V | 3.34 | -0.01 | 20 | 18.36 |
| 4399 | 78Iot Leo | 112355.5 | +103145 | F4IV | 3.94 | 0.41 | 20 | 41.26 |
| 4368 | 74Phi Leo | 111639.7 | -033906 | A7IVn | 4.47 | 0.21 | 225 | 16.69 |
| 4534 | 94Bet Leo | 114903.6 | +143419 | A3V | 2.14 | 0.09 | 121 | 90.16 |
| 4554 | 64Gam UMa | 115349.8 | +534141 | A0Ve | 2.44 | 0.00 | 168 | 38.99 |
| 4646 | | 121211.9 | +773659 | A5m | 5.14 | 0.33 | 79 | 29.70 |
| 4660 | 69Del UMa | 121525.6 | +570157 | A3V | 3.31 | 0.08 | 177 | 40.05 |
| 4733 | 14 Com | 122624.1 | +271606 | F0p | 4.95 | 0.27 | 227 | 11.92 |
| 4753 | 18 Com | 122926.9 | +240632 | F5III | 5.48 | 0.43 | 93 | 15.10 |
| 4825 | 29Gam Vir | 124139.6 | -012658 | F0V | 3.48 | 0.36 | 28 | 84.53 |
| 4826 | 29Gam Vir | 124139.6 | -012658 | F0V | 3.50 | 0.36 | 30 | 84.53 |
| 4905 | 77Eps UMa | 125401.7 | +555735 | A0pCr | 1.77 | -0.02 | 38 | 40.30 |
| 4915 | 12Alp2CVn | 125601.7 | +381906 | A0pSiEuHg | 2.90 | -0.12 | 29 | 29.60 |
| 4931 | 78 UMa | 130043.8 | +562159 | F2V | 4.93 | 0.36 | 92 | 40.06 |
| 4968 | 42Alp Com | 130959.3 | +173146 | F5V | 5.22 | 0.45 | 28 | 51.00 |
| 5017 | 20 CVn | 131732.5 | +403421 | F3III | 4.73 | 0.30 | 17 | 11.39 |
| 5055 | 79Zet UMa | 132356.4 | +545518 | A1m | 3.95 | 0.13 | 57 | 41.40 |
| 5062 | 80 UMa | 132513.5 | +545917 | A5V | 4.01 | 0.16 | 218 | 40.19 |
| 5107 | 79Zet Vir | 133441.6 | -003545 | A3V | 3.37 | 0.11 | 173 | 44.55 |
| 5110 | | 133447.8 | +371057 | F2IV | 4.98 | 0.40 | 16 | 22.46 |
| 5127 | 25 CVn | 133727.6 | +361742 | A7III | 4.82 | 0.23 | 204 | 17.01 |
| 5191 | 85Eta UMa | 134732.4 | +491848 | B3V | 1.86 | -0.19 | 205 | 32.39 |
| 5264 | 93Tau Vir | 140138.8 | +013240 | A3V | 4.26 | 0.10 | 150 | 14.94 |
| 5291 | 11Alp Dra | 140423.3 | +642233 | A0III | 3.65 | -0.05 | 18 | 10.56 |
| 5329 | 17Kap2Boo | 141329.0 | +514725 | A8IV | 4.54 | 0.20 | 127 | 21.03 |
| 5351 | 19Lam Boo | 141623.0 | +460518 | A0p | 4.18 | 0.08 | 110 | 33.58 |
| 5435 | 27Gam Boo | 143204.7 | +381830 | A7III | 3.03 | 0.19 | 139 | 38.29 |

Table 4.1—Continued

| HR | Name | $\alpha$ | $\delta$ 2000 | SpType | V | B-V | $v \sin i$ | $\pi$ |
|---|---|---|---|---|---|---|---|---|
| 5447 | 28Sig Boo | 143440.8 | +294442 | F2V | 4.46 | 0.36 | 14 | 64.66 |
| 5487 | 107Mu Vir | 144303.6 | -053930 | F2III | 3.88 | 0.38 | 54 | 53.54 |
| 5511 | 109 Vir | 144614.9 | +015334 | A0V | 3.72 | -0.01 | 351 | 25.35 |
| 5570 | 16 Lib | 145711.0 | -042047 | F0V | 4.49 | 0.32 | 117 | 35.83 |
| 5634 | 45 Boo | 150718.1 | +245209 | F5V | 4.93 | 0.43 | 45 | 50.70 |
| 5685 | 27Bet Lib | 151700.4 | -092259 | B8V | 2.61 | -0.11 | 230 | 20.38 |
| 5723 | 31Eps Lib | 152411.9 | -101920 | F5IV | 4.94 | 0.44 | 10 | 30.90 |
| 5733 | 51Mu 1Boo | 152429.4 | +372238 | F2IVa | 4.31 | 0.31 | 84 | 26.96 |
| 5789 | 13Del Ser | 153448.1 | +103221 | F0IV | 3.80 | 0.26 | 80 | 15.00 |
| 5793 | 5Alp CrB | 153441.3 | +264253 | A0V+G5V | 2.23 | -0.02 | 133 | 43.65 |
| 5867 | 28Bet Ser | 154611.3 | +152519 | A2IV | 3.67 | 0.06 | 170 | 21.31 |
| 5881 | 32Mu Ser | 154937.2 | -032549 | A0V | 3.53 | -0.04 | 87 | 20.94 |
| 5892 | 37Eps Ser | 155049.0 | +042840 | A2Vm | 3.71 | 0.15 | 37 | 46.39 |
| 6093 | 50Sig Ser | 162204.4 | +010145 | F0V | 4.82 | 0.34 | 80 | 36.56 |
| 6095 | 20Gam Her | 162155.2 | +190911 | A9III | 3.75 | 0.27 | 141 | 16.69 |
| 6116 | 21Eta UMi | 161730.3 | +754519 | F5V | 4.95 | 0.37 | 76 | 33.52 |
| 6129 | 3Ups Oph | 162748.1 | -082218 | A3m | 4.63 | 0.17 | 44 | 26.67 |
| 6237 |  | 164517.8 | +564655 | F2V | 4.85 | 0.38 | 53 | 37.41 |
| 6324 | 58Eps Her | 170017.4 | +305535 | A0V | 3.92 | -0.01 | 78 | 20.04 |
| 6410 | 65Del Her | 171501.9 | +245021 | A3IV | 3.14 | 0.08 | 290 | 41.55 |
| 6554 | 24Nu 1Dra | 173210.6 | +551103 | A6V | 4.88 | 0.26 | 66 | 32.96 |
| 6555 | 25Nu 2Dra | 173216.0 | +551023 | A4m v | 4.87 | 0.28 | 50 | 32.64 |
| 6556 | 55Alp Oph | 173456.1 | +123336 | A5III | 2.08 | 0.15 | 219 | 69.84 |
| 6581 | 56Omi Ser | 174124.9 | -125231 | A2V | 4.26 | 0.08 | 125 | 19.41 |
| 6596 | 28Ome Dra | 173657.1 | +684529 | F5V | 4.80 | 0.43 | 26 | 42.62 |
| 6629 | 62Gam Oph | 174753.6 | +024226 | A0Vnp | 3.75 | 0.04 | 205 | 34.42 |
| 6636 | 31Psi1Dra | 174156.3 | +720856 | F5IV-V | 4.58 | 0.42 | 14 | 45.38 |
| 6710 | 57Zet Ser | 180029.0 | -034125 | F2IV | 4.62 | 0.38 | 70 | 43.11 |
| 6771 | 72 Oph | 180721.0 | +093350 | A4IV s | 3.73 | 0.12 | 80 | 39.40 |
| 6779 | 103Omi Her | 180732.6 | +284545 | B9.5V e | 3.83 | -0.03 | 134 | 9.39 |
| 6850 | 36 Dra | 181353.8 | +642350 | F5V | 5.03 | 0.38 | 8 | 42.56 |
| 7020 | Del Sct | 184216.4 | -090309 | F2IIIpDelDel | 4.72 | 0.35 | 32 | 17.44 |
| 7056 | 6Zet1Lyr | 184446.4 | +373618 | A4m v | 4.36 | 0.19 | 27 | 21.23 |
| 7069 | 111 Her | 184701.3 | +181053 | A5III | 4.36 | 0.13 | 79 | 35.17 |
| 7141 | 63The1Ser | 185613.2 | +041213 | A5V | 4.62 | 0.17 | 143 | 22.84 |
| 7235 | 17Zet Aql | 190524.6 | +135148 | A0Vn | 2.99 | 0.01 | 317 | 39.18 |
| 7236 | 16Lam Aql | 190614.9 | -045257 | B9Vn | 3.44 | -0.09 | 176 | 26.05 |
| 7266 | 19 Aql | 190859.9 | +060424 | F0III-IV | 5.22 | 0.35 | 104 | 22.96 |
| 7377 | 30Del Aql | 192529.9 | +030653 | F3IV | 3.36 | 0.32 | 85 | 65.05 |
| 7420 | 10Iot2Cyg | 192942.3 | +514347 | A5Vn | 3.79 | 0.14 | 226 | 26.63 |
| 7460 | 42 Aql | 193747.3 | -043851 | F3IV | 5.46 | 0.43 | 82 | 31.14 |
| 7469 | 13The Cyg | 193626.5 | +501316 | F4V | 4.48 | 0.38 | 7 | 53.78 |
| 7495 |  | 194050.2 | +453130 | F5II-III | 5.06 | 0.40 | 42 | 20.51 |
| 7528 | 18Del Cyg | 194458.5 | +450751 | B9.5IV+F1V | 2.87 | -0.03 | 149 | 19.07 |
| 7653 | 15 Vul | 200106.1 | +274513 | A4III | 4.64 | 0.18 | 23 | 14.67 |
| 7657 | 16 Vul | 200201.4 | +245617 | F2III | 5.22 | 0.36 | 121 | 15.43 |
| 7740 | 33 Cyg | 201323.9 | +563404 | A3IV-Vn | 4.30 | 0.11 | 268 | 21.41 |
| 7850 | 2The Cep | 202934.9 | +625939 | A7III | 4.22 | 0.20 | 59 | 24.04 |
| 7928 | 11Del Del | 204327.5 | +150428 | A7IIIpDelDel | 4.43 | 0.32 | 41 | 16.03 |
| 7950 | 2Eps Aqr | 204740.6 | -092945 | A1V | 3.77 | 0.00 | 98 | 14.21 |
| 7990 | 6Mu Aqr | 205239.2 | -085900 | A3m | 4.73 | 0.32 | 46 | 21.01 |

Table 4.1—Continued

| HR | Name | $\alpha$ | $\delta$ 2000 | SpType | V | B-V | $v \sin i$ | $\pi$ |
|---|---|---|---|---|---|---|---|---|
| 8028 | 58Nu Cyg | 205710.4 | +411002 | A1Vn | 3.94 | 0.02 | 241 | 9.17 |
| 8097 | 5Gam Equ | 211020.5 | +100754 | F0IIIp v | 4.69 | 0.26 | 8 | 28.38 |
| 8130 | 65Tau Cyg | 211447.5 | +380244 | F2IV | 3.72 | 0.39 | 89 | 47.80 |
| 8162 | 5Alp Cep | 211834.8 | +623508 | A7V | 2.44 | 0.22 | 246 | 66.84 |
| 8344 | 13 Peg | 215008.7 | +171708 | F2III-IV | 5.29 | 0.37 | 71 | 29.91 |
| 8351 | 51Mu Cap | 215317.8 | -133306 | F1III | 5.08 | 0.37 | 87 | 36.15 |
| 8400 | 16 Cep | 215915.0 | +731048 | F5V | 5.03 | 0.44 | 26 | 26.67 |
| 8430 | 24Iot Peg | 220700.7 | +252042 | F5V | 3.76 | 0.44 | 7 | 85.06 |
| 8450 | 26The Peg | 221012.0 | +061152 | A2Vp | 3.53 | 0.08 | 117 | 33.77 |
| 8494 | 23Eps Cep | 221502.0 | +570237 | F0IV | 4.19 | 0.28 | 86 | 38.86 |
| 8518 | 48Gam Aqr | 222139.4 | -012314 | A0V | 3.84 | -0.05 | 57 | 20.67 |
| 8559 | 55Zet2Aqr | 222850.1 | -000112 | F3V | 4.42 | 0.38 | 58 | 13.00 |
| 8585 | 7Alp Lac | 223117.5 | +501657 | A1V | 3.77 | 0.01 | 146 | 31.86 |
| 8613 | 9 Lac | 223722.4 | +513243 | A8IV | 4.63 | 0.24 | 87 | 18.95 |
| 8615 | 31 Cep | 223546.1 | +733835 | F3III-IV | 5.08 | 0.39 | 85 | 17.70 |
| 8634 | 42Zet Peg | 224127.7 | +104953 | B8V | 3.40 | -0.09 | 194 | 15.64 |
| 8781 | 54Alp Peg | 230445.7 | +151219 | B9V | 2.49 | -0.04 | 148 | 23.36 |
| 8830 | 7 And | 231233.0 | +492423 | F0V | 4.52 | 0.29 | 59 | 40.82 |
| 8880 | 62Tau Peg | 232038.2 | +234425 | A5Vp | 4.60 | 0.17 | 143 | 19.50 |
| 8984 | 18Lam Psc | 234202.8 | +014648 | A7V | 4.50 | 0.20 | 63 | 32.38 |
| 9072 | 28Ome Psc | 235918.7 | +065148 | F4IV | 4.01 | 0.42 | 38 | 30.78 |

Table 4.2. Estimated physical parameters of the preliminary targets for NPOI 80 m baseline

| HR | $\omega_{90}$ | $i_c$ [a] | $i^{th}_{obl.}$ | $i^{th}_{asy.}$ | $i^{th}_{\Delta\phi}$ | $T_{90}$ | $T_c$ | $M_{90}$ | $M_c$ | $\theta^{max}_{90}$ | $\theta^{min}_{90}$ | $\theta^{max}_{c}$ | $\theta^{min}_{c}$ | $P_{obl.}$ | $P_{asy.}$ | $P(\Delta\phi)$ | comments |
|---|---|---|---|---|---|---|---|---|---|---|---|---|---|---|---|---|---|
| 15 | 0.21 | 7.37 | 25.99 | 7.38 | 7.38 | 12993.7 | 14931.2 | 3.70 | 3.37 | 0.94 | 0.93 | 0.98 | 0.97 | 0.09 | 0.00 | 0.00 | |
| 21 | 0.37 | 14.33 | 71.82 | 66.84 | 47.14 | 7208.2 | 7798.5 | 2.05 | 1.79 | 1.92 | 1.88 | 2.19 | 2.13 | 0.68 | 0.60 | 0.30 | |
| 82 | 0.22 | 8.20 | 16.50 | 8.20 | 8.20 | 6766.0 | 7401.9 | 1.81 | 1.58 | 0.56 | 0.55 | 0.64 | 0.63 | 0.03 | 0.00 | 0.00 | |
| 269 | 0.34 | 12.86 | 32.74 | 12.86 | 12.86 | 8356.3 | 9273.7 | 2.26 | 2.00 | 0.68 | 0.67 | 0.75 | 0.73 | 0.14 | 0.00 | 0.00 | |
| 343 | 0.46 | 17.88 | 40.89 | 17.89 | 17.89 | 8281.2 | 9001.8 | 2.07 | 1.84 | 0.58 | 0.56 | 0.65 | 0.62 | 0.21 | 0.00 | 0.00 | |
| 403 | 0.55 | 22.40 | 90.00 | 22.39 | 61.48 | 8488.2 | 9176.8 | 2.52 | 2.23 | 1.22 | 1.16 | 1.36 | 1.27 | 1.00 | 0.00 | 0.49 | |
| 417 | 0.32 | 12.27 | 28.87 | 12.27 | 12.27 | 6849.1 | 7461.6 | 1.53 | 1.36 | 0.65 | 0.64 | 0.75 | 0.73 | 0.10 | 0.00 | 0.00 | |
| 531 | 0.25 | 28.91 | 28.89 | 28.89 | 28.89 | 7320.8 | 7397.8 | 1.53 | 1.54 | 0.61 | 0.60 | 0.61 | 0.60 | 0.00 | 0.00 | 0.00 | w=0.500 |
| 553 | 0.34 | 12.77 | 46.96 | 12.77 | 21.47 | 8475.5 | 9420.2 | 2.04 | 1.84 | 1.17 | 1.15 | 1.29 | 1.26 | 0.30 | 0.00 | 0.05 | |
| 569 | 0.45 | 17.71 | 32.87 | 17.71 | 17.71 | 7621.9 | 8267.4 | 1.83 | 1.63 | 0.55 | 0.53 | 0.62 | 0.59 | 0.12 | 0.00 | 0.00 | |
| 575 | 0.28 | 11.85 | 21.51 | 11.85 | 11.85 | 8300.6 | 9043.7 | 1.87 | 1.74 | 0.50 | 0.50 | 0.53 | 0.52 | 0.05 | 0.00 | 0.00 | w=0.971 |
| 623 | 0.82 | 40.95 | 90.00 | 40.96 | 64.01 | 7879.8 | 7842.5 | 2.61 | 2.37 | 0.60 | 0.52 | 0.72 | 0.57 | 1.00 | 0.00 | 0.43 | |
| 646 | 0.04 | 1.51 | 2.20 | 1.51 | 1.51 | 6719.4 | 7416.7 | 1.44 | 1.31 | 0.54 | 0.54 | 0.61 | 0.61 | 0.00 | 0.00 | 0.00 | |
| 664 | 0.73 | 38.42 | 76.41 | 38.74 | 38.74 | 10240.3 | 10767.9 | 2.31 | 2.20 | 0.55 | 0.50 | 0.56 | 0.50 | 0.71 | 0.00 | 0.00 | w=0.956 |
| 813 | 0.24 | 8.96 | 21.31 | 8.96 | 8.96 | 7378.0 | 8112.9 | 1.67 | 1.51 | 0.71 | 0.71 | 0.80 | 0.79 | 0.06 | 0.00 | 0.00 | |
| 838 | 0.60 | 31.66 | 45.97 | 31.69 | 31.69 | 13123.5 | 13834.0 | 3.40 | 3.20 | 0.48 | 0.45 | 0.49 | 0.46 | 0.19 | 0.00 | 0.00 | w=0.928 |
| 840 | 0.70 | 31.76 | 90.00 | 31.77 | 64.98 | 7638.6 | 7860.6 | 2.04 | 1.81 | 0.81 | 0.74 | 0.95 | 0.82 | 1.00 | 0.00 | 0.51 | |
| 855 | 0.36 | 13.78 | 24.90 | 13.78 | 13.78 | 6865.9 | 7426.1 | 2.10 | 1.83 | 0.52 | 0.51 | 0.60 | 0.58 | 0.07 | 0.00 | 0.00 | |
| 984 | 0.29 | 11.13 | 17.55 | 11.07 | 11.07 | 7866.7 | 8607.2 | 1.77 | 1.63 | 0.49 | 0.49 | 0.54 | 0.53 | 0.03 | 0.00 | 0.00 | w=0.992 |
| 1069 | 0.14 | 5.05 | 9.70 | 5.05 | 5.05 | 6875.0 | 7569.7 | 1.55 | 1.38 | 0.51 | 0.50 | 0.57 | 0.57 | 0.01 | 0.00 | 0.00 | |
| 1251 | 0.29 | 10.39 | 22.43 | 10.40 | 10.40 | 9337.0 | 10653.4 | 2.31 | 2.12 | 0.56 | 0.56 | 0.60 | 0.59 | 0.06 | 0.00 | 0.00 | |
| 1298 | 0.49 | 19.89 | 58.87 | 19.88 | 34.81 | 7354.3 | 7860.2 | 2.08 | 1.82 | 0.85 | 0.81 | 0.97 | 0.92 | 0.46 | 0.00 | 0.15 | |
| 1387 | 0.38 | 14.28 | 30.05 | 14.28 | 14.28 | 8404.3 | 9295.0 | 2.22 | 1.97 | 0.58 | 0.57 | 0.64 | 0.62 | 0.11 | 0.00 | 0.00 | |
| 1392 | 0.85 | 43.94 | 90.00 | 43.95 | 70.93 | 8452.7 | 8379.9 | 2.25 | 2.05 | 0.74 | 0.63 | 0.89 | 0.68 | 1.00 | 0.00 | 0.55 | |
| 1394 | 0.82 | 40.85 | 89.94 | 40.81 | 62.47 | 8421.7 | 8444.7 | 2.16 | 1.95 | 0.65 | 0.57 | 0.78 | 0.61 | 1.00 | 0.00 | 0.40 | |
| 1412 | 0.40 | 15.53 | 42.10 | 15.53 | 18.73 | 7968.8 | 8750.1 | 2.40 | 2.10 | 0.80 | 0.78 | 0.89 | 0.86 | 0.23 | 0.00 | 0.02 | |
| 1412 | 0.48 | 18.69 | 30.67 | 18.69 | 18.69 | 8274.6 | 8973.3 | 1.97 | 1.76 | 0.48 | 0.46 | 0.54 | 0.51 | 0.09 | 0.00 | 0.00 | |
| 1444 | 0.55 | 22.16 | 42.65 | 22.15 | 27.85 | 7848.2 | 8403.0 | 2.01 | 1.78 | 0.57 | 0.54 | 0.65 | 0.60 | 0.21 | 0.00 | 0.05 | |
| 1473 | 0.36 | 13.50 | 27.05 | 13.51 | 13.51 | 8485.5 | 9433.4 | 2.18 | 1.95 | 0.55 | 0.54 | 0.61 | 0.59 | 0.08 | 0.00 | 0.00 | |
| 1560 | 0.77 | 36.13 | 84.88 | 36.10 | 57.09 | 8156.0 | 8284.0 | 2.56 | 2.31 | 0.69 | 0.61 | 0.81 | 0.67 | 0.89 | 0.00 | 0.35 | |
| 1637 | 0.06 | 0.00 | 0.00 | 0.00 | 0.00 | 7274.3 | 0.0 | 1.53 | 0.00 | 0.52 | 0.52 | 0.00 | 0.00 | 0.00 | 0.00 | 0.00 | ZAMS |
| 1641 | 0.39 | 33.27 | 33.28 | 33.28 | 33.28 | 18717.8 | 19031.9 | 5.92 | 5.78 | 0.42 | 0.41 | 0.43 | 0.42 | 0.00 | 0.00 | 0.00 | w=0.658 |
| 1666 | 0.77 | 35.39 | 90.00 | 35.42 | 67.89 | 8994.2 | 9319.7 | 2.39 | 2.16 | 1.19 | 1.06 | 1.36 | 1.14 | 1.00 | 0.00 | 0.56 | |
| 1673 | 0.04 | 2.45 | 3.14 | 2.45 | 2.45 | 6683.2 | 7050.8 | 1.38 | 1.35 | 0.58 | 0.58 | 0.60 | 0.60 | 0.00 | 0.00 | 0.00 | w=0.848 |
| 1676 | 0.34 | 12.78 | 24.65 | 12.78 | 12.78 | 7164.3 | 7775.6 | 2.53 | 2.30 | 0.59 | 0.58 | 0.67 | 0.66 | 0.07 | 0.00 | 0.00 | |
| 1790 | 0.20 | 6.88 | 19.76 | 6.88 | 6.88 | 22361.2 | 25532.2 | 8.79 | 8.27 | 0.72 | 0.71 | 0.75 | 0.75 | 0.05 | 0.00 | 0.00 | |
| 1791 | 0.29 | 10.53 | 39.82 | 10.54 | 10.54 | 13967.3 | 15725.0 | 4.67 | 4.20 | 1.07 | 1.06 | 1.13 | 1.12 | 0.22 | 0.00 | 0.00 | |
| 1998 | 0.70 | 0.00 | 0.00 | 0.00 | 0.00 | 9374.8 | 0.0 | 1.96 | 0.00 | 0.75 | 0.69 | 0.00 | 0.00 | 0.67 | 0.00 | 0.00 | ZAMS |
| 2085 | 0.08 | 10.93 | 10.92 | 10.92 | 10.92 | 7275.1 | 7346.7 | 1.53 | 1.53 | 0.94 | 0.94 | 0.94 | 0.94 | 0.00 | 0.00 | 0.00 | w=0.424 |
| 2095 | 0.23 | 8.17 | 27.25 | 8.18 | 8.18 | 11112.8 | 12907.5 | 3.71 | 3.36 | 0.84 | 0.83 | 0.87 | 0.86 | 0.10 | 0.00 | 0.00 | |
| 2124 | 0.12 | 4.37 | 9.72 | 4.37 | 4.37 | 8070.6 | 8984.6 | 2.23 | 1.96 | 0.62 | 0.62 | 0.70 | 0.70 | 0.01 | 0.00 | 0.00 | |
| 2220 | 0.05 | 0.00 | 0.00 | 0.00 | 0.00 | 6702.8 | 0.0 | 1.37 | 0.00 | 0.56 | 0.56 | 0.00 | 0.00 | 0.00 | 0.00 | 0.00 | ZAMS |
| 2241 | 0.07 | 0.00 | 0.00 | 0.00 | 0.00 | 6803.9 | 0.0 | 1.43 | 0.00 | 0.59 | 0.58 | 0.00 | 0.00 | 0.00 | 0.00 | 0.00 | ZAMS |
| 2264 | 0.08 | 2.86 | 4.91 | 2.87 | 2.87 | 6689.5 | 7343.9 | 1.87 | 1.62 | 0.52 | 0.52 | 0.60 | 0.59 | 0.00 | 0.00 | 0.00 | |
| 2298 | 0.53 | 21.21 | 40.75 | 21.23 | 23.51 | 8345.1 | 8986.4 | 1.98 | 1.77 | 0.56 | 0.53 | 0.63 | 0.59 | 0.19 | 0.00 | 0.02 | |
| 2421 | 0.17 | 5.95 | 23.35 | 5.95 | 5.95 | 9266.3 | 10660.3 | 3.09 | 2.76 | 1.40 | 1.39 | 1.49 | 1.48 | 0.08 | 0.00 | 0.00 | |
| 2484 | 0.35 | 13.42 | 48.33 | 13.44 | 34.52 | 6797.8 | 7391.9 | 1.66 | 1.46 | 1.31 | 1.29 | 1.50 | 1.47 | 0.32 | 0.00 | 0.18 | |
| 2540 | 0.65 | 27.19 | 85.83 | 27.19 | 44.36 | 8767.4 | 9389.5 | 2.84 | 2.54 | 0.79 | 0.73 | 0.88 | 0.79 | 0.92 | 0.00 | 0.21 | |

Table 4.2—Continued

| HR | $\omega_{90}$ | $i_c$[a] | $i^{th}_{obl.}$ | $i^{th}_{asy.}$ | $i^{th}_{\Delta\phi}$ | $T_{90}$ | $T_c$ | $M_{90}$ | $M_c$ | $\theta^{max}_{90}$ | $\theta^{min}_{90}$ | $\theta^{max}_{c}$ | $\theta^{min}_{c}$ | $P_{obl.}$ | $P_{asy.}$ | $P(\Delta\phi)$ | comments |
|---|---|---|---|---|---|---|---|---|---|---|---|---|---|---|---|---|---|
| 2564 | 0.52 | 26.47 | 41.79 | 26.21 | 29.41 | 7661.5 | 8048.7 | 1.64 | 1.56 | 0.60 | 0.57 | 0.62 | 0.59 | 0.17 | 0.00 | 0.03 | w=0.930 |
| 2763 | 0.62 | 25.46 | 77.52 | 25.47 | 36.18 | 8947.8 | 9659.1 | 2.11 | 1.91 | 0.76 | 0.71 | 0.84 | 0.77 | 0.77 | 0.00 | 0.12 | |
| 2777 | 0.49 | 19.42 | 77.04 | 19.41 | 44.69 | 7395.9 | 7938.3 | 1.66 | 1.49 | 1.07 | 1.02 | 1.21 | 1.15 | 0.77 | 0.00 | 0.27 | |
| 2849 | 0.05 | 0.00 | 0.00 | 0.00 | 0.00 | 6667.7 | 0.0 | 1.41 | 0.00 | 0.53 | 0.53 | 0.00 | 0.00 | 0.00 | 0.00 | 0.00 | ZAMS |
| 2852 | 0.27 | 0.00 | 0.00 | 0.00 | 0.00 | 7393.9 | 0.0 | 1.56 | 0.00 | 0.75 | 0.74 | 0.00 | 0.00 | 0.00 | 0.00 | 0.00 | ZAMS |
| 2890 | 0.10 | 0.00 | 0.00 | 0.00 | 0.00 | 9578.5 | 0.0 | 2.43 | 0.00 | 0.86 | 0.86 | 0.00 | 0.00 | 0.00 | 0.00 | 0.00 | ZAMS |
| 2891 | 0.06 | 2.20 | 8.37 | 2.19 | 2.19 | 9309.5 | 10531.9 | 2.25 | 2.08 | 1.35 | 1.35 | 1.41 | 1.41 | 0.01 | 0.00 | 0.00 | w=0.989 |
| 2927 | 0.12 | 4.36 | 8.71 | 4.36 | 4.36 | 6640.5 | 7266.0 | 2.04 | 1.77 | 0.59 | 0.59 | 0.68 | 0.68 | 0.01 | 0.00 | 0.00 | |
| 2930 | 0.46 | 18.48 | 40.27 | 18.47 | 21.82 | 7006.0 | 7509.4 | 1.92 | 1.68 | 0.63 | 0.60 | 0.72 | 0.69 | 0.20 | 0.00 | 0.02 | |
| 3015 | 0.54 | 22.17 | 38.15 | 22.17 | 26.67 | 7382.3 | 7829.7 | 2.25 | 1.98 | 0.54 | 0.51 | 0.62 | 0.58 | 0.15 | 0.00 | 0.04 | |
| 3314 | 0.47 | 24.10 | 34.48 | 24.10 | 24.10 | 10332.4 | 11040.7 | 2.45 | 2.34 | 0.52 | 0.50 | 0.52 | 0.50 | 0.10 | 0.00 | 0.00 | w=0.911 |
| 3572 | 0.33 | 12.56 | 26.27 | 12.56 | 12.56 | 8267.0 | 9137.3 | 2.32 | 2.05 | 0.58 | 0.57 | 0.65 | 0.63 | 0.08 | 0.00 | 0.00 | |
| 3619 | 0.16 | 6.52 | 13.65 | 6.48 | 6.48 | 7553.5 | 8309.5 | 1.70 | 1.57 | 0.61 | 0.61 | 0.65 | 0.64 | 0.02 | 0.00 | 0.00 | w=0.983 |
| 3624 | 0.09 | 3.33 | 8.07 | 3.33 | 3.33 | 7089.9 | 7809.7 | 1.78 | 1.56 | 0.63 | 0.63 | 0.71 | 0.71 | 0.01 | 0.00 | 0.00 | |
| 3690 | 0.66 | 27.14 | 78.38 | 27.16 | 32.39 | 9446.0 | 10236.5 | 2.29 | 2.09 | 0.64 | 0.59 | 0.70 | 0.63 | 0.78 | 0.00 | 0.06 | |
| 3757 | 0.63 | 26.60 | 90.00 | 26.60 | 68.70 | 7587.6 | 7975.4 | 1.81 | 1.60 | 1.01 | 0.94 | 1.16 | 1.05 | 1.00 | 0.00 | 0.59 | |
| 3888 | 0.55 | 22.38 | 88.94 | 22.38 | 54.34 | 7605.5 | 8107.0 | 2.10 | 1.85 | 0.90 | 0.86 | 1.03 | 0.96 | 0.98 | 0.00 | 0.37 | |
| 3974 | 0.55 | 0.00 | 0.00 | 0.00 | 0.00 | 8496.4 | 0.0 | 1.77 | 0.00 | 0.53 | 0.51 | 0.00 | 0.00 | 0.00 | 0.00 | 0.00 | ZAMS |
| 4033 | 0.22 | 7.96 | 22.39 | 7.97 | 7.97 | 9165.3 | 10450.2 | 2.53 | 2.28 | 0.71 | 0.70 | 0.76 | 0.75 | 0.07 | 0.00 | 0.00 | |
| 4054 | 0.07 | 3.76 | 5.79 | 3.76 | 3.76 | 6644.7 | 7042.4 | 1.37 | 1.33 | 0.69 | 0.69 | 0.71 | 0.71 | 0.00 | 0.00 | 0.00 | w=0.870 |
| 4084 | 0.36 | 0.00 | 0.00 | 0.00 | 0.00 | 7196.7 | 0.0 | 1.72 | 0.00 | 0.49 | 0.48 | 0.00 | 0.00 | 0.00 | 0.00 | 0.00 | ZAMS |
| 4090 | 0.17 | 6.18 | 12.08 | 6.19 | 6.19 | 7519.9 | 8293.8 | 2.23 | 1.95 | 0.54 | 0.54 | 0.61 | 0.61 | 0.02 | 0.00 | 0.00 | |
| 4132 | 0.54 | 24.07 | 40.38 | 24.07 | 25.58 | 8087.8 | 8600.0 | 1.76 | 1.65 | 0.51 | 0.49 | 0.55 | 0.52 | 0.17 | 0.00 | 0.01 | w=0.976 |
| 4141 | 0.34 | 0.00 | 0.00 | 0.00 | 0.00 | 7327.1 | 0.0 | 1.56 | 0.00 | 0.49 | 0.48 | 0.00 | 0.00 | 0.00 | 0.00 | 0.00 | ZAMS |
| 4295 | 0.17 | 5.84 | 22.27 | 5.84 | 5.84 | 9884.4 | 11497.4 | 2.62 | 2.41 | 1.06 | 1.05 | 1.11 | 1.10 | 0.07 | 0.00 | 0.00 | |
| 4310 | 0.11 | 4.13 | 8.82 | 4.13 | 4.13 | 7250.8 | 7999.7 | 1.63 | 1.48 | 0.62 | 0.62 | 0.70 | 0.69 | 0.01 | 0.00 | 0.00 | |
| 4357 | 0.70 | 30.78 | 90.00 | 30.78 | 66.56 | 9068.5 | 9574.5 | 2.10 | 1.90 | 1.25 | 1.14 | 1.41 | 1.23 | 1.00 | 0.00 | 0.55 | |
| 4359 | 0.10 | 3.50 | 9.58 | 3.50 | 3.50 | 9473.4 | 10958.1 | 2.97 | 2.66 | 0.71 | 0.71 | 0.75 | 0.75 | 0.01 | 0.00 | 0.00 | |
| 4368 | 0.91 | 53.65 | 89.81 | 53.66 | 70.98 | 9091.9 | 8840.2 | 2.45 | 2.30 | 0.67 | 0.54 | 0.81 | 0.60 | 0.99 | 0.00 | 0.46 | |
| 4399 | 0.10 | 3.79 | 11.20 | 3.80 | 3.80 | 6800.7 | 7478.7 | 1.70 | 1.49 | 0.97 | 0.97 | 1.10 | 1.10 | 0.02 | 0.00 | 0.00 | |
| 4534 | 0.45 | 0.00 | 0.00 | 0.00 | 0.00 | 9067.3 | 0.0 | 1.93 | 0.00 | 1.37 | 1.32 | 0.00 | 0.00 | 0.42 | 0.00 | 0.00 | ZAMS |
| 4554 | 0.67 | 27.83 | 90.00 | 27.83 | 53.57 | 10128.7 | 11082.9 | 2.64 | 2.42 | 1.12 | 1.03 | 1.20 | 1.07 | 1.00 | 0.00 | 0.33 | |
| 4646 | 0.34 | 15.54 | 25.07 | 15.68 | 15.68 | 7344.4 | 7864.2 | 1.59 | 1.51 | 0.49 | 0.48 | 0.52 | 0.51 | 0.06 | 0.00 | 0.00 | w=0.950 |
| 4660 | 0.67 | 28.09 | 90.00 | 28.10 | 48.90 | 9355.0 | 10070.6 | 2.14 | 1.96 | 0.83 | 0.76 | 0.91 | 0.81 | 1.00 | 0.00 | 0.26 | |
| 4733 | 0.95 | 62.56 | 89.86 | 62.53 | 78.13 | 8944.4 | 8583.7 | 2.62 | 2.49 | 0.61 | 0.48 | 0.75 | 0.54 | 0.99 | 0.00 | 0.56 | |
| 4753 | 0.50 | 20.09 | 32.83 | 20.09 | 20.09 | 6900.9 | 7355.5 | 1.97 | 1.73 | 0.50 | 0.48 | 0.58 | 0.55 | 0.11 | 0.00 | 0.00 | |
| 4825 | 0.11 | 0.00 | 0.00 | 0.00 | 0.00 | 7122.1 | 0.0 | 1.49 | 0.00 | 1.09 | 1.09 | 0.00 | 0.00 | 0.00 | 0.00 | 0.00 | ZAMS |
| 4826 | 0.12 | 0.00 | 0.00 | 0.00 | 0.00 | 7123.6 | 0.0 | 1.50 | 0.00 | 1.08 | 1.08 | 0.00 | 0.00 | 0.00 | 0.00 | 0.00 | ZAMS |
| 4905 | 0.18 | 6.39 | 26.97 | 6.39 | 6.39 | 9709.4 | 11228.3 | 2.93 | 2.64 | 1.43 | 1.42 | 1.50 | 1.49 | 0.10 | 0.00 | 0.00 | |
| 4915 | 0.09 | 0.00 | 0.00 | 0.00 | 0.00 | 13931.3 | 0.0 | 3.61 | 0.00 | 0.60 | 0.60 | 0.00 | 0.00 | 0.00 | 0.00 | 0.00 | ZAMS |
| 4931 | 0.38 | 41.97 | 41.97 | 41.97 | 41.97 | 7221.7 | 7293.0 | 1.50 | 1.50 | 0.57 | 0.56 | 0.57 | 0.56 | 0.00 | 0.00 | 0.00 | w=0.542 |
| 4968 | 0.11 | 0.00 | 0.00 | 0.00 | 0.00 | 6671.4 | 0.0 | 1.40 | 0.00 | 0.56 | 0.56 | 0.00 | 0.00 | 0.00 | 0.00 | 0.00 | ZAMS |
| 5017 | 0.11 | 3.91 | 8.62 | 3.91 | 3.91 | 7179.0 | 7882.0 | 2.50 | 2.24 | 0.59 | 0.59 | 0.67 | 0.67 | 0.01 | 0.00 | 0.00 | |
| 5055 | 0.22 | 27.10 | 27.09 | 27.09 | 27.09 | 8564.6 | 8655.3 | 1.84 | 1.83 | 0.62 | 0.62 | 0.62 | 0.62 | 0.00 | 0.00 | 0.00 | w=0.469 |
| 5062 | 0.76 | 61.08 | 90.00 | 61.07 | 61.90 | 9043.4 | 9122.1 | 1.88 | 1.86 | 0.67 | 0.60 | 0.68 | 0.61 | 1.00 | 0.00 | 0.03 | w=0.831 |
| 5107 | 0.65 | 30.61 | 80.17 | 30.60 | 42.51 | 9095.8 | 9641.8 | 2.01 | 1.87 | 0.83 | 0.77 | 0.88 | 0.81 | 0.81 | 0.00 | 0.16 | w=0.978 |
| 5110 | 0.08 | 3.13 | 6.52 | 3.13 | 3.13 | 6834.0 | 7510.9 | 1.80 | 1.57 | 0.59 | 0.59 | 0.67 | 0.67 | 0.00 | 0.00 | 0.00 | |
| 5127 | 0.85 | 44.18 | 90.00 | 44.15 | 66.48 | 8651.9 | 8599.4 | 2.22 | 2.03 | 0.55 | 0.47 | 0.66 | 0.50 | 1.00 | 0.00 | 0.45 | |

Table 4.2—Continued

| HR | $\omega_{90}$ | $i_c$[a] | $i^{th}_{obl.}$ | $i^{th}_{asy.}$ | $i^{th}_{\Delta\phi}$ | $T_{90}$ | $T_c$ | $M_{90}$ | $M_c$ | $\theta^{max}_{90}$ | $\theta^{min}_{90}$ | $\theta^{max}_{c}$ | $\theta^{min}_{c}$ | $P_{obl.}$ | $P_{asy.}$ | $P(\Delta\phi)$ | comments |
|---|---|---|---|---|---|---|---|---|---|---|---|---|---|---|---|---|---|
| 5191 | 0.52 | 0.00 | 0.00 | 0.00 | 0.00 | 20287.2 | 0.0 | 5.89 | 0.00 | 0.75 | 0.71 | 0.00 | 0.00 | 0.33 | 0.00 | 0.00 | ZAMS |
| 5264 | 0.69 | 30.24 | 66.88 | 30.23 | 37.39 | 8954.0 | 9498.8 | 2.63 | 2.35 | 0.58 | 0.53 | 0.65 | 0.57 | 0.57 | 0.00 | 0.09 | |
| 5291 | 0.10 | 3.37 | 8.55 | 3.36 | 3.36 | 9956.2 | 11652.5 | 3.61 | 3.27 | 0.58 | 0.58 | 0.60 | 0.60 | 0.01 | 0.00 | 0.00 | |
| 5329 | 0.58 | 23.61 | 52.39 | 23.61 | 31.82 | 8179.0 | 8749.0 | 2.09 | 1.85 | 0.56 | 0.53 | 0.63 | 0.59 | 0.34 | 0.00 | 0.08 | |
| 5351 | 0.41 | 50.91 | 51.07 | 51.07 | 51.07 | 9107.6 | 9164.2 | 1.97 | 1.96 | 0.53 | 0.51 | 0.53 | 0.51 | 0.00 | 0.00 | 0.00 | w=0.517 |
| 5435 | 0.63 | 26.76 | 90.00 | 26.76 | 64.48 | 8294.5 | 8800.1 | 2.18 | 1.94 | 1.13 | 1.05 | 1.28 | 1.15 | 1.00 | 0.00 | 0.52 | |
| 5447 | 0.05 | 0.00 | 0.00 | 0.00 | 0.00 | 7150.2 | 0.0 | 1.74 | 0.00 | 0.69 | 0.69 | 0.00 | 0.00 | 0.00 | 0.00 | 0.00 | ZAMS |
| 5487 | 0.25 | 9.17 | 26.75 | 9.17 | 9.17 | 7011.7 | 7694.0 | 1.55 | 1.40 | 0.95 | 0.94 | 1.08 | 1.06 | 0.10 | 0.00 | 0.00 | |
| 5511 | 0.97 | 64.19 | 89.80 | 64.17 | 70.17 | 12544.7 | 12502.9 | 2.84 | 2.75 | 0.69 | 0.52 | 0.75 | 0.54 | 0.99 | 0.00 | 0.22 | |
| 5570 | 0.51 | 19.98 | 44.96 | 19.98 | 27.13 | 7526.3 | 8070.2 | 1.67 | 1.50 | 0.66 | 0.64 | 0.75 | 0.71 | 0.25 | 0.00 | 0.06 | |
| 5634 | 0.18 | 0.00 | 0.00 | 0.00 | 0.00 | 6768.3 | 0.0 | 1.38 | 0.00 | 0.63 | 0.62 | 0.00 | 0.00 | 0.00 | 0.00 | 0.00 | ZAMS |
| 5685 | 0.80 | 36.43 | 85.75 | 36.45 | 38.82 | 14126.8 | 14881.3 | 4.16 | 3.81 | 0.79 | 0.69 | 0.85 | 0.71 | 0.91 | 0.00 | 0.03 | |
| 5723 | 0.05 | 1.85 | 3.91 | 1.85 | 1.85 | 6659.7 | 7328.2 | 1.57 | 1.38 | 0.64 | 0.64 | 0.73 | 0.73 | 0.00 | 0.00 | 0.00 | |
| 5733 | 0.41 | 16.07 | 40.53 | 16.08 | 20.31 | 7403.0 | 8028.1 | 1.92 | 1.69 | 0.72 | 0.70 | 0.81 | 0.78 | 0.21 | 0.00 | 0.03 | |
| 5789 | 0.49 | 19.27 | 59.97 | 19.27 | 32.94 | 7558.5 | 8094.1 | 2.66 | 2.41 | 0.88 | 0.85 | 1.01 | 0.96 | 0.48 | 0.00 | 0.13 | |
| 5793 | 0.54 | 20.45 | 84.70 | 20.46 | 30.37 | 10212.6 | 11558.0 | 2.66 | 2.46 | 1.16 | 1.11 | 1.21 | 1.14 | 0.90 | 0.00 | 0.09 | |
| 5867 | 0.73 | 32.00 | 83.43 | 31.99 | 42.64 | 9451.8 | 10044.0 | 2.58 | 2.33 | 0.71 | 0.65 | 0.79 | 0.68 | 0.87 | 0.00 | 0.14 | |
| 5881 | 0.37 | 13.27 | 31.46 | 13.28 | 13.28 | 10327.0 | 11944.0 | 2.84 | 2.62 | 0.61 | 0.59 | 0.63 | 0.61 | 0.12 | 0.00 | 0.00 | |
| 5892 | 0.15 | 12.50 | 13.11 | 12.50 | 12.50 | 8376.3 | 8575.5 | 1.81 | 1.79 | 0.71 | 0.71 | 0.72 | 0.72 | 0.00 | 0.00 | 0.00 | w=0.626 |
| 6093 | 0.34 | 18.37 | 24.80 | 18.37 | 18.37 | 7303.1 | 7676.2 | 1.55 | 1.51 | 0.58 | 0.57 | 0.59 | 0.58 | 0.04 | 0.00 | 0.00 | w=0.878 |
| 6095 | 0.76 | 35.59 | 90.00 | 35.57 | 67.68 | 7988.4 | 8118.2 | 2.67 | 2.42 | 0.95 | 0.85 | 1.12 | 0.94 | 1.00 | 0.00 | 0.55 | |
| 6116 | 0.34 | 12.63 | 28.55 | 12.63 | 12.63 | 7121.3 | 7773.0 | 1.55 | 1.42 | 0.57 | 0.56 | 0.65 | 0.63 | 0.10 | 0.00 | 0.00 | |
| 6129 | 0.19 | 7.30 | 11.81 | 7.29 | 7.29 | 8183.9 | 9033.2 | 1.87 | 1.72 | 0.49 | 0.48 | 0.53 | 0.52 | 0.01 | 0.00 | 0.00 | w=0.990 |
| 6237 | 0.24 | 10.48 | 19.79 | 10.47 | 10.47 | 7013.3 | 7563.2 | 1.50 | 1.43 | 0.61 | 0.60 | 0.64 | 0.63 | 0.04 | 0.00 | 0.00 | w=0.951 |
| 6324 | 0.34 | 12.01 | 26.23 | 12.01 | 12.01 | 9800.9 | 11269.5 | 2.60 | 2.39 | 0.53 | 0.52 | 0.56 | 0.55 | 0.08 | 0.00 | 0.00 | |
| 6410 | 0.92 | 53.88 | 90.00 | 53.85 | 76.25 | 10477.2 | 10368.3 | 2.31 | 2.16 | 0.99 | 0.80 | 1.15 | 0.86 | 1.00 | 0.00 | 0.60 | |
| 6554 | 0.27 | 24.06 | 24.16 | 24.16 | 24.16 | 7717.6 | 7881.9 | 1.64 | 1.63 | 0.49 | 0.49 | 0.49 | 0.49 | 0.00 | 0.00 | 0.00 | w=0.614 |
| 6555 | 0.21 | 13.02 | 14.82 | 13.02 | 13.02 | 7542.5 | 7903.6 | 1.62 | 1.59 | 0.51 | 0.51 | 0.52 | 0.51 | 0.01 | 0.00 | 0.00 | w=0.795 |
| 6556 | 0.82 | 40.85 | 90.00 | 79.31 | 79.88 | 9184.7 | 9304.5 | 2.12 | 1.93 | 1.70 | 1.47 | 1.97 | 1.56 | 1.00 | 0.77 | 0.77 | |
| 6581 | 0.55 | 21.72 | 42.07 | 21.70 | 21.70 | 8976.7 | 9837.1 | 2.35 | 2.11 | 0.54 | 0.51 | 0.59 | 0.55 | 0.20 | 0.00 | 0.00 | |
| 6596 | 0.12 | 4.94 | 10.92 | 4.94 | 4.94 | 6736.3 | 7322.3 | 1.42 | 1.34 | 0.67 | 0.67 | 0.71 | 0.71 | 0.01 | 0.00 | 0.00 | w=0.969 |
| 6629 | 0.71 | 47.78 | 74.71 | 47.76 | 47.76 | 9978.3 | 10232.0 | 2.19 | 2.14 | 0.63 | 0.58 | 0.64 | 0.58 | 0.63 | 0.00 | 0.00 | w=0.870 |
| 6636 | 0.06 | 2.57 | 5.93 | 2.52 | 2.52 | 6767.6 | 7406.7 | 1.45 | 1.35 | 0.73 | 0.73 | 0.78 | 0.78 | 0.00 | 0.00 | 0.00 | w=0.980 |
| 6710 | 0.31 | 15.35 | 25.59 | 15.73 | 15.73 | 7056.0 | 7479.8 | 1.49 | 1.45 | 0.68 | 0.67 | 0.70 | 0.69 | 0.06 | 0.00 | 0.00 | w=0.904 |
| 6771 | 0.32 | 16.03 | 29.61 | 16.02 | 16.02 | 8621.0 | 9216.4 | 1.93 | 1.84 | 0.69 | 0.68 | 0.71 | 0.69 | 0.10 | 0.00 | 0.00 | w=0.915 |
| 6779 | 0.68 | 27.73 | 73.06 | 27.75 | 27.75 | 10162.6 | 11225.9 | 3.63 | 3.35 | 0.59 | 0.54 | 0.62 | 0.56 | 0.68 | 0.00 | 0.00 | |
| 6850 | 0.03 | 0.00 | 0.00 | 0.00 | 0.00 | 6989.2 | 0.0 | 1.45 | 0.00 | 0.55 | 0.55 | 0.00 | 0.00 | 0.00 | 0.00 | 0.00 | ZAMS |
| 7020 | 0.18 | 6.73 | 13.89 | 6.73 | 6.73 | 7058.3 | 7715.7 | 2.14 | 1.86 | 0.63 | 0.62 | 0.71 | 0.71 | 0.02 | 0.00 | 0.00 | |
| 7056 | 0.13 | 4.90 | 10.88 | 4.90 | 4.90 | 7886.7 | 8769.9 | 2.13 | 1.87 | 0.58 | 0.58 | 0.65 | 0.65 | 0.01 | 0.00 | 0.00 | |
| 7069 | 0.30 | 0.00 | 0.00 | 0.00 | 0.00 | 8617.2 | 0.0 | 1.83 | 0.00 | 0.51 | 0.51 | 0.00 | 0.00 | 0.00 | 0.00 | 0.00 | ZAMS |
| 7141 | 0.60 | 24.72 | 42.76 | 24.74 | 27.50 | 8491.2 | 9070.2 | 2.01 | 1.80 | 0.51 | 0.48 | 0.58 | 0.53 | 0.20 | 0.00 | 0.03 | |
| 7235 | 0.94 | 55.58 | 89.96 | 55.51 | 71.26 | 11607.8 | 11646.6 | 2.59 | 2.46 | 0.96 | 0.76 | 1.07 | 0.79 | 1.00 | 0.00 | 0.44 | |
| 7236 | 0.58 | 47.65 | 50.77 | 48.07 | 48.07 | 12689.0 | 12839.7 | 3.12 | 3.06 | 0.54 | 0.51 | 0.54 | 0.51 | 0.05 | 0.00 | 0.00 | w=0.735 |
| 7266 | 0.48 | 19.10 | 30.46 | 19.10 | 19.10 | 7310.1 | 7850.1 | 1.73 | 1.52 | 0.50 | 0.48 | 0.57 | 0.54 | 0.09 | 0.00 | 0.00 | |
| 7377 | 0.37 | 15.97 | 46.52 | 15.96 | 29.94 | 7412.1 | 7970.2 | 1.61 | 1.52 | 1.10 | 1.08 | 1.17 | 1.14 | 0.29 | 0.00 | 0.12 | w=0.968 |
| 7420 | 0.87 | 45.48 | 90.00 | 45.52 | 73.67 | 9376.7 | 9385.5 | 2.30 | 2.11 | 0.79 | 0.66 | 0.92 | 0.72 | 1.00 | 0.00 | 0.60 | |
| 7460 | 0.37 | 14.94 | 22.48 | 15.28 | 15.28 | 6836.1 | 7430.3 | 1.44 | 1.31 | 0.50 | 0.49 | 0.57 | 0.55 | 0.04 | 0.00 | 0.00 | w=0.999 |
| 7469 | 0.03 | 0.00 | 0.00 | 0.00 | 0.00 | 6988.3 | 0.0 | 1.45 | 0.00 | 0.71 | 0.71 | 0.00 | 0.00 | 0.00 | 0.00 | 0.00 | ZAMS |

Table 4.2—Continued

| HR | $\omega_{90}$ | $i_c$[a] | $i^{th}_{obl.}$ | $i^{th}_{asy.}$ | $i^{th}_{\Delta\phi}$ | $T_{90}$ | $T_c$ | $M_{90}$ | $M_c$ | $\theta^{max}_{90}$ | $\theta^{min}_{90}$ | $\theta^{max}_{c}$ | $\theta^{min}_{c}$ | $P_{obl.}$ | $P_{asy.}$ | $P(\Delta\phi)$ | comments |
|---|---|---|---|---|---|---|---|---|---|---|---|---|---|---|---|---|---|
| 7495 | 0.22 | 8.39 | 17.42 | 8.39 | 8.39 | 6865.9 | 7503.4 | 1.85 | 1.61 | 0.57 | 0.57 | 0.65 | 0.65 | 0.04 | 0.00 | 0.00 | |
| 7528 | 0.68 | 28.24 | 90.00 | 28.24 | 37.97 | 10320.8 | 11388.8 | 3.32 | 3.02 | 0.90 | 0.83 | 0.95 | 0.85 | 1.00 | 0.00 | 0.11 | |
| 7653 | 0.12 | 4.48 | 8.38 | 4.48 | 4.48 | 7840.9 | 8747.9 | 2.36 | 2.07 | 0.52 | 0.52 | 0.57 | 0.57 | 0.01 | 0.00 | 0.00 | |
| 7657 | 0.61 | 25.99 | 44.79 | 26.00 | 33.42 | 7368.1 | 7724.4 | 2.07 | 1.82 | 0.52 | 0.49 | 0.60 | 0.55 | 0.21 | 0.00 | 0.08 | |
| 7740 | 0.93 | 54.78 | 90.00 | 54.82 | 73.51 | 10060.3 | 9923.6 | 2.37 | 2.22 | 0.62 | 0.50 | 0.72 | 0.54 | 1.00 | 0.00 | 0.51 | |
| 7850 | 0.29 | 10.65 | 26.36 | 10.66 | 10.66 | 7906.4 | 8722.3 | 2.07 | 1.83 | 0.63 | 0.63 | 0.71 | 0.70 | 0.09 | 0.00 | 0.00 | |
| 7928 | 0.24 | 9.02 | 20.30 | 9.01 | 9.01 | 7171.4 | 7824.6 | 2.34 | 2.06 | 0.69 | 0.69 | 0.79 | 0.78 | 0.05 | 0.00 | 0.00 | |
| 7950 | 0.48 | 18.19 | 41.47 | 18.19 | 18.19 | 9514.3 | 10749.5 | 3.04 | 2.73 | 0.61 | 0.59 | 0.65 | 0.62 | 0.21 | 0.00 | 0.00 | |
| 7990 | 0.24 | 8.94 | 17.48 | 8.93 | 8.93 | 7244.9 | 7931.0 | 1.96 | 1.71 | 0.59 | 0.59 | 0.67 | 0.67 | 0.03 | 0.00 | 0.00 | |
| 8028 | 0.97 | 65.41 | 90.00 | 65.39 | 76.54 | 11355.5 | 11206.2 | 3.80 | 3.68 | 0.71 | 0.53 | 0.79 | 0.56 | 1.00 | 0.00 | 0.44 | |
| 8097 | 0.04 | 1.31 | 2.01 | 1.31 | 1.31 | 7567.8 | 8429.8 | 1.75 | 1.58 | 0.54 | 0.54 | 0.61 | 0.61 | 0.00 | 0.00 | 0.00 | |
| 8130 | 0.43 | 16.66 | 59.63 | 16.65 | 37.33 | 7054.3 | 7606.6 | 1.68 | 1.48 | 1.05 | 1.02 | 1.20 | 1.16 | 0.47 | 0.00 | 0.18 | |
| 8162 | 0.89 | 49.86 | 90.00 | 87.18 | 87.60 | 9024.4 | 8857.0 | 2.02 | 1.86 | 1.65 | 1.37 | 1.98 | 1.51 | 1.00 | 0.92 | 0.93 | |
| 8344 | 0.31 | 13.91 | 19.46 | 13.92 | 13.92 | 7106.2 | 7639.7 | 1.52 | 1.45 | 0.49 | 0.48 | 0.51 | 0.50 | 0.03 | 0.00 | 0.00 | w=0.955 |
| 8351 | 0.37 | 25.18 | 25.65 | 25.19 | 25.19 | 7147.1 | 7373.6 | 1.49 | 1.47 | 0.54 | 0.53 | 0.55 | 0.53 | 0.00 | 0.00 | 0.00 | w=0.759 |
| 8400 | 0.13 | 4.96 | 10.94 | 4.97 | 4.97 | 6665.7 | 7328.9 | 1.65 | 1.44 | 0.61 | 0.61 | 0.70 | 0.70 | 0.01 | 0.00 | 0.00 | |
| 8430 | 0.03 | 45.50 | 45.50 | 45.50 | 45.50 | 6691.6 | 6692.8 | 1.35 | 1.35 | 1.09 | 1.09 | 1.09 | 1.09 | 0.00 | 0.00 | 0.00 | w=0.042 |
| 8450 | 0.48 | 18.46 | 49.86 | 18.47 | 19.50 | 8995.0 | 9996.1 | 2.16 | 1.96 | 0.73 | 0.71 | 0.80 | 0.76 | 0.32 | 0.00 | 0.01 | |
| 8494 | 0.38 | 14.11 | 37.63 | 14.11 | 14.11 | 7599.8 | 8322.5 | 1.70 | 1.55 | 0.71 | 0.70 | 0.80 | 0.78 | 0.18 | 0.00 | 0.00 | |
| 8559 | 0.38 | 14.48 | 35.32 | 14.47 | 18.21 | 6950.8 | 7495.8 | 2.46 | 2.22 | 0.77 | 0.75 | 0.88 | 0.86 | 0.16 | 0.00 | 0.02 | |
| 8585 | 0.53 | 33.67 | 51.58 | 33.68 | 33.68 | 10005.6 | 10405.0 | 2.27 | 2.20 | 0.58 | 0.56 | 0.59 | 0.56 | 0.26 | 0.00 | 0.00 | w=0.836 |
| 8518 | 0.23 | 8.00 | 16.37 | 8.04 | 8.04 | 10562.3 | 12390.7 | 2.76 | 2.56 | 0.50 | 0.50 | 0.52 | 0.51 | 0.03 | 0.00 | 0.00 | |
| 8613 | 0.43 | 16.79 | 35.66 | 16.79 | 16.79 | 7747.8 | 8415.9 | 2.12 | 1.86 | 0.56 | 0.55 | 0.64 | 0.61 | 0.15 | 0.00 | 0.00 | |
| 8615 | 0.45 | 17.82 | 38.79 | 17.84 | 17.84 | 7039.7 | 7556.4 | 1.99 | 1.74 | 0.57 | 0.55 | 0.65 | 0.62 | 0.18 | 0.00 | 0.00 | |
| 8634 | 0.73 | 31.11 | 74.81 | 31.11 | 31.11 | 12580.2 | 13720.6 | 3.68 | 3.40 | 0.59 | 0.53 | 0.62 | 0.54 | 0.71 | 0.00 | 0.00 | |
| 8781 | 0.67 | 27.09 | 88.03 | 27.08 | 37.65 | 10507.1 | 11675.4 | 3.31 | 3.02 | 1.04 | 0.96 | 1.09 | 0.99 | 0.96 | 0.00 | 0.12 | |
| 8830 | 0.25 | 19.76 | 20.30 | 19.76 | 19.76 | 7519.5 | 7719.7 | 1.59 | 1.58 | 0.61 | 0.61 | 0.61 | 0.61 | 0.00 | 0.00 | 0.00 | w=0.659 |
| 8880 | 0.63 | 26.53 | 49.66 | 26.52 | 32.06 | 8466.3 | 8989.1 | 2.15 | 1.91 | 0.53 | 0.49 | 0.60 | 0.54 | 0.28 | 0.00 | 0.06 | |
| 8984 | 0.26 | 14.08 | 18.13 | 14.08 | 14.08 | 8064.1 | 8520.5 | 1.77 | 1.70 | 0.54 | 0.53 | 0.55 | 0.54 | 0.02 | 0.00 | 0.00 | w=0.870 |
| 9072 | 0.21 | 7.87 | 22.31 | 7.88 | 7.88 | 6755.3 | 7392.5 | 1.92 | 1.67 | 0.96 | 0.95 | 1.10 | 1.09 | 0.07 | 0.00 | 0.00 | |

[a]If inclination is not limited by the ZAMS constraint, this means $i_B$.

Table 4.3. Estimated physical parameters of the preliminary targets for NPOI 100 m baseline

| HR | $\omega_{90}$ | $i_c$ | $i^{th}_{obl.}$ | $i^{th}_{asy.}$ | $i^{th}_{\Delta\phi}$ | $T_{90}$ | $T_c$ | $M_{90}$ | $M_c$ | $\theta^{max}_{90}$ | $\theta^{min}_{90}$ | $\theta^{max}_{c}$ | $\theta^{min}_{c}$ | $P_{obl.}$ | $P_{asy.}$ | $P(\Delta\phi)$ | comments |
|---|---|---|---|---|---|---|---|---|---|---|---|---|---|---|---|---|---|
| 15 | 0.21 | 7.36 | 33.41 | 7.37 | 7.37 | 13006.1 | 14944.9 | 3.70 | 3.37 | 0.94 | 0.93 | 0.98 | 0.97 | 0.16 | 0.00 | 0.00 | |
| 21 | 0.37 | 14.33 | 90.00 | 48.52 | 30.14 | 7208.1 | 7798.4 | 2.05 | 1.79 | 1.92 | 1.88 | 2.19 | 2.13 | 1.00 | 0.33 | 0.12 | |
| 82 | 0.22 | 8.20 | 21.30 | 8.20 | 8.20 | 6768.3 | 7404.2 | 1.81 | 1.58 | 0.56 | 0.55 | 0.64 | 0.63 | 0.06 | 0.00 | 0.00 | |
| 269 | 0.34 | 12.85 | 43.39 | 12.86 | 12.86 | 8357.8 | 9275.4 | 2.26 | 2.00 | 0.68 | 0.67 | 0.75 | 0.73 | 0.25 | 0.00 | 0.00 | |
| 343 | 0.46 | 17.89 | 54.98 | 17.89 | 24.27 | 8276.5 | 8997.2 | 2.07 | 1.84 | 0.58 | 0.56 | 0.65 | 0.62 | 0.40 | 0.00 | 0.05 | |
| 403 | 0.55 | 22.41 | 90.00 | 36.66 | 72.75 | 8494.6 | 9173.1 | 2.52 | 2.23 | 1.22 | 1.16 | 1.36 | 1.27 | 1.00 | 0.18 | 0.68 | |
| 417 | 0.32 | 12.27 | 37.88 | 12.27 | 12.27 | 6849.6 | 7462.2 | 1.53 | 1.36 | 0.65 | 0.64 | 0.75 | 0.73 | 0.19 | 0.00 | 0.00 | |
| 531 | 0.25 | 26.34 | 26.56 | 26.56 | 26.56 | 7322.6 | 7418.3 | 1.53 | 1.54 | 0.61 | 0.60 | 0.61 | 0.60 | 0.00 | 0.00 | 0.00 | w=0.539 |
| 553 | 0.34 | 12.77 | 65.06 | 12.77 | 32.38 | 8473.6 | 9418.4 | 2.04 | 1.84 | 1.17 | 1.15 | 1.29 | 1.26 | 0.57 | 0.00 | 0.16 | |
| 569 | 0.45 | 17.70 | 46.70 | 17.71 | 22.33 | 7624.7 | 8270.6 | 1.83 | 1.63 | 0.55 | 0.53 | 0.62 | 0.59 | 0.28 | 0.00 | 0.04 | |
| 575 | 0.28 | 11.85 | 27.14 | 11.88 | 11.88 | 8298.9 | 9041.1 | 1.87 | 1.75 | 0.50 | 0.50 | 0.53 | 0.52 | 0.09 | 0.00 | 0.00 | w=0.971 |
| 623 | 0.82 | 40.98 | 90.00 | 40.97 | 69.70 | 7878.5 | 7839.3 | 2.60 | 2.37 | 0.60 | 0.52 | 0.72 | 0.57 | 1.00 | 0.00 | 0.54 | |
| 646 | 0.04 | 1.51 | 3.58 | 1.51 | 1.51 | 6719.4 | 7416.7 | 1.44 | 1.31 | 0.54 | 0.54 | 0.61 | 0.61 | 0.00 | 0.00 | 0.00 | |
| 664 | 0.73 | 39.37 | 90.00 | 39.36 | 40.42 | 10221.3 | 10739.3 | 2.30 | 2.21 | 0.55 | 0.50 | 0.56 | 0.50 | 1.00 | 0.00 | 0.02 | w=0.949 |
| 813 | 0.24 | 8.96 | 26.90 | 8.96 | 8.96 | 7381.1 | 8120.8 | 1.67 | 1.51 | 0.71 | 0.71 | 0.80 | 0.79 | 0.10 | 0.00 | 0.00 | |
| 838 | 0.59 | 31.72 | 68.70 | 31.60 | 31.60 | 13199.9 | 13798.9 | 3.41 | 3.19 | 0.48 | 0.45 | 0.49 | 0.46 | 0.58 | 0.00 | 0.00 | w=0.929 |
| 840 | 0.70 | 31.75 | 90.00 | 31.77 | 71.35 | 7640.7 | 7864.0 | 2.04 | 1.81 | 0.81 | 0.74 | 0.95 | 0.82 | 1.00 | 0.00 | 0.63 | |
| 855 | 0.36 | 13.78 | 33.53 | 13.78 | 13.78 | 6863.7 | 7424.0 | 2.10 | 1.83 | 0.52 | 0.51 | 0.60 | 0.58 | 0.14 | 0.00 | 0.00 | |
| 984 | 0.29 | 10.82 | 23.36 | 10.89 | 10.89 | 7858.9 | 8637.5 | 1.77 | 1.62 | 0.49 | 0.49 | 0.54 | 0.54 | 0.07 | 0.00 | 0.00 | w=0.996 |
| 1069 | 0.14 | 5.05 | 12.35 | 5.05 | 5.05 | 6869.6 | 7570.9 | 1.55 | 1.38 | 0.51 | 0.50 | 0.57 | 0.57 | 0.02 | 0.00 | 0.00 | |
| 1251 | 0.29 | 10.40 | 29.06 | 10.40 | 10.40 | 9330.3 | 10646.1 | 2.31 | 2.12 | 0.56 | 0.56 | 0.60 | 0.59 | 0.11 | 0.00 | 0.00 | |
| 1298 | 0.49 | 19.87 | 80.55 | 19.89 | 44.40 | 7356.3 | 7867.0 | 2.08 | 1.82 | 0.85 | 0.81 | 0.97 | 0.92 | 0.83 | 0.00 | 0.27 | |
| 1387 | 0.38 | 14.28 | 40.41 | 14.28 | 14.28 | 8404.0 | 9294.6 | 2.22 | 1.97 | 0.58 | 0.57 | 0.64 | 0.62 | 0.21 | 0.00 | 0.00 | |
| 1392 | 0.85 | 43.94 | 90.00 | 43.95 | 75.25 | 8453.7 | 8380.2 | 2.25 | 2.05 | 0.74 | 0.63 | 0.89 | 0.68 | 1.00 | 0.00 | 0.65 | |
| 1394 | 0.82 | 40.83 | 90.00 | 40.82 | 66.69 | 8424.3 | 8447.8 | 2.16 | 1.95 | 0.65 | 0.57 | 0.77 | 0.61 | 1.00 | 0.00 | 0.49 | |
| 1412 | 0.40 | 15.52 | 57.71 | 15.52 | 24.06 | 7975.2 | 8757.1 | 2.40 | 2.11 | 0.80 | 0.78 | 0.89 | 0.86 | 0.45 | 0.00 | 0.06 | |
| 1412 | 0.48 | 18.68 | 42.65 | 18.70 | 18.70 | 8276.7 | 8975.7 | 1.97 | 1.76 | 0.48 | 0.46 | 0.54 | 0.51 | 0.22 | 0.00 | 0.00 | |
| 1444 | 0.55 | 22.16 | 64.29 | 22.16 | 32.67 | 7853.1 | 8401.0 | 2.01 | 1.78 | 0.57 | 0.54 | 0.65 | 0.60 | 0.54 | 0.00 | 0.11 | |
| 1473 | 0.36 | 13.52 | 35.72 | 13.51 | 13.51 | 8487.8 | 9418.6 | 2.18 | 1.95 | 0.55 | 0.54 | 0.61 | 0.60 | 0.17 | 0.00 | 0.00 | |
| 1560 | 0.77 | 36.10 | 90.00 | 36.10 | 62.63 | 8149.9 | 8289.0 | 2.56 | 2.31 | 0.69 | 0.61 | 0.81 | 0.67 | 1.00 | 0.00 | 0.45 | |
| 1637 | 0.06 | 0.00 | 0.00 | 0.00 | 0.00 | 7274.3 | 0.0 | 1.53 | 0.00 | 0.52 | 0.52 | 0.00 | 0.00 | 0.00 | 0.00 | 0.00 | ZAMS |
| 1641 | 0.39 | 33.26 | 35.39 | 31.73 | 31.73 | 18727.9 | 19042.8 | 5.92 | 5.79 | 0.42 | 0.41 | 0.43 | 0.42 | 0.04 | 0.00 | 0.00 | w=0.658 |
| 1666 | 0.77 | 35.44 | 90.00 | 61.85 | 74.57 | 9000.8 | 9310.5 | 2.39 | 2.15 | 1.19 | 1.06 | 1.36 | 1.14 | 1.00 | 0.46 | 0.69 | |
| 1673 | 0.04 | 2.45 | 4.50 | 2.45 | 2.45 | 6683.2 | 7050.8 | 1.38 | 1.35 | 0.58 | 0.58 | 0.60 | 0.60 | 0.00 | 0.00 | 0.00 | w=0.848 |
| 1676 | 0.34 | 12.78 | 33.30 | 12.78 | 12.78 | 7163.2 | 7775.9 | 2.53 | 2.30 | 0.59 | 0.58 | 0.67 | 0.66 | 0.14 | 0.00 | 0.00 | |
| 1790 | 0.20 | 6.88 | 25.07 | 6.89 | 6.89 | 22346.7 | 25515.3 | 8.78 | 8.27 | 0.72 | 0.71 | 0.75 | 0.75 | 0.09 | 0.00 | 0.00 | |
| 1791 | 0.29 | 10.54 | 52.45 | 10.55 | 10.55 | 14023.5 | 15709.2 | 4.68 | 4.19 | 1.07 | 1.05 | 1.14 | 1.12 | 0.38 | 0.00 | 0.00 | |
| 1998 | 0.70 | 0.00 | 0.00 | 0.00 | 0.00 | 9374.8 | 0.0 | 1.96 | 0.00 | 0.75 | 0.69 | 0.00 | 0.00 | 1.00 | 0.00 | 0.00 | ZAMS |
| 2085 | 0.08 | 10.25 | 10.25 | 10.25 | 10.25 | 7276.4 | 7357.0 | 1.53 | 1.53 | 0.94 | 0.94 | 0.94 | 0.94 | 0.00 | 0.00 | 0.00 | w=0.449 |
| 2095 | 0.23 | 8.17 | 34.61 | 8.19 | 8.19 | 11062.2 | 12904.7 | 3.70 | 3.36 | 0.84 | 0.84 | 0.87 | 0.86 | 0.17 | 0.00 | 0.00 | |
| 2124 | 0.12 | 4.37 | 12.73 | 4.37 | 4.37 | 8064.9 | 8978.1 | 2.23 | 1.96 | 0.63 | 0.62 | 0.70 | 0.70 | 0.02 | 0.00 | 0.00 | |
| 2220 | 0.05 | 0.00 | 0.00 | 0.00 | 0.00 | 6702.8 | 0.0 | 1.37 | 0.00 | 0.56 | 0.56 | 0.00 | 0.00 | 0.00 | 0.00 | 0.00 | ZAMS |
| 2241 | 0.07 | 0.00 | 0.00 | 0.00 | 0.00 | 6803.9 | 0.0 | 1.43 | 0.00 | 0.59 | 0.58 | 0.00 | 0.00 | 0.00 | 0.00 | 0.00 | ZAMS |
| 2264 | 0.08 | 2.87 | 7.63 | 2.87 | 2.87 | 6683.7 | 7340.7 | 1.87 | 1.62 | 0.52 | 0.52 | 0.60 | 0.60 | 0.01 | 0.00 | 0.00 | |
| 2298 | 0.53 | 21.22 | 56.86 | 21.22 | 28.39 | 8343.5 | 8984.5 | 1.98 | 1.77 | 0.56 | 0.53 | 0.63 | 0.59 | 0.42 | 0.00 | 0.06 | |
| 2421 | 0.17 | 5.95 | 29.26 | 5.95 | 5.95 | 9260.7 | 10654.1 | 3.09 | 2.76 | 1.40 | 1.39 | 1.49 | 1.48 | 0.12 | 0.00 | 0.00 | |
| 2484 | 0.35 | 13.43 | 66.37 | 30.19 | 36.66 | 6800.9 | 7389.0 | 1.66 | 1.46 | 1.31 | 1.29 | 1.50 | 1.47 | 0.59 | 0.15 | 0.20 | |
| 2540 | 0.65 | 27.19 | 90.00 | 27.19 | 53.52 | 8775.9 | 9386.6 | 2.84 | 2.54 | 0.79 | 0.73 | 0.88 | 0.79 | 1.00 | 0.00 | 0.34 | |

Table 4.3—Continued

| HR | $\omega_{90}$ | $i_c$ | $i^{th}_{obl.}$ | $i^{th}_{asy.}$ | $i^{th}_{\Delta\phi}$ | $T_{90}$ | $T_c$ | $M_{90}$ | $M_c$ | $\theta^{max}_{90}$ | $\theta^{min}_{90}$ | $\theta^{max}_{c}$ | $\theta^{min}_{c}$ | $P_{obl.}$ | $P_{asy.}$ | $P(\Delta\phi)$ | comments |
|---|---|---|---|---|---|---|---|---|---|---|---|---|---|---|---|---|---|
| 2564 | 0.52 | 25.93 | 63.83 | 25.94 | 34.13 | 7658.3 | 8059.6 | 1.64 | 1.58 | 0.60 | 0.57 | 0.62 | 0.59 | 0.52 | 0.00 | 0.09 | w=0.935 |
| 2763 | 0.62 | 25.47 | 90.00 | 25.47 | 42.78 | 8948.7 | 9660.4 | 2.11 | 1.91 | 0.76 | 0.71 | 0.84 | 0.77 | 1.00 | 0.00 | 0.21 | |
| 2777 | 0.49 | 19.42 | 90.00 | 19.42 | 55.40 | 7400.8 | 7936.4 | 1.66 | 1.48 | 1.06 | 1.02 | 1.21 | 1.15 | 1.00 | 0.00 | 0.42 | |
| 2849 | 0.05 | 0.00 | 0.00 | 0.00 | 0.00 | 6667.7 | 0.0 | 1.41 | 0.00 | 0.53 | 0.53 | 0.00 | 0.00 | 0.00 | 0.00 | 0.00 | ZAMS |
| 2852 | 0.27 | 0.00 | 0.00 | 0.00 | 0.00 | 7393.9 | 0.0 | 1.56 | 0.00 | 0.75 | 0.74 | 0.00 | 0.00 | 0.00 | 0.00 | 0.00 | ZAMS |
| 2890 | 0.10 | 0.00 | 0.00 | 0.00 | 0.00 | 9578.5 | 0.0 | 2.43 | 0.00 | 0.86 | 0.86 | 0.00 | 0.00 | 0.00 | 0.00 | 0.00 | ZAMS |
| 2891 | 0.06 | 2.24 | 11.14 | 2.22 | 2.22 | 9308.0 | 10503.8 | 2.25 | 2.08 | 1.35 | 1.35 | 1.40 | 1.40 | 0.02 | 0.00 | 0.00 | w=0.985 |
| 2927 | 0.12 | 4.36 | 10.38 | 4.36 | 4.36 | 6640.8 | 7266.3 | 2.04 | 1.77 | 0.59 | 0.59 | 0.68 | 0.68 | 0.01 | 0.00 | 0.00 | |
| 2930 | 0.46 | 18.46 | 57.59 | 18.47 | 28.53 | 7013.2 | 7516.1 | 1.92 | 1.68 | 0.62 | 0.60 | 0.72 | 0.69 | 0.44 | 0.00 | 0.08 | |
| 3015 | 0.54 | 22.17 | 54.49 | 22.16 | 32.50 | 7380.9 | 7829.1 | 2.25 | 1.98 | 0.54 | 0.51 | 0.62 | 0.58 | 0.38 | 0.00 | 0.10 | |
| 3314 | 0.47 | 23.84 | 45.44 | 24.06 | 24.06 | 10327.6 | 11038.9 | 2.45 | 2.33 | 0.52 | 0.50 | 0.53 | 0.51 | 0.23 | 0.00 | 0.00 | w=0.916 |
| 3572 | 0.33 | 12.56 | 33.93 | 12.56 | 12.56 | 8262.7 | 9137.5 | 2.32 | 2.05 | 0.58 | 0.57 | 0.65 | 0.63 | 0.15 | 0.00 | 0.00 | |
| 3619 | 0.16 | 6.35 | 17.52 | 6.42 | 6.42 | 7547.1 | 8329.1 | 1.69 | 1.59 | 0.61 | 0.61 | 0.65 | 0.65 | 0.04 | 0.00 | 0.00 | w=0.988 |
| 3624 | 0.09 | 3.33 | 9.42 | 3.33 | 3.33 | 7088.4 | 7808.0 | 1.78 | 1.56 | 0.63 | 0.63 | 0.71 | 0.71 | 0.01 | 0.00 | 0.00 | |
| 3690 | 0.66 | 27.16 | 90.00 | 27.15 | 39.10 | 9454.8 | 10224.4 | 2.29 | 2.09 | 0.64 | 0.59 | 0.70 | 0.63 | 1.00 | 0.00 | 0.13 | |
| 3757 | 0.63 | 26.61 | 90.00 | 26.60 | 75.47 | 7588.3 | 7976.4 | 1.81 | 1.60 | 1.01 | 0.94 | 1.16 | 1.05 | 1.00 | 0.00 | 0.72 | |
| 3888 | 0.55 | 22.39 | 90.00 | 22.38 | 63.41 | 7602.4 | 8103.5 | 2.10 | 1.85 | 0.90 | 0.86 | 1.03 | 0.96 | 1.00 | 0.00 | 0.52 | |
| 3974 | 0.55 | 0.00 | 0.00 | 0.00 | 0.00 | 8496.4 | 0.0 | 1.77 | 0.00 | 0.53 | 0.51 | 0.00 | 0.00 | 0.00 | 0.00 | 0.00 | ZAMS |
| 4033 | 0.22 | 7.96 | 29.01 | 7.97 | 7.97 | 9165.7 | 10450.7 | 2.53 | 2.28 | 0.71 | 0.70 | 0.76 | 0.75 | 0.12 | 0.00 | 0.00 | |
| 4054 | 0.07 | 3.77 | 8.48 | 3.77 | 3.77 | 6638.3 | 7040.5 | 1.37 | 1.33 | 0.69 | 0.69 | 0.71 | 0.71 | 0.01 | 0.00 | 0.00 | w=0.870 |
| 4084 | 0.36 | 0.00 | 0.00 | 0.00 | 0.00 | 7196.7 | 0.0 | 1.72 | 0.00 | 0.49 | 0.48 | 0.00 | 0.00 | 0.00 | 0.00 | 0.00 | ZAMS |
| 4090 | 0.17 | 6.19 | 16.01 | 6.19 | 6.19 | 7518.2 | 8287.2 | 2.23 | 1.95 | 0.54 | 0.54 | 0.61 | 0.61 | 0.03 | 0.00 | 0.00 | |
| 4132 | 0.54 | 24.08 | 58.90 | 24.02 | 31.24 | 8098.2 | 8605.6 | 1.76 | 1.65 | 0.51 | 0.49 | 0.55 | 0.52 | 0.44 | 0.00 | 0.07 | w=0.975 |
| 4141 | 0.34 | 0.00 | 0.00 | 0.00 | 0.00 | 7327.1 | 0.0 | 1.56 | 0.00 | 0.49 | 0.48 | 0.00 | 0.00 | 0.00 | 0.00 | 0.00 | ZAMS |
| 4295 | 0.17 | 5.83 | 27.53 | 5.84 | 5.84 | 9909.3 | 11493.7 | 2.63 | 2.41 | 1.06 | 1.05 | 1.11 | 1.10 | 0.11 | 0.00 | 0.00 | |
| 4310 | 0.11 | 4.13 | 11.51 | 4.13 | 4.13 | 7248.4 | 7997.0 | 1.63 | 1.48 | 0.62 | 0.62 | 0.70 | 0.69 | 0.02 | 0.00 | 0.00 | |
| 4357 | 0.71 | 30.76 | 90.00 | 59.77 | 73.50 | 9060.6 | 9582.7 | 2.10 | 1.90 | 1.26 | 1.14 | 1.41 | 1.23 | 1.00 | 0.46 | 0.67 | |
| 4359 | 0.10 | 3.49 | 12.28 | 3.50 | 3.50 | 9478.7 | 10963.9 | 2.97 | 2.66 | 0.71 | 0.71 | 0.75 | 0.75 | 0.02 | 0.00 | 0.00 | |
| 4399 | 0.10 | 3.79 | 13.90 | 3.79 | 3.79 | 6793.0 | 7481.1 | 1.70 | 1.49 | 0.97 | 0.97 | 1.10 | 1.10 | 0.03 | 0.00 | 0.00 | |
| 4368 | 0.91 | 53.65 | 90.00 | 53.66 | 74.10 | 9093.7 | 8839.9 | 2.45 | 2.30 | 0.67 | 0.54 | 0.81 | 0.60 | 1.00 | 0.00 | 0.55 | |
| 4534 | 0.45 | 0.00 | 0.00 | 0.00 | 0.00 | 9067.3 | 0.0 | 1.93 | 0.00 | 1.37 | 1.32 | 0.00 | 0.00 | 1.00 | 0.00 | 0.00 | ZAMS |
| 4554 | 0.67 | 27.83 | 90.00 | 27.83 | 66.20 | 10129.2 | 11083.3 | 2.64 | 2.42 | 1.12 | 1.03 | 1.20 | 1.07 | 1.00 | 0.00 | 0.55 | |
| 4646 | 0.34 | 15.54 | 31.66 | 15.58 | 15.58 | 7344.3 | 7864.1 | 1.59 | 1.51 | 0.49 | 0.48 | 0.52 | 0.51 | 0.12 | 0.00 | 0.00 | w=0.950 |
| 4660 | 0.67 | 28.10 | 90.00 | 28.10 | 58.73 | 9352.7 | 10068.0 | 2.14 | 1.96 | 0.83 | 0.76 | 0.91 | 0.81 | 1.00 | 0.00 | 0.41 | |
| 4733 | 0.95 | 62.50 | 90.00 | 62.51 | 80.84 | 8948.9 | 8587.6 | 2.62 | 2.49 | 0.61 | 0.48 | 0.75 | 0.54 | 1.00 | 0.00 | 0.66 | |
| 4753 | 0.50 | 20.08 | 46.67 | 20.08 | 24.27 | 6897.7 | 7358.1 | 1.97 | 1.73 | 0.50 | 0.48 | 0.58 | 0.55 | 0.27 | 0.00 | 0.03 | |
| 4825 | 0.11 | 0.00 | 0.00 | 0.00 | 0.00 | 7122.1 | 0.0 | 1.49 | 0.00 | 1.09 | 1.09 | 0.00 | 0.00 | 0.00 | 0.00 | 0.00 | ZAMS |
| 4826 | 0.12 | 0.00 | 0.00 | 0.00 | 0.00 | 7123.6 | 0.0 | 1.50 | 0.00 | 1.08 | 1.08 | 0.00 | 0.00 | 0.00 | 0.00 | 0.00 | ZAMS |
| 4905 | 0.18 | 6.39 | 33.17 | 6.39 | 6.39 | 9706.6 | 11225.2 | 2.93 | 2.64 | 1.43 | 1.42 | 1.50 | 1.49 | 0.16 | 0.00 | 0.00 | |
| 4915 | 0.09 | 0.00 | 0.00 | 0.00 | 0.00 | 13931.3 | 0.0 | 3.61 | 0.00 | 0.60 | 0.60 | 0.00 | 0.00 | 0.00 | 0.00 | 0.00 | ZAMS |
| 4931 | 0.38 | 41.97 | 41.97 | 41.97 | 41.97 | 7221.7 | 7293.0 | 1.50 | 1.50 | 0.57 | 0.56 | 0.57 | 0.56 | 0.00 | 0.00 | 0.00 | w=0.542 |
| 4968 | 0.11 | 0.00 | 0.00 | 0.00 | 0.00 | 6671.4 | 0.0 | 1.40 | 0.00 | 0.56 | 0.56 | 0.00 | 0.00 | 0.00 | 0.00 | 0.00 | ZAMS |
| 5017 | 0.11 | 3.91 | 10.41 | 3.91 | 3.91 | 7179.1 | 7882.0 | 2.50 | 2.24 | 0.59 | 0.59 | 0.67 | 0.67 | 0.01 | 0.00 | 0.00 | |
| 5055 | 0.22 | 27.08 | 27.96 | 27.96 | 27.96 | 8561.9 | 8647.8 | 1.84 | 1.83 | 0.62 | 0.62 | 0.62 | 0.62 | 0.00 | 0.00 | 0.00 | w=0.470 |
| 5062 | 0.76 | 61.09 | 90.00 | 61.07 | 66.19 | 9041.4 | 9120.0 | 1.88 | 1.86 | 0.67 | 0.60 | 0.68 | 0.61 | 1.00 | 0.00 | 0.17 | w=0.831 |
| 5107 | 0.65 | 30.62 | 90.00 | 30.61 | 49.87 | 9089.2 | 9657.0 | 2.01 | 1.88 | 0.83 | 0.77 | 0.88 | 0.80 | 1.00 | 0.00 | 0.27 | w=0.977 |
| 5110 | 0.08 | 3.13 | 7.88 | 3.13 | 3.13 | 6834.0 | 7510.9 | 1.80 | 1.57 | 0.59 | 0.59 | 0.67 | 0.67 | 0.01 | 0.00 | 0.00 | |
| 5127 | 0.85 | 44.12 | 90.00 | 44.15 | 71.25 | 8659.9 | 8607.1 | 2.22 | 2.03 | 0.55 | 0.47 | 0.66 | 0.50 | 1.00 | 0.00 | 0.55 | |

Table 4.3—Continued

| HR | $\omega_{90}$ | $i_c$ | $i^{th}_{obl.}$ | $i^{th}_{asy.}$ | $i^{th}_{\Delta\phi}$ | $T_{90}$ | $T_c$ | $M_{90}$ | $M_c$ | $\theta^{max}_{90}$ | $\theta^{min}_{90}$ | $\theta^{max}_{c}$ | $\theta^{min}_{c}$ | $P_{obl.}$ | $P_{asy.}$ | $P(\Delta\phi)$ | comments |
|---|---|---|---|---|---|---|---|---|---|---|---|---|---|---|---|---|---|
| 5191 | 0.52 | 0.00 | 0.00 | 0.00 | 0.00 | 20287.2 | 0.0 | 5.89 | 0.00 | 0.75 | 0.71 | 0.00 | 0.00 | 1.00 | 0.00 | 0.00 | ZAMS |
| 5264 | 0.69 | 30.26 | 88.91 | 30.23 | 43.31 | 8950.8 | 9495.3 | 2.63 | 2.35 | 0.58 | 0.53 | 0.65 | 0.57 | 0.98 | 0.00 | 0.17 | |
| 5291 | 0.10 | 3.37 | 10.81 | 3.36 | 3.36 | 9947.1 | 11642.2 | 3.61 | 3.27 | 0.58 | 0.58 | 0.60 | 0.60 | 0.02 | 0.00 | 0.00 | |
| 5329 | 0.58 | 23.62 | 86.37 | 23.61 | 39.52 | 8175.0 | 8743.6 | 2.08 | 1.85 | 0.56 | 0.53 | 0.64 | 0.59 | 0.93 | 0.00 | 0.17 | |
| 5351 | 0.41 | 46.03 | 46.89 | 46.89 | 46.89 | 9097.3 | 9176.4 | 1.97 | 1.96 | 0.53 | 0.51 | 0.53 | 0.51 | 0.00 | 0.00 | 0.00 | w=0.553 |
| 5435 | 0.63 | 26.75 | 90.00 | 26.77 | 73.37 | 8299.2 | 8805.3 | 2.18 | 1.94 | 1.13 | 1.05 | 1.28 | 1.15 | 1.00 | 0.00 | 0.68 | |
| 5447 | 0.05 | 0.00 | 0.00 | 0.00 | 0.00 | 7150.2 | 0.0 | 1.74 | 0.00 | 0.69 | 0.69 | 0.00 | 0.00 | 0.00 | 0.00 | 0.00 | ZAMS |
| 5487 | 0.25 | 9.18 | 31.91 | 9.18 | 13.44 | 7016.6 | 7688.1 | 1.55 | 1.40 | 0.95 | 0.94 | 1.08 | 1.06 | 0.14 | 0.00 | 0.02 | |
| 5511 | 0.97 | 64.24 | 90.00 | 64.15 | 72.98 | 12540.1 | 12499.1 | 2.84 | 2.75 | 0.69 | 0.52 | 0.75 | 0.54 | 1.00 | 0.00 | 0.33 | |
| 5570 | 0.51 | 19.97 | 68.53 | 19.97 | 34.42 | 7528.0 | 8071.8 | 1.67 | 1.50 | 0.66 | 0.64 | 0.75 | 0.71 | 0.62 | 0.00 | 0.14 | |
| 5634 | 0.18 | 0.00 | 0.00 | 0.00 | 0.00 | 6768.3 | 0.0 | 1.38 | 0.00 | 0.63 | 0.62 | 0.00 | 0.00 | 0.00 | 0.00 | 0.00 | ZAMS |
| 5685 | 0.80 | 36.50 | 90.00 | 36.46 | 46.29 | 14082.6 | 14855.1 | 4.15 | 3.81 | 0.79 | 0.70 | 0.85 | 0.71 | 1.00 | 0.00 | 0.15 | |
| 5723 | 0.05 | 1.85 | 5.29 | 1.85 | 1.85 | 6660.8 | 7333.0 | 1.57 | 1.38 | 0.64 | 0.64 | 0.73 | 0.73 | 0.00 | 0.00 | 0.00 | |
| 5733 | 0.41 | 16.08 | 57.85 | 16.08 | 28.40 | 7406.3 | 8024.1 | 1.92 | 1.69 | 0.72 | 0.70 | 0.81 | 0.78 | 0.45 | 0.00 | 0.10 | |
| 5789 | 0.49 | 19.27 | 88.80 | 19.27 | 41.09 | 7557.2 | 8092.4 | 2.66 | 2.41 | 0.88 | 0.85 | 1.01 | 0.96 | 0.98 | 0.00 | 0.23 | |
| 5793 | 0.54 | 20.44 | 90.00 | 20.46 | 44.81 | 10218.1 | 11563.7 | 2.66 | 2.46 | 1.16 | 1.10 | 1.21 | 1.14 | 1.00 | 0.00 | 0.27 | |
| 5867 | 0.73 | 32.01 | 90.00 | 31.99 | 48.45 | 9449.6 | 10041.7 | 2.58 | 2.33 | 0.71 | 0.65 | 0.79 | 0.68 | 1.00 | 0.00 | 0.24 | |
| 5881 | 0.37 | 13.30 | 39.86 | 13.29 | 13.29 | 10345.1 | 11931.6 | 2.85 | 2.62 | 0.61 | 0.59 | 0.63 | 0.61 | 0.21 | 0.00 | 0.00 | |
| 5892 | 0.15 | 12.56 | 16.74 | 12.50 | 12.50 | 8373.6 | 8585.5 | 1.81 | 1.79 | 0.71 | 0.71 | 0.72 | 0.71 | 0.02 | 0.00 | 0.00 | w=0.624 |
| 6093 | 0.34 | 18.37 | 32.73 | 18.37 | 18.37 | 7296.7 | 7672.2 | 1.55 | 1.51 | 0.58 | 0.57 | 0.59 | 0.58 | 0.11 | 0.00 | 0.00 | w=0.879 |
| 6095 | 0.76 | 35.57 | 90.00 | 35.56 | 74.12 | 7989.0 | 8120.7 | 2.67 | 2.42 | 0.95 | 0.85 | 1.12 | 0.94 | 1.00 | 0.00 | 0.67 | |
| 6116 | 0.34 | 12.62 | 35.80 | 12.62 | 12.62 | 7118.6 | 7769.9 | 1.55 | 1.42 | 0.57 | 0.56 | 0.65 | 0.64 | 0.17 | 0.00 | 0.00 | |
| 6129 | 0.19 | 7.62 | 15.49 | 7.43 | 7.43 | 8185.8 | 8996.8 | 1.87 | 1.73 | 0.49 | 0.48 | 0.52 | 0.51 | 0.03 | 0.00 | 0.00 | w=0.979 |
| 6237 | 0.24 | 10.47 | 25.69 | 10.47 | 10.47 | 7015.0 | 7557.9 | 1.51 | 1.43 | 0.61 | 0.60 | 0.64 | 0.63 | 0.08 | 0.00 | 0.00 | w=0.952 |
| 6324 | 0.33 | 12.02 | 34.86 | 12.01 | 12.01 | 9819.2 | 11260.0 | 2.61 | 2.39 | 0.53 | 0.52 | 0.56 | 0.55 | 0.16 | 0.00 | 0.00 | |
| 6410 | 0.93 | 53.89 | 90.00 | 53.85 | 79.93 | 10485.7 | 10367.2 | 2.31 | 2.16 | 0.99 | 0.80 | 1.15 | 0.86 | 1.00 | 0.00 | 0.70 | |
| 6554 | 0.27 | 23.43 | 24.57 | 23.66 | 23.66 | 7718.7 | 7881.1 | 1.64 | 1.63 | 0.49 | 0.49 | 0.50 | 0.49 | 0.01 | 0.00 | 0.00 | w=0.627 |
| 6555 | 0.21 | 13.02 | 19.63 | 13.02 | 13.02 | 7540.5 | 7902.0 | 1.62 | 1.59 | 0.51 | 0.51 | 0.52 | 0.51 | 0.03 | 0.00 | 0.00 | w=0.795 |
| 6556 | 0.82 | 40.83 | 90.00 | 81.55 | 83.08 | 9186.9 | 9306.4 | 2.12 | 1.93 | 1.70 | 1.47 | 1.97 | 1.56 | 1.00 | 0.81 | 0.84 | |
| 6581 | 0.55 | 21.70 | 56.39 | 21.71 | 23.71 | 8970.9 | 9850.7 | 2.35 | 2.11 | 0.54 | 0.51 | 0.59 | 0.55 | 0.41 | 0.00 | 0.02 | |
| 6596 | 0.12 | 5.03 | 13.66 | 5.03 | 5.03 | 6733.2 | 7307.5 | 1.42 | 1.34 | 0.67 | 0.67 | 0.71 | 0.71 | 0.02 | 0.00 | 0.00 | w=0.963 |
| 6629 | 0.71 | 47.77 | 90.00 | 47.68 | 48.07 | 9982.2 | 10235.8 | 2.19 | 2.14 | 0.63 | 0.58 | 0.64 | 0.58 | 1.00 | 0.00 | 0.01 | w=0.870 |
| 6636 | 0.06 | 2.57 | 7.35 | 2.57 | 2.57 | 6766.9 | 7411.6 | 1.45 | 1.35 | 0.73 | 0.73 | 0.78 | 0.78 | 0.01 | 0.00 | 0.00 | w=0.980 |
| 6710 | 0.31 | 15.36 | 32.40 | 15.52 | 15.52 | 7052.8 | 7476.1 | 1.49 | 1.45 | 0.68 | 0.67 | 0.70 | 0.69 | 0.12 | 0.00 | 0.00 | w=0.904 |
| 6771 | 0.32 | 16.02 | 38.19 | 16.04 | 16.04 | 8624.9 | 9218.8 | 1.93 | 1.84 | 0.69 | 0.68 | 0.71 | 0.69 | 0.18 | 0.00 | 0.00 | w=0.915 |
| 6779 | 0.68 | 27.78 | 90.00 | 27.75 | 29.86 | 10169.3 | 11197.3 | 3.63 | 3.34 | 0.59 | 0.54 | 0.62 | 0.56 | 1.00 | 0.00 | 0.02 | |
| 6850 | 0.03 | 0.00 | 0.00 | 0.00 | 0.00 | 6989.2 | 0.0 | 1.45 | 0.00 | 0.55 | 0.55 | 0.00 | 0.00 | 0.00 | 0.00 | 0.00 | ZAMS |
| 7020 | 0.18 | 6.73 | 17.14 | 6.73 | 6.73 | 7063.1 | 7714.2 | 2.14 | 1.86 | 0.62 | 0.62 | 0.72 | 0.71 | 0.04 | 0.00 | 0.00 | |
| 7056 | 0.13 | 4.90 | 13.54 | 4.90 | 4.90 | 7894.3 | 8774.0 | 2.13 | 1.87 | 0.58 | 0.58 | 0.65 | 0.65 | 0.02 | 0.00 | 0.00 | |
| 7069 | 0.30 | 0.00 | 0.00 | 0.00 | 0.00 | 8617.2 | 0.0 | 1.83 | 0.00 | 0.51 | 0.51 | 0.00 | 0.00 | 0.00 | 0.00 | 0.00 | ZAMS |
| 7141 | 0.60 | 24.75 | 62.98 | 24.73 | 32.89 | 8498.9 | 9062.0 | 2.01 | 1.80 | 0.51 | 0.48 | 0.58 | 0.53 | 0.51 | 0.00 | 0.09 | |
| 7235 | 0.94 | 55.35 | 90.00 | 55.47 | 75.51 | 11594.5 | 11642.9 | 2.59 | 2.46 | 0.96 | 0.76 | 1.07 | 0.79 | 1.00 | 0.00 | 0.56 | |
| 7236 | 0.57 | 49.88 | 67.35 | 48.79 | 48.79 | 12716.2 | 12866.0 | 3.12 | 3.08 | 0.54 | 0.51 | 0.54 | 0.51 | 0.43 | 0.00 | 0.00 | w=0.714 |
| 7266 | 0.48 | 19.09 | 42.18 | 19.10 | 23.25 | 7311.5 | 7851.6 | 1.73 | 1.52 | 0.50 | 0.48 | 0.57 | 0.54 | 0.22 | 0.00 | 0.03 | |
| 7377 | 0.37 | 15.96 | 63.30 | 15.97 | 42.33 | 7413.4 | 7971.2 | 1.61 | 1.52 | 1.10 | 1.08 | 1.17 | 1.14 | 0.54 | 0.00 | 0.27 | w=0.968 |
| 7420 | 0.87 | 45.50 | 90.00 | 45.52 | 78.07 | 9379.2 | 9383.2 | 2.30 | 2.11 | 0.79 | 0.66 | 0.92 | 0.72 | 1.00 | 0.00 | 0.71 | |
| 7460 | 0.37 | 14.64 | 29.52 | 14.72 | 14.72 | 6836.3 | 7400.4 | 1.44 | 1.33 | 0.50 | 0.49 | 0.55 | 0.53 | 0.10 | 0.00 | 0.00 | w=0.990 |
| 7469 | 0.03 | 0.00 | 0.00 | 0.00 | 0.00 | 6988.3 | 0.0 | 1.45 | 0.00 | 0.71 | 0.71 | 0.00 | 0.00 | 0.00 | 0.00 | 0.00 | ZAMS |

Table 4.3—Continued

| HR | $\omega_{90}$ | $i_c$ | $i^{th}_{obl.}$ | $i^{th}_{asy.}$ | $i^{th}_{\Delta\phi}$ | $T_{90}$ | $T_c$ | $M_{90}$ | $M_c$ | $\theta^{max}_{90}$ | $\theta^{min}_{90}$ | $\theta^{max}_{c}$ | $\theta^{min}_{c}$ | $P_{obl.}$ | $P_{asy.}$ | $P(\Delta\phi)$ | comments |
|---|---|---|---|---|---|---|---|---|---|---|---|---|---|---|---|---|---|
| 7495 | 0.22 | 8.38 | 22.52 | 8.39 | 8.39 | 6862.5 | 7506.5 | 1.85 | 1.61 | 0.57 | 0.57 | 0.65 | 0.65 | 0.07 | 0.00 | 0.00 | |
| 7528 | 0.68 | 28.23 | 90.00 | 28.24 | 49.15 | 10325.6 | 11393.4 | 3.32 | 3.02 | 0.90 | 0.83 | 0.95 | 0.85 | 1.00 | 0.00 | 0.26 | |
| 7653 | 0.12 | 4.47 | 11.83 | 4.48 | 4.48 | 7842.0 | 8754.2 | 2.36 | 2.07 | 0.52 | 0.52 | 0.57 | 0.57 | 0.02 | 0.00 | 0.00 | |
| 7657 | 0.61 | 26.00 | 77.96 | 26.01 | 40.63 | 7364.3 | 7721.9 | 2.07 | 1.82 | 0.52 | 0.49 | 0.60 | 0.55 | 0.77 | 0.00 | 0.17 | |
| 7740 | 0.93 | 54.85 | 90.00 | 54.83 | 77.09 | 10074.8 | 9917.0 | 2.37 | 2.22 | 0.62 | 0.50 | 0.73 | 0.54 | 1.00 | 0.00 | 0.61 | |
| 7850 | 0.28 | 10.65 | 33.38 | 10.66 | 10.66 | 7901.2 | 8720.9 | 2.07 | 1.83 | 0.63 | 0.63 | 0.71 | 0.70 | 0.15 | 0.00 | 0.00 | |
| 7928 | 0.24 | 9.01 | 25.88 | 9.01 | 9.01 | 7174.0 | 7833.4 | 2.34 | 2.06 | 0.69 | 0.69 | 0.79 | 0.78 | 0.09 | 0.00 | 0.00 | |
| 7950 | 0.48 | 18.19 | 54.19 | 18.19 | 18.19 | 9523.6 | 10751.6 | 3.04 | 2.73 | 0.61 | 0.59 | 0.65 | 0.62 | 0.39 | 0.00 | 0.00 | |
| 7990 | 0.24 | 8.94 | 21.81 | 8.93 | 8.93 | 7244.9 | 7931.1 | 1.96 | 1.71 | 0.59 | 0.59 | 0.67 | 0.67 | 0.06 | 0.00 | 0.00 | |
| 8028 | 0.97 | 65.41 | 90.00 | 65.40 | 79.62 | 11351.1 | 11205.0 | 3.80 | 3.68 | 0.71 | 0.53 | 0.79 | 0.56 | 1.00 | 0.00 | 0.57 | |
| 8097 | 0.04 | 1.31 | 3.39 | 1.31 | 1.31 | 7567.8 | 8429.8 | 1.75 | 1.58 | 0.54 | 0.54 | 0.61 | 0.61 | 0.00 | 0.00 | 0.00 | |
| 8130 | 0.43 | 16.65 | 90.00 | 16.65 | 50.36 | 7055.9 | 7608.3 | 1.68 | 1.48 | 1.05 | 1.02 | 1.20 | 1.16 | 1.00 | 0.00 | 0.34 | |
| 8162 | 0.89 | 49.91 | 90.00 | 86.97 | 85.82 | 9029.7 | 8852.2 | 2.02 | 1.86 | 1.65 | 1.36 | 1.98 | 1.51 | 1.00 | 0.92 | 0.89 | |
| 8344 | 0.31 | 13.91 | 26.01 | 13.92 | 13.92 | 7106.5 | 7640.0 | 1.52 | 1.45 | 0.49 | 0.48 | 0.51 | 0.50 | 0.07 | 0.00 | 0.00 | w=0.955 |
| 8351 | 0.37 | 25.22 | 32.20 | 25.20 | 25.20 | 7157.5 | 7381.0 | 1.49 | 1.48 | 0.54 | 0.53 | 0.54 | 0.53 | 0.07 | 0.00 | 0.00 | w=0.759 |
| 8400 | 0.13 | 4.97 | 13.60 | 4.96 | 4.96 | 6663.8 | 7323.2 | 1.65 | 1.44 | 0.61 | 0.61 | 0.70 | 0.70 | 0.02 | 0.00 | 0.00 | |
| 8430 | 0.03 | 12.13 | 15.84 | 15.84 | 15.84 | 6688.3 | 6699.8 | 1.35 | 1.35 | 1.09 | 1.09 | 1.09 | 1.09 | 0.00 | 0.00 | 0.00 | w=0.141 |
| 8450 | 0.48 | 18.47 | 73.00 | 18.47 | 24.53 | 8997.8 | 9993.1 | 2.16 | 1.96 | 0.73 | 0.71 | 0.80 | 0.76 | 0.70 | 0.00 | 0.05 | |
| 8494 | 0.38 | 14.12 | 50.77 | 14.12 | 25.68 | 7595.2 | 8316.9 | 1.70 | 1.55 | 0.71 | 0.70 | 0.80 | 0.78 | 0.35 | 0.00 | 0.08 | |
| 8518 | 0.23 | 8.12 | 20.88 | 8.08 | 8.08 | 10569.1 | 12452.5 | 2.76 | 2.57 | 0.50 | 0.50 | 0.52 | 0.51 | 0.06 | 0.00 | 0.00 | w=0.999 |
| 8559 | 0.38 | 14.47 | 46.63 | 14.48 | 24.11 | 6952.2 | 7497.4 | 2.46 | 2.22 | 0.77 | 0.75 | 0.88 | 0.86 | 0.29 | 0.00 | 0.07 | |
| 8585 | 0.53 | 34.23 | 79.50 | 34.10 | 34.10 | 10004.3 | 10397.6 | 2.27 | 2.21 | 0.58 | 0.56 | 0.58 | 0.56 | 0.78 | 0.00 | 0.00 | w=0.828 |
| 8613 | 0.43 | 16.79 | 48.44 | 16.79 | 21.13 | 7749.0 | 8417.3 | 2.12 | 1.86 | 0.56 | 0.55 | 0.64 | 0.61 | 0.31 | 0.00 | 0.03 | |
| 8615 | 0.45 | 17.82 | 50.81 | 17.83 | 29.10 | 7044.6 | 7555.2 | 1.99 | 1.74 | 0.57 | 0.55 | 0.65 | 0.62 | 0.34 | 0.00 | 0.09 | |
| 8634 | 0.73 | 31.05 | 90.00 | 31.11 | 31.11 | 12607.7 | 13747.5 | 3.69 | 3.41 | 0.59 | 0.53 | 0.62 | 0.54 | 1.00 | 0.00 | 0.00 | |
| 8781 | 0.67 | 27.11 | 90.00 | 27.08 | 48.71 | 10526.2 | 11663.6 | 3.32 | 3.02 | 1.04 | 0.96 | 1.10 | 0.99 | 1.00 | 0.00 | 0.29 | |
| 8830 | 0.25 | 19.79 | 26.34 | 19.76 | 19.76 | 7515.4 | 7718.1 | 1.59 | 1.58 | 0.61 | 0.61 | 0.61 | 0.61 | 0.05 | 0.00 | 0.00 | w=0.659 |
| 8880 | 0.63 | 26.52 | 82.48 | 26.52 | 37.93 | 8469.3 | 8992.6 | 2.15 | 1.91 | 0.53 | 0.49 | 0.60 | 0.54 | 0.86 | 0.00 | 0.13 | |
| 8984 | 0.26 | 13.75 | 23.49 | 13.76 | 13.76 | 8060.5 | 8530.5 | 1.77 | 1.70 | 0.54 | 0.53 | 0.55 | 0.55 | 0.06 | 0.00 | 0.00 | w=0.881 |
| 9072 | 0.21 | 7.88 | 27.77 | 7.88 | 9.54 | 6757.9 | 7385.0 | 1.92 | 1.67 | 0.96 | 0.95 | 1.10 | 1.09 | 0.11 | 0.00 | 0.01 | |

Table 4.4. Target list for oblateness with at least 25% detection probability

| HR | Name | $\alpha$ | $\delta$ 2000 | SpType | V | B-V | $v \sin i$ | $\pi$ | $P_{obl.}^{80m}$ | $P_{obl.}^{100m}$ |
|---|---|---|---|---|---|---|---|---|---|---|
| 21 | 11Bet Cas | 000910.7 | +590859 | F2III-IV | 2.27 | 0.34 | 70 | 59.89 | 0.68 | 1.00 |
| 403 | 37Del Cas | 012549.0 | +601407 | A5III-IV v | 2.68 | 0.13 | 113 | 32.81 | 1.00 | 1.00 |
| 553 | 6Bet Ari | 015438.4 | +204829 | A5V | 2.64 | 0.13 | 79 | 54.74 | 0.30 | 0.57 |
| 623 | 14 Ari | 020925.3 | +255623 | F2III | 4.98 | 0.33 | 154 | 10.19 | 1.00 | 1.00 |
| 664 | 9Gam Tri | 021718.9 | +335050 | A1Vnn | 4.01 | 0.02 | 208 | 27.73 | 0.71 | 1.00 |
| 838 | 41 Ari | 024959.0 | +271538 | B8Vn | 3.63 | -0.10 | 180 | 20.45 | 0.19 | 0.58 |
| 840 | 16 Per | 025035.1 | +381907 | F2III | 4.23 | 0.34 | 149 | 25.54 | 1.00 | 1.00 |
| 1298 | 38Omi1Eri | 041151.9 | -065015 | F2II-III | 4.04 | 0.33 | 96 | 25.98 | 0.46 | 0.83 |
| 1392 | 69Ups Tau | 042618.5 | +224849 | A8Vn | 4.28 | 0.26 | 196 | 21.07 | 1.00 | 1.00 |
| 1394 | 71 Tau | 042620.8 | +153706 | F0V | 4.49 | 0.25 | 192 | 20.86 | 1.00 | 1.00 |
| 1412 | 78The2Tau | 042839.7 | +155215 | A7III | 3.73 | +0.18 | 78 | 21.89 | 0.23 | 0.45 |
| 1444 | 86Rho Tau | 043350.9 | +145040 | A8V | 4.65 | 0.25 | 117 | 21.39 | 0.21 | 0.54 |
| 1560 | 61Ome Eri | 045253.7 | -052710 | F4III+A6III | 4.39 | 0.25 | 153 | 14.39 | 0.89 | 1.00 |
| 1666 | 67Bet Eri | 050751.0 | -050511 | A3III | 2.79 | 0.13 | 179 | 36.71 | 1.00 | 1.00 |
| 1791 | 112Bet Tau | 052617.5 | +283627 | B7III | 1.65 | -0.13 | 71 | 24.89 | 0.22 | 0.38 |
| 1998 | 14Zet Lep | 054657.3 | -144919 | A3Vn | 3.55 | 0.10 | 202 | 46.47 | 0.67 | 1.00 |
| 2298 | 8Eps Mon | 062346.1 | +043534 | A5IV | 4.44 | 0.18 | 124 | 25.39 | 0.19 | 0.42 |
| 2484 | 31Xi Gem | 064517.4 | +125344 | F5III | 3.36 | 0.43 | 70 | 57.02 | 0.32 | 0.59 |
| 2540 | 34The Gem | 065247.3 | +335740 | A3III | 3.60 | 0.10 | 128 | 16.59 | 0.92 | 1.00 |
| 2564 | 38 Gem | 065438.7 | +131040 | F0Vp | 4.65 | 0.30 | 126 | 35.79 | 0.17 | 0.52 |
| 2763 | 54Lam Gem | 071805.6 | +163225 | A3V | 3.58 | 0.11 | 154 | 34.59 | 0.77 | 1.00 |
| 2777 | 55Del Gem | 072007.4 | +215856 | F2IV | 3.53 | 0.34 | 111 | 55.45 | 0.77 | 1.00 |
| 2930 | 71Omi Gem | 073909.9 | +343503 | F3III | 4.90 | 0.40 | 89 | 20.62 | 0.20 | 0.44 |
| 3015 | 4 Pup | 074556.9 | -143350 | F0V | 5.04 | 0.33 | 101 | 13.80 | 0.15 | 0.38 |
| 3690 | 38 Lyn | 091850.7 | +364809 | A3V | 3.82 | 0.06 | 165 | 26.75 | 0.78 | 1.00 |
| 3757 | 23 UMa | 093131.7 | +630343 | F0IV | 3.67 | 0.33 | 140 | 43.20 | 1.00 | 1.00 |
| 3888 | 29Ups UMa | 095059.4 | +590219 | F2IV | 3.80 | 0.29 | 110 | 28.35 | 0.98 | 1.00 |
| 4132 |  | 103313.9 | +402532 | A7IV | 4.75 | 0.23 | 132 | 29.13 | 0.17 | 0.44 |
| 4357 | 68Del Leo | 111406.5 | +203125 | A4V | 2.56 | 0.12 | 181 | 56.52 | 1.00 | 1.00 |
| 4399 | 78Iot Leo | 112355.5 | +103145 | F4IV | 3.94 | 0.41 | 20 | 41.26 | 0.99 | 0.03 |
| 4368 | 74Phi Leo | 111639.7 | -033906 | A7IVn | 4.47 | 0.21 | 225 | 16.69 | 0.02 | 1.00 |
| 4534 | 94Bet Leo | 114903.6 | +143419 | A3V | 2.14 | 0.09 | 121 | 90.16 | 0.42 | 1.00 |
| 4554 | 64Gam UMa | 115349.8 | +534141 | A0Ve | 2.44 | 0.00 | 168 | 38.99 | 1.00 | 1.00 |
| 4660 | 69Del UMa | 121525.6 | +570157 | A3V | 3.31 | 0.08 | 177 | 40.05 | 1.00 | 1.00 |

Table 4.4—Continued

| HR | Name | $\alpha$ | $\delta$ 2000 | SpType | V | B-V | $v \sin i$ | $\pi$ | $P_{obl.}^{80m}$ | $P_{obl.}^{100m}$ |
|---|---|---|---|---|---|---|---|---|---|---|
| 4733 | 14 Com | 122624.1 | +271606 | F0p | 4.95 | 0.27 | 227 | 11.92 | 0.99 | 1.00 |
| 5062 | 80 UMa | 132513.5 | +545917 | A5V | 4.01 | 0.16 | 218 | 40.19 | 1.00 | 1.00 |
| 5107 | 79Zet Vir | 133441.6 | -003545 | A3V | 3.37 | 0.11 | 173 | 44.55 | 0.81 | 1.00 |
| 5127 | 25 CVn | 133727.6 | +361742 | A7III | 4.82 | 0.23 | 204 | 17.01 | 1.00 | 1.00 |
| 5191 | 85Eta UMa | 134732.4 | +491848 | B3V | 1.86 | -0.19 | 205 | 32.39 | 0.33 | 1.00 |
| 5264 | 93Tau Vir | 140138.8 | +013240 | A3V | 4.26 | 0.10 | 150 | 14.94 | 0.57 | 0.98 |
| 5329 | 17Kap2Boo | 141329.0 | +514725 | A8IV | 4.54 | 0.20 | 127 | 21.03 | 0.34 | 0.93 |
| 5435 | 27Gam Boo | 143204.7 | +381830 | A7III | 3.03 | 0.19 | 139 | 38.29 | 1.00 | 1.00 |
| 5511 | 109 Vir | 144614.9 | +015334 | A0V | 3.72 | -0.01 | 351 | 25.35 | 0.99 | 1.00 |
| 5570 | 16 Lib | 145711.0 | -042047 | F0V | 4.49 | 0.32 | 117 | 35.83 | 0.25 | 0.62 |
| 5685 | 27Bet Lib | 151700.4 | -092259 | B8V | 2.61 | -0.11 | 230 | 20.38 | 0.91 | 1.00 |
| 5733 | 51Mu 1Boo | 152429.4 | +372238 | F2IVa | 4.31 | 0.31 | 84 | 26.96 | 0.21 | 0.45 |
| 5789 | 13Del Ser | 153448.1 | +103221 | F0IV | 3.80 | 0.26 | 80 | 15.00 | 0.48 | 0.98 |
| 5793 | 5Alp CrB | 153441.3 | +264253 | A0V+G5V | 2.23 | -0.02 | 133 | 43.65 | 0.90 | 1.00 |
| 5867 | 28Bet Ser | 154611.3 | +152519 | A2IV | 3.67 | 0.06 | 170 | 21.31 | 0.87 | 1.00 |
| 6095 | 20Gam Her | 162155.2 | +190911 | A9III | 3.75 | 0.27 | 141 | 16.69 | 1.00 | 1.00 |
| 6410 | 65Del Her | 171501.9 | +245021 | A3IV | 3.14 | 0.08 | 290 | 41.55 | 1.00 | 1.00 |
| 6556 | 55Alp Oph | 173456.1 | +123336 | A5III | 2.08 | 0.15 | 219 | 69.84 | 1.00 | 1.00 |
| 6581 | 56Omi Ser | 174124.9 | -125231 | A2V | 4.26 | 0.08 | 125 | 19.41 | 0.20 | 0.41 |
| 6629 | 62Gam Oph | 174753.6 | +024226 | A0Vnp | 3.75 | 0.04 | 205 | 34.42 | 0.63 | 1.00 |
| 6779 | 103Omi Her | 180732.6 | +284545 | B9.5V e | 3.83 | -0.03 | 134 | 9.39 | 0.68 | 1.00 |
| 7141 | 63The1Ser | 185613.2 | +041213 | A5V | 4.62 | 0.17 | 143 | 22.84 | 0.20 | 0.51 |
| 7235 | 17Zet Aql | 190524.6 | +135148 | A0Vn | 2.99 | 0.01 | 317 | 39.18 | 1.00 | 1.00 |
| 7236 | 16Lam Aql | 190614.9 | -045257 | B9Vn | 3.44 | -0.09 | 176 | 26.05 | 0.05 | 0.43 |
| 7377 | 30Del Aql | 192529.9 | +030653 | F3IV | 3.36 | 0.32 | 85 | 65.05 | 0.29 | 0.54 |
| 7420 | 10Iot2Cyg | 192942.3 | +514347 | A5Vn | 3.79 | 0.14 | 226 | 26.63 | 1.00 | 1.00 |
| 7528 | 18Del Cyg | 194458.5 | +450751 | B9.5IV+F1V | 2.87 | -0.03 | 149 | 19.07 | 1.00 | 1.00 |
| 7657 | 16 Vul | 200201.4 | +245617 | F2III | 5.22 | 0.36 | 121 | 15.43 | 0.21 | 0.77 |
| 7740 | 33 Cyg | 201323.9 | +563404 | A3IV-Vn | 4.30 | 0.11 | 268 | 21.41 | 1.00 | 1.00 |
| 7950 | 2Eps Aqr | 204740.6 | -092945 | A1V | 3.77 | 0.00 | 98 | 14.21 | 0.21 | 0.39 |
| 8028 | 58Nu Cyg | 205710.4 | +411002 | A1Vn | 3.94 | 0.02 | 241 | 9.17 | 1.00 | 1.00 |
| 8130 | 65Tau Cyg | 211447.5 | +380244 | F2IV | 3.72 | 0.39 | 89 | 47.80 | 0.47 | 1.00 |
| 8162 | 5Alp Cep | 211834.8 | +623508 | A7V | 2.44 | 0.22 | 246 | 66.84 | 1.00 | 1.00 |
| 8450 | 26The Peg | 221012.0 | +061152 | A2Vp | 3.53 | 0.08 | 117 | 33.77 | 0.32 | 0.70 |

Table 4.4—Continued

| HR | Name | $\alpha$ | $\delta$ 2000 | SpType | V | B-V | $v \sin i$ | $\pi$ | $P_{obl.}^{80m}$ | $P_{obl.}^{100m}$ |
|---|---|---|---|---|---|---|---|---|---|---|
| 8494 | 23Eps Cep | 221502.0 | +570237 | F0IV | 4.19 | 0.28 | 86 | 38.86 | 0.18 | 0.35 |
| 8559 | 55Zet2Aqr | 222850.1 | -000112 | F3V | 4.42 | 0.38 | 58 | 13.00 | 0.26 | 0.29 |
| 8585 | 7Alp Lac | 223117.5 | +501657 | A1V | 3.77 | 0.01 | 146 | 31.86 | 0.03 | 0.78 |
| 8613 | 9 Lac | 223722.4 | +513243 | A8IV | 4.63 | 0.24 | 87 | 18.95 | 0.15 | 0.31 |
| 8615 | 31 Cep | 223546.1 | +733835 | F3III-IV | 5.08 | 0.39 | 85 | 17.70 | 0.18 | 0.34 |
| 8634 | 42Zet Peg | 224127.7 | +104953 | B8V | 3.40 | -0.09 | 194 | 15.64 | 0.71 | 1.00 |
| 8781 | 54Alp Peg | 230445.7 | +151219 | B9V | 2.49 | -0.04 | 148 | 23.36 | 0.96 | 1.00 |
| 8880 | 62Tau Peg | 232038.2 | +234425 | A5Vp | 4.60 | 0.17 | 143 | 19.50 | 0.28 | 0.86 |

Table 4.5. Target list for asymmetry via the triple phase technique with at least 25% detection probability

| HR | Name | $\alpha$ | $\delta$ 2000 | SpType | V | B-V | $v \sin i$ | $\pi$ | $P_{asy.}^{80m}$ | $P_{asy.}^{100m}$ |
|---|---|---|---|---|---|---|---|---|---|---|
| 21 | 11Bet Cas | 000910.7 | +590859 | F2III-IV | 2.27 | 0.34 | 70 | 59.89 | 0.60 | 0.33 |
| 1666 | 67Bet Eri | 050751.0 | -050511 | A3III | 2.79 | 0.13 | 179 | 36.71 | 0.00 | 0.46 |
| 4357 | 68Del Leo | 111406.5 | +203125 | A4V | 2.56 | 0.12 | 181 | 56.52 | 0.00 | 0.46 |
| 6556 | 55Alp Oph | 173456.1 | +123336 | A5III | 2.08 | 0.15 | 219 | 69.84 | 0.77 | 0.81 |
| 8162 | 5Alp Cep | 211834.8 | +623508 | A7V | 2.44 | 0.22 | 246 | 66.84 | 0.92 | 0.92 |

Table 4.6. Target list for asymmetry via the differential phase technique with at least 25% detection probability

| HR | Name | $\alpha$ | $\delta$ 2000 | SpType | V | B-V | $v \sin i$ | $\pi$ | $P_{\Delta\phi}^{80m}$ | $P_{\Delta\phi}^{100m}$ |
|---|---|---|---|---|---|---|---|---|---|---|
| 21 | 11Bet Cas | 000910.7 | +590859 | F2III-IV | 2.27 | 0.34 | 70 | 59.89 | 0.30 | 0.12 |
| 403 | 37Del Cas | 012549.0 | +601407 | A5III-IV v | 2.68 | 0.13 | 113 | 32.81 | 0.49 | 0.68 |
| 623 | 14 Ari | 020925.3 | +255623 | F2III | 4.98 | 0.33 | 154 | 10.19 | 0.43 | 0.54 |
| 840 | 16 Per | 025035.1 | +381907 | F2III | 4.23 | 0.34 | 149 | 25.54 | 0.51 | 0.63 |
| 1298 | 38Omi1Eri | 041151.9 | -065015 | F2II-III | 4.04 | 0.33 | 96 | 25.98 | 0.15 | 0.27 |
| 1392 | 69Ups Tau | 042618.5 | +224849 | A8Vn | 4.28 | 0.26 | 196 | 21.07 | 0.55 | 0.65 |
| 1394 | 71 Tau | 042620.8 | +153706 | F0V | 4.49 | 0.25 | 192 | 20.86 | 0.40 | 0.49 |
| 1560 | 61Ome Eri | 045253.7 | -052710 | F4III+A6III | 4.39 | 0.25 | 153 | 14.39 | 0.35 | 0.45 |
| 1666 | 67Bet Eri | 050751.0 | -050511 | A3III | 2.79 | 0.13 | 179 | 36.71 | 0.56 | 0.69 |
| 2540 | 34The Gem | 065247.3 | +335740 | A3III | 3.60 | 0.10 | 128 | 16.59 | 0.21 | 0.34 |
| 2777 | 55Del Gem | 072007.4 | +215856 | F2IV | 3.53 | 0.34 | 111 | 55.45 | 0.27 | 0.42 |
| 3757 | 23 UMa | 093131.7 | +630343 | F0IV | 3.67 | 0.33 | 140 | 43.20 | 0.59 | 0.72 |
| 3888 | 29Ups UMa | 095059.4 | +590219 | F2IV | 3.80 | 0.29 | 110 | 28.35 | 0.37 | 0.52 |
| 4357 | 68Del Leo | 111406.5 | +203125 | A4V | 2.56 | 0.12 | 181 | 56.52 | 0.55 | 0.67 |
| 4399 | 78Iot Leo | 112355.5 | +103145 | F4IV | 3.94 | 0.41 | 20 | 41.26 | 0.46 | 0.00 |
| 4368 | 74Phi Leo | 111639.7 | -033906 | A7IVn | 4.47 | 0.21 | 225 | 16.69 | 0.00 | 0.55 |
| 4554 | 64Gam UMa | 115349.8 | +534141 | A0Ve | 2.44 | 0.00 | 168 | 38.99 | 0.33 | 0.55 |
| 4660 | 69Del UMa | 121525.6 | +570157 | A3V | 3.31 | 0.08 | 177 | 40.05 | 0.26 | 0.41 |
| 4733 | 14 Com | 122624.1 | +271606 | F0p | 4.95 | 0.27 | 227 | 11.92 | 0.56 | 0.66 |
| 5107 | 79Zet Vir | 133441.6 | -003545 | A3V | 3.37 | 0.11 | 173 | 44.55 | 0.16 | 0.27 |
| 5127 | 25 CVn | 133727.6 | +361742 | A7III | 4.82 | 0.23 | 204 | 17.01 | 0.45 | 0.55 |
| 5435 | 27Gam Boo | 143204.7 | +381830 | A7III | 3.03 | 0.19 | 139 | 38.29 | 0.52 | 0.68 |
| 5511 | 109 Vir | 144614.9 | +015334 | A0V | 3.72 | -0.01 | 351 | 25.35 | 0.22 | 0.33 |
| 5793 | 5Alp CrB | 153441.3 | +264253 | A0V+G5V | 2.23 | -0.02 | 133 | 43.65 | 0.09 | 0.27 |
| 5867 | 28Bet Ser | 154611.3 | +152519 | A2IV | 3.67 | 0.06 | 170 | 21.31 | 0.14 | 0.24 |
| 6095 | 20Gam Her | 162155.2 | +190911 | A9III | 3.75 | 0.27 | 141 | 16.69 | 0.55 | 0.67 |
| 6410 | 65Del Her | 171501.9 | +245021 | A3IV | 3.14 | 0.08 | 290 | 41.55 | 0.60 | 0.70 |
| 6556 | 55Alp Oph | 173456.1 | +123336 | A5III | 2.08 | 0.15 | 219 | 69.84 | 0.77 | 0.84 |
| 7235 | 17Zet Aql | 190524.6 | +135148 | A0Vn | 2.99 | 0.01 | 317 | 39.18 | 0.44 | 0.56 |
| 7377 | 30Del Aql | 192529.9 | +030653 | F3IV | 3.36 | 0.32 | 85 | 65.05 | 0.12 | 0.27 |
| 7420 | 10Iot2Cyg | 192942.3 | +514347 | A5Vn | 3.79 | 0.14 | 226 | 26.63 | 0.60 | 0.71 |
| 7528 | 18Del Cyg | 194458.5 | +450751 | B9.5IV+F1V | 2.87 | -0.03 | 149 | 19.07 | 0.11 | 0.26 |
| 7740 | 33 Cyg | 201323.9 | +563404 | A3IV-Vn | 4.30 | 0.11 | 268 | 21.41 | 0.51 | 0.61 |
| 8028 | 58Nu Cyg | 205710.4 | +411002 | A1Vn | 3.94 | 0.02 | 241 | 9.17 | 0.44 | 0.57 |

Table 4.6—Continued

| HR | Name | $\alpha$ | $\delta$ 2000 | SpType | V | B-V | $v \sin i$ | $\pi$ | $P_{\Delta\phi}^{80m}$ | $P_{\Delta\phi}^{100m}$ |
|---|---|---|---|---|---|---|---|---|---|---|
| 8130 | 65Tau Cyg | 211447.5 | +380244 | F2IV | 3.72 | 0.39 | 89 | 47.80 | 0.18 | 0.34 |
| 8162 | 5Alp Cep | 211834.8 | +623508 | A7V | 2.44 | 0.22 | 246 | 66.84 | 0.93 | 0.89 |
| 8781 | 54Alp Peg | 230445.7 | +151219 | B9V | 2.49 | -0.04 | 148 | 23.36 | 0.12 | 0.29 |

# Chapter 5

# The Effect of Rotation on Spectrum of Vega

## 5.1 Introduction

With the announcement of the detection of the interferometric signature of rapid rotation in Vega (Peterson et al., 2004, 2006b; Aufdenberg et al., 2006), a number of questions were raised about the fundamental standard. Earlier suggestions of rapid rotation were based on the high luminosity (Petrie, 1964; Gray, 1988) of the object and the unusual shapes of the weak lines in the spectrum (Gulliver, Hill, & Adelman, 1994; Hill, Gulliver, & Adelman, 2004). The high luminosity is immediately explained using Roche models for the figure of the rotating star, von Zeipel's theorem (von Zeipel, 1924) to characterize the temperature distribution, and adopting a nearly pole-on geometry, required by the small line widths (Gray, 1988).

But this model, requiring a star rotating near breakup, raises the question of whether such fundamental issues as Vega's composition, mass, and age, are accurately known. It has been recognized for some time that Vega appears metal poor (Sadakane & Nishimura, 1981; Adelman & Gulliver, 1990). And although it has been known since the early 20th century that masses deduced from luminosity and radius measurements are strongly affected by composition, recent mass and age determinations have largely assumed solar composition, the assumption being that sharp-lined A stars often show abundance peculiarities that are assumed due to diffusion and generally confined to surface layers. The recognition of rotation velocities approaching breakup renders that assumption unlikely, since rotation-driven circulation is likely to mix the envelope completely and deeply over times short compared to operable diffusion timescales.

Furthermore, the large surface temperature gradients that would be associated with rapid rotation raise a new question: how seriously are simple, single model atmosphere analyses of the spectrum affected by the composite

nature of the atmosphere? The peculiar line shapes add to this concern. A full analysis of the spectrum, or at least representative spectral features, seems necessary to demonstrate that we understand the peculiar line profiles and are able to derive reliable abundances.

This in turn requires high resolution, high SNR spectra comparable to those used by Hill, Gulliver, & Adelman (2004). The spectra of Vega available on the ELODIE archive provide us the necessary resolution and low noise; we describe those data in § 5.2. The computation of the synthetic spectra based on a rotational model are described in § 5.3 and the deduced abundances and other characteristics are reported in § 5.4, including the discovery that significant macroturbulence must be adopted. In § 5.5 we discuss the implications of the abundance profile and argue that the suggestion that Vega belongs to the $\lambda$ Bootis class of objects is probably correct. We note that the effect of rotation on the line strengths depends strongly on the line considered and propose a simple resolution to the prediction of large departures from LTE in the Fe I spectrum that have not been seen in practice. We examine more closely the issue of rotational mixing and conclude that the abundances we find here likely represent the material out of which Vega was formed. Lastly, we estimate the mass and age of Vega based on this composition.

After submitting the manuscript of this study to the Astrophysical Journal we found a paper (Takeda, Kawanomoto, & Ohishi, 2008) that had been recently accepted for publication in the same Journal which undertakes an analysis of their previously published (Takeda, Kawanomoto, & Ohishi, 2007) spectra toward understanding Vega's rotation, much along the lines taken earlier (Gulliver, Hill, & Adelman, 1994; Hill, Gulliver, & Adelman, 2004). These authors draw a number of conclusions in agreement with what we find here. But they also arrive at quite a different physical model of Vega, concluding in the process that errors were made in the reductions of the published interferometry. We will comment on these results at the appropriate points.

## 5.2 The Observational Data

The Vega spectra we used are from the ELODIE archive (Moultaka et al., 2004), which contains high-resolution ($R \sim 42,000$) echelle spectra from the ELODIE spectrograph obtained at the Observatoire de Haute-Provence 1.93 m telescope. The ELODIE data pipeline automatically extracts the spectra, establishes the dispersion, and corrects for scattered light. The spectra used here were obtained between 1996 and 2004. The wavelength rectified spectra covering $\lambda\lambda$ 4000-6800 are provided with 0.05 Å sampling.

Barycenter corrections were required before co-adding the spectra. To improve the signal-to-noise ratio (SNR) which is 250 for a typical spectrum, we co-added 49 out of 71 available spectra. In the process we rejected spectra whose SNR was less than 100 and those showing noticeable fringing. We also replaced bad pixels whose residuals in individual spectra were 5 times larger than the typical noise by interpolating adjacent pixels. The co-added spectra were converted to a residual intensity scale by normalizing them to the scale of the synthetic spectra described in § 5.3. The resultant spectra, segments of which are shown in Figures 5.1 and 5.2, were then compared to the synthesized spectra for the abundance analysis. The SNRs of the co-added spectra were estimated to range from 750 to 2,200 depending on the spectral regions.

Besides the ELODIE spectra, spectra of comparably high SNR and resolution of Vega have been obtained at the Dominion Astrophysical Observatory (DAO; Gulliver, Hill, & Adelman, 1994; Hill, Gulliver, & Adelman, 2004) and the Okayama Astrophysical Observatory (OAO; Takeda, Kawanomoto, & Ohishi, 2007). The DAO spectra (SNR $\sim 3,300$) have not yet been released publicly. However they are available as part of a graphic toolkit[1] which allows one to examine sections of spectra at high resolution and identify lines and probable blends. We made extensive use of this tool during this investigation.[2]

Also recently published are OAO spectra (SNR from 1,000 to 2,000 on average) covering $\lambda\lambda$ 3900-8800. However, these spectra display emission (e. g., $\sim \lambda\,4560$) and absorption (e. g., $\sim \lambda\,6060$) features and show the head of the Paschen continuum to be strongly in emission, features not reported elsewhere. So we have chosen to focus exclusively on the ELODIE data set.

## 5.3 Computations

We assume Vega can be described by a gravity-darkened Roche spheroid in solid-body rotation, with a point mass gravitational potential, showing a temperature distribution varying according to von Zeipel's theorem (von Zeipel, 1924), and seen nearly pole-on (e. g., Peterson et al., 2006b; Aufdenberg et al., 2006). Because the recent interferometric measurements taken at the Navy Prototype Optical Interferometer (NPOI; Armstrong et al., 1998) and the Center for High Angular Resolution Astronomy (ten Brummelaar et al., 2005) array yield closely similar model parameters, we adopt the parameters ob-

[1] `http://www.brandonu.ca/physics/gulliver/ccd_atlases.html`

[2] At the same time R.L. Kurucz (2007, private communication) provided a high resolution synthesized spectrum for Vega in the 450–500 nm region based on a line list and gf values calibrated to a solar spectrum which proved extremely useful.

tained from the NPOI data (Peterson et al., 2006b) for synthesizing spectra; the model has a fractional rotation velocity, $\omega = 0.926$, a polar surface gravity of $\log g_{\rm p} = 4.074$, a polar effective temperature of $T_{\rm p} = 9988\,{\rm K}$, an inclination of the rotational axis to the line of sight $i = 4.54\,^{\circ}$, and a projected rotational velocity of $v \sin i = 21.7\,{\rm km\,s^{-1}}$. For details of fitting Roche models to the NPOI data see Peterson et al. (2006a), and for issues specific to Vega see Peterson et al. (2006b), respectively.

To calculate the emergent spectrum we constructed a square $256 \times 256$ grid which contains the apparent disk of the star, calculated the stellar parameters at the center of each cell that actually fell on the flattened disk, and computed an emergent flux as a function of $\lambda$, $\mu$ (cosine of the angle between the local normal and the line of sight), $T_{\rm eff}$, $g_{\rm eff}$ (local gravity reduced by centrifugal force), and projected velocity using the ATLAS9 model atmosphere grid (Castelli & Kurucz, 2003) and the atomic line data given in the extensive compilation of Kurucz & Bell (1995). The fluxes were integrated over the disk to yield the synthetic model spectrum. In these calculations LTE, hydrostatic equilibrium, and plane-parallel atmospheres were assumed to represent the star's surface locally.

Concerns have been raised recently (Aufdenberg et al., 2006; Monnier et al., 2007) about the rigorous applicability of the von Zeipel theorem in the parts of the disk of a rotating star that are rendered cool enough to generate convection. We believe the issue is not relevant to Vega. First, in our model the temperature drops to about 7600 K at the equator, and the effective gravity in turn decreases to about $\log g \sim 3.5$ although a 7500K atmosphere certainly has some convection. From a model atmosphere with $T_{\rm eff} = 7500\,{\rm K}$, $\log g = 3.5$ we find the reduced density and in turn increased fraction of hydrogen ionized compared to the main sequence, substantially decreases the extent of the convective region and the efficiency of the resulting convection. Convection carries significant flux only in the range of $1 \leq \tau_{Rosseland} \leq 30$, well out from the interior where the flux requirement is established.

## 5.4 Results

### 5.4.1 Line Shapes

The abundance analysis was done by adjusting each element's abundance until the model spectra fit the co-added spectra. Since Vega's lines are sharp and blending is minimal, the process of adjusting the abundances was straightforward. Several representative regions of the co-added ELODIE spectrum are

shown in Figures 5.1 and 5.2. Weak lines throughout the spectrum show not only the flat-bottomed shapes (Cr II $\lambda$ 4565, S I $\lambda$ 6052, and Fe II $\lambda$ 6147) as noted in recent studies (Gulliver, Hill, & Adelman, 1994; Hill, Gulliver, & Adelman, 2004) but also weakly "self-reversed" shapes such as Mg I $\lambda$ 4702 and Ca I $\lambda$ 6162 and "V" shapes such as He I $\lambda$ 4713 and O I $\lambda$ 6046.

The unusual shapes of the weak lines are strongly correlated with excitation and ionization potential and can be understood in terms of how the Boltzmann factors amplify the temperature gradient across the disk. Since Vega is seen nearly pole on, the center of the apparent disk is almost exactly at one pole, the hottest point on the star. On the other hand, the limb is nearly the equator which is not only 2,400 K cooler than the pole, but the visible gas is actually cooler still owing to the simple projection effects associated with limb-darkening. Therefore the bound states responsible for the lines seen from the light elements such as He I, O I, Mg II, Al II, and Si II whose ionization and excitation potentials are quite high are excited mostly at the axis with zero projected velocity. There is almost no contribution to the line profiles from the rotationally shifted equatorial region, resulting in "V" shapes. The lower the excitation potentials the lines have, the more enhanced the contribution from the more rapidly rotating equatorial regions becomes and the wider and more square shaped the line profiles get. For the elements such as Ca I, Fe I, and Ba II with the lowest excitation potentials one sees a mild double-horned shape ("self-reversed") as the contribution from the equatorial region completely dominates the profile. In this sequence the flat-bottomed shape is formed at intermediate excitation potentials such as those of the lines of Cr II and Fe II. Our synthetic spectra predict well this sequence of line shapes as shown in Figure 5.2, where three regions of the ELODIE spectrum, overplotted with our synthetic spectrum, are shown. We see that weak Fe II lines tend to have a flat-bottomed shape while weak Fe I lines show a self-reversed shape. Examination of data presented by Gulliver, Hill, & Adelman (1994) and particularly in Hill, Gulliver, & Adelman (2004) suggests these shapes are present in their data as well.

### 5.4.2 Macroturbulence

In the process of the spectral synthesis, in order to fit the shapes of the weak line we found we had to reduce the resolution of the spectra well below the nominal resolution of 42,000 of the ELODIE spectra, ultimately adopting a resolution of about 25,000 as shown in Figure 5.3. We interpret this additional broadening, which was accomplished by convolving the synthetic spectrum with a Gaussian, as adding $10\,\mathrm{km\,s^{-1}}$ of macroturbulence to the

nominal ELODIE resolution (also assumed to be a Gaussian). The effect of this additional broadening is most noticeable in steep-sided line profiles (e. g., Mg I $\lambda\,4703$ and Ni I $\lambda\,4713$), as shown in Figure 5.3. As a result the value determined for the macroturbulence comes from low excitation lines and hence refers more to the equatorial regions than the polar regions. As might be expected, "V" shaped lines such as He I $\lambda\,4713$ are insensitive to the macroturbulence, as also shown in Figure 5.3. This is a very interesting result which we discuss at more length below. One caution is immediately apparent though: line widths might not be reliable indicators of actual projected velocity, at least for stars seen at low inclination. At this point our analysis deviates sharply from the recent contribution from Takeda, Kawanomoto, & Ohishi (2008), who seem not to have considered the possibility of large scale non-thermal line broadening. That there could, and even should, be turbulence on large scales in the atmosphere of Vega seems easy to justify. Even very slow, $\mathrm{cm\,s^{-1}}$, subsurface circulation currents will be magnified by the many order of magnitude drop in density found in the outer envelope, as required by the equation of continuity. Add to this a very strong Coriolis force owing to the rapid rotation and a surface covered with large eddies - cyclones - is to be expected. Ignoring this possibility, Takeda, Kawanomoto, & Ohishi (2008) were forced to adopt a relatively slowly rotating model, creating a clear conflict with the interferometric measurements (Peterson et al., 2006b; Aufdenberg et al., 2006).

### 5.4.3 Abundance Analysis and Microturbulence

As is often the case, we found that it was generally not possible to find abundances for elements (or even the same ion of an element) which gave good fits to both strong and weak lines simultaneously. This is usually taken as a signal that some microturbulence needs to be introduced. To this end, we determined the abundances from the Fe II lines for two choices of the microturbulence, as shown in Figure 5.4. Here the abundances are given as the logarithm of the ratio of the number of an element to that of total elements, $\log \frac{N_{\mathrm{el}}}{N_{\mathrm{tot}}}$. Castelli & Faraggiana (1979) and Sadakane & Nishimura (1981) have previously noted that the influence of the microturbulence is less important in the visual region for lines of intermediate strengths about $40 \sim 70\,\mathrm{m\AA}$, which we also found. For Fe II, which has the widest range of equivalent widths, we find both the scatter and any trend with equivalent width are significantly reduced for a microturbulence of about $2\,\mathrm{km\,s^{-1}}$ which we subsequently adopt. The O I triplets also support $2\,\mathrm{km\,s^{-1}}$ (e. g., Figure 5.2 which shows only the case for $2\,\mathrm{km\,s^{-1}}$ ).

Table 5.1 shows the deduced abundances for Vega with a microturbulence of $\xi_T = 2\,\mathrm{km\,s^{-1}}$. In selecting lines we eliminated severe blends but included weak blends where we felt reliable abundances could be obtained. The columns are the laboratory wavelength, lower excitation potential, equivalent width, $\log gf$, and the deduced abundance ($\log \frac{N_{\mathrm{el}}}{N_{\mathrm{tot}}}$). Blends we have decided to retain are noted in the last column. The abundances for elements with only single lines such as Al II, S I, Mn I, and Ni I must be considered uncertain. Even where there was no obvious blending, abundances were determined exclusively by spectral synthesis. Nevertheless, we give equivalent widths for comparison with recent work; agreement is within 1–2 mÅ typically. Equivalent widths are missing where lines were not able to be measured due to "one-sided" blends or difficulty in defining the local continuum level.

Notable in Table 5.1 is the discrepancy between Fe I and Fe II abundances. The abundances of Fe reported by Adelman & Gulliver (1990) do not show this dramatic lack of balance, and this might be viewed as supporting the smaller temperature gradient derived by Gulliver, Hill, & Adelman (1994) and Hill, Gulliver, & Adelman (2004). In contrast with Fe, the abundances of Mg I and Mg II shown in Table 5.1 do not show similar behavior. We discuss this result further below.

## 5.5 Discussion

### 5.5.1 How Does Rotation Affect Abundances?

The main difference between a pole-on rapidly rotating star, as modeled here, and a classical plane-parallel stellar atmosphere model is that for the same integrated colors, the rotating model has some fraction of its surface at both higher and lower local effective temperatures than the non-rotating model. The expected effect is that there will be spectral lines in a range of excitation and ionization energies where the two models give similar results. For Vega this is the case when the sum of the excitation energy and ionization energy (for lines of ions such as Fe II) is about 10 eV. But for both higher and lower energy features the expanded range of temperatures will enhance line strengths, resulting in a decrease in the deduced abundances from those lines (described as "intensification" by Takeda, Kawanomoto, & Ohishi, 2008).

We see that trend here. Table 5.2 summarizes the results of two recent analyses of Vega with non-rotating models (Sadakane & Nishimura, 1981; Adelman & Gulliver, 1990) along with the element-by-element results determined here. Our results from Mg I, Mg II, Al II, Si II, Ti II, Cr II, Mn I, and Fe II are about

-0.6 dex below solar, roughly that found by earlier authors. These are mostly the dominant ionization stages and thus yield fairly stable abundances. Other ions, including C I, Ca I, Sc II, Fe I, Ni I, and Ba II are deficient by about -1.0 dex, or even more, than the solar abundances (C I by -0.6), and are depressed by typically several tenths dex compared to the earlier studies, in this case because of their relatively small excitation and ionization energies.

On the other side, the He abundance we deduce, $N_{\rm He}/N_{\rm tot} = 0.072 \pm 0.004$, which is essentially solar (0.078), is substantially higher than that found by Adelman & Gulliver (1990), running counter to expectations. The result determined here is based on five of the six lines in the ELODIE spectral window that are expected to be measurable ($\lambda\,5875$ is heavily involved with atmospheric water vapor lines), while the helium abundance of Adelman & Gulliver (1990) is based on $\lambda\,4471$ only. Otherwise, we have no explanation for why we obtain a larger helium abundance.

In broadest terms, we find that if one can determine abundances from lines of the dominant ionization stage of an element, the errors induced by not accounting for rotation are small. Where lines from the dominant ionization stage are not accessible (e. g.,Ba III), one can expect large corrections to be required when standard, model-atmosphere analyses are applied to objects rotating near breakup.

One interesting example of the problems that can arise because of the corrections required between different ionization stages of the same element, involves the ionization balance between Fe I and Fe II. Problems with the Fe I/Fe II ionization balance have been reported for a wide range of stars (e. g., Gigas, 1986; Allende Prieto et al., 1999; Thévenin & Idiart, 1999; Johnson, 2002). For Vega, departures from LTE are predicted to produce about 0.3 dex errors in abundances deduced from Fe I lines while Fe II lines are barely affected (Gigas, 1986). However, these calculations are difficult owing to the complexity of the atom and the lack of accurate collision and photoionization cross sections. For example, Pradhan et al. (1995) have found that many of the photoionization cross sections of Fe I are significantly higher than those previously adopted (e. g., Gigas, 1986) with the possibility that the actual corrections from departures from LTE are larger still.

The problem with the Fe balance in Vega is confusing since at first glance, straightforward LTE analyses (Sadakane & Nishimura, 1981; Adelman & Gulliver, 1990) provide apparent agreement between the abundances deduced from the two ions. This is in contrast to the sizable departures from LTE required in other similar objects.

However, even though we assume LTE in our analysis here, we also find a serious iron ionization imbalance amounting to $\sim 0.4$ dex, but in the opposite

sense of that induced by non-LTE. To understand the origin of this imbalance we reanalyzed representative lines from the two iron ionization states and, as a check, from the two magnesium ions present, using a standard plane-parallel model. We find that rotation induces an apparent 0.35 dex error in the Fe I/Fe II ionization balance, while the corresponding effect in the Mg I/Mg II balance is only about 0.1 dex.

Thus we reach the amusing conclusion that a simple LTE analysis of Vega using models which do not account for rotation give a good ionization balance because of a nearly complete cancellation of the effects of photoionization-driven departures from LTE in the Fe I ion, on the one hand, and an enhanced Fe I line spectrum contributed by the extensive cool equatorial regions of the model owing to the favorable viewing geometry, on the other. Note however, the near balance between these two effects may disappear when one analyses lines in either the ultraviolet or infrared, owing to the changing relative contribution of the equatorial regions to the overall light.

We note that Takeda, Kawanomoto, & Ohishi (2008) have independently commented on the near cancellation of departures from LTE versus the effects of rotation in the iron ionization balance. However, in their calculation the rotation induced errors are predicted to be about half those calculated here, owing to the much lower rotation velocity and the corresponding dramatically reduced temperature gradient ($\sim 900$ K) in their model.

### 5.5.2 Is Vega a $\lambda$ Bootis Star?

Since Baschek & Slettebak (1988) remarked that Vega showed an abundance pattern similar to the $\lambda$ Bootis stars, which are a class of metal poor A type stars with normal rotation, several studies (e. g., Venn & Lambert, 1990; Ilijić et al., 1998) reported that Vega may be a mild $\lambda$ Bootis star. We confirm that result here. The abundance pattern we deduce matches well the main characteristics of the abundance patterns of $\lambda$ Bootis stars as summarized, for example by Heiter (2002). Elements such as Si, S, Ca, and Sc fall in the middle of their respective typical ranges while O, Mg, Ti, Cr, Mn, and Fe are on the high side of normal and Ni and Ba are on the low side. While most elements fit the $\lambda$ Bootis abundance pattern well, C and Al are somewhat out of the reported range. The Al abundance is based on one line and is not certain, while carbon is off the lower end of the pattern reported by Heiter (2002). However Pauzen et al. (1999), in an extensive discussion of carbon and oxygen in this group of objects, find several objects with carbon abundances as low as -0.7 dex with respect to the Sun. We conclude that Vega would not be rejected as a $\lambda$ Bootis star on the basis of its carbon abundance and the rest of

the abundances determined here are very much in keeping with membership in this group.

### 5.5.3 Is Vega Well Mixed?

A presumption, often unstated, about the nature of $\lambda$ Boo stars is that the deviations from solar composition are limited to surface layers (e. g., Baschek, 1992; Holweger & Stürenburg, 1993), much the same as has been concluded for the Ap and Am stars which also occupy this part of the H-R diagram. But there has always been some concern about that assumption since unlike the latter groups the $\lambda$ Boo stars appear to have a distribution of rotation velocities similar to normal stars (e. g., Holweger & Stürenburg, 1993).

We argue here that since Vega is rotating at a significant fraction of breakup and yet displays fairly typical $\lambda$ Boo characteristics, it is unlikely that these composition anomalies are limited to the surface; more likely, Vega is well mixed. The literature on rotationally induced mixing has generally focused on the surface layers and the question of whether the Ap and Am phenomena could be understood as due to diffusive separation (e. g., Charbonneau, 1993) and not on how fast an inhomogeneity introduced on the surface would be mixed throughout the envelope.

However, recent efforts to include the effects of rotation in evolutionary calculations of massive stars (Meynet & Maeder, 1997) have led to an examination of how inhomogeneities will be redistributed through a star (Talon et al., 1997; Ekström et al., 2008), suggesting that extensive mixing is to be expected. In fact, at the highest velocities in models down to 3 $M_{\odot}$, the lowest mass examined, the mixing is predicted to be so deep there is the possibility that some of the nuclear products from the CNO burning region might be mixed to the surface.

This is an interesting possibility, given the low carbon abundance we have found. From this point of view, missing is an estimate of the nitrogen abundance, the lines of which are out of the ELODIE spectral range. However measurements of nitrogen line equivalent widths have been reported elsewhere. To fill in the abundance of this important nuclide taking full account of the effects of rotation, we have calculated the abundances for the nitrogen equivalent widths reported in Venn & Lambert (1990) for $\lambda$ 7442.28 ($\log N/N_{\rm tot} = -4.05$, $[N/N_{\rm tot}] = +0.07$) and $\lambda$ 7468.29 ($\log N/N_{\rm tot} = -4.02$, $[N/N_{\rm tot}] = +0.1$) ($\lambda$ 7423 appears to be blended and we exclude it here), finding values quite close to those deduced by Venn & Lambert (1990) at about 0.085 dex above solar. This is an intriguing result. Although it is difficult to know what "normal" is in this star, normalizing to oxygen gives [N/O] $\sim +0.2$ and [C/O] $\sim$

-0.5, which may very well indicate that some CN cycle processed material has been mixed into the envelope of the star. In this regard we note that Vega represents a rather unique object; a few other $\lambda$ Boo objects have projected velocities in the vicinity of $200\,\mathrm{km\,s^{-1}}$, but Vega is the one object known to rotate as fast as $275\,\mathrm{km\,s^{-1}}$, less than 10% from breakup in terms of angular velocity. However, without a better understanding of the composition of the material Vega started with, or other supporting information, we must leave this as just an intriguing possibility.

In summary, we believe a fairly strong case can be made for the outer layers of Vega being well mixed, possibly even down to the edge of its nuclear burning core. If this is so then we are looking at about 2 $M_\odot$ of material of highly unusual composition in an object that is much too young to display such extreme depletion in heavy elements. In this case the various mechanisms put forth to explain the $\lambda$ Boo phenomena that rely on its being limited to the superficial layers (e. g., Kamp & Paunzen, 2002) seem excluded for Vega. Some form of dust - gas separation, such as suggested by Venn & Lambert (1990) or Holweger (1992), may be involved but if so the mechanism likely must work at the time of Vega's formation since so much mass is involved.

### 5.5.4 Determination of the Age and Mass of Vega

We estimate the mass and age of Vega by locating its measured luminosity and polar radius in an appropriate evolution grid, as described in Peterson et al. (2006b). The interior models we adopt are from the BASTI database[3] (Pietrinferni, 2006, and references therein) which include evolutionary calculations using scaled solar and alpha-enhanced compositions for stellar masses up to $2.4\,M_\odot$. The composition found here is not a perfect fit to either of those mixtures, but the large enhancement of oxygen is about the same compared to the heavy metals as the alpha-enhanced mixture adopted there. Missing are the other alpha-rich elements at the enhanced levels, but given the dominance of oxygen even among these nuclei, that grid should give results more than adequate. To quantify how much the mismatch in the details of the distribution of abundances might affect the estimate we also calculate the mass and age using the scaled solar grid. In both cases, the heavy element fraction used is $\mathrm{Z} = 0.0093^{+0.0006}_{-0.0005}$ as calculated from Table 5.2 and assuming $[N_{\mathrm{el}}/N_{\mathrm{tot}}] = -0.7$ for abundances not obtained here.

For the alpha-enhanced composition we obtain $2.09 \pm 0.03 M_\odot$ and $536 \pm 29\,\mathrm{Myr}$ for the mass and age. The simple scaled solar abundances in turn yield

[3] `http://www.te.astro.it/BASTI/index.php`

$2.14 M_{\odot}$ and 541 Myr and since the alpha-enhanced models are a much closer match to Vega's composition it is clear the errors introduced by the slight mismatch are small compared to the other uncertainties.

As described in Peterson et al. (2006b), whether Vega is solar composition throughout or the derived abundances represent the actual overall composition, results in quite different estimates for the star's mass and age. Most previous authors have assumed an underlying solar composition yielding estimates of $2.3 M_{\odot}$ for the mass and an age in the neighborhood of 360 Myr. Since there is a distinct possibility that the composition we have derived applies to the star as a whole, Vega's estimated mass may be reduced and its implied age increased substantially. One immediate consequence of this is a growing clash with the properties of the so-called "Castor moving group" (Barrado y Navascués, 1998), which includes Castor ($\alpha$ Gem), Fomalhaut ($\alpha$ PsA) and Alderamin ($\alpha$ Cep), in addition to Vega, and whose members are estimated to have an age of $200 \pm 100$ Myr. Even with an assumed solar composition Vega's age was not a comfortable fit for inclusion in this group. The increased age we propose would make it an unlikely member.

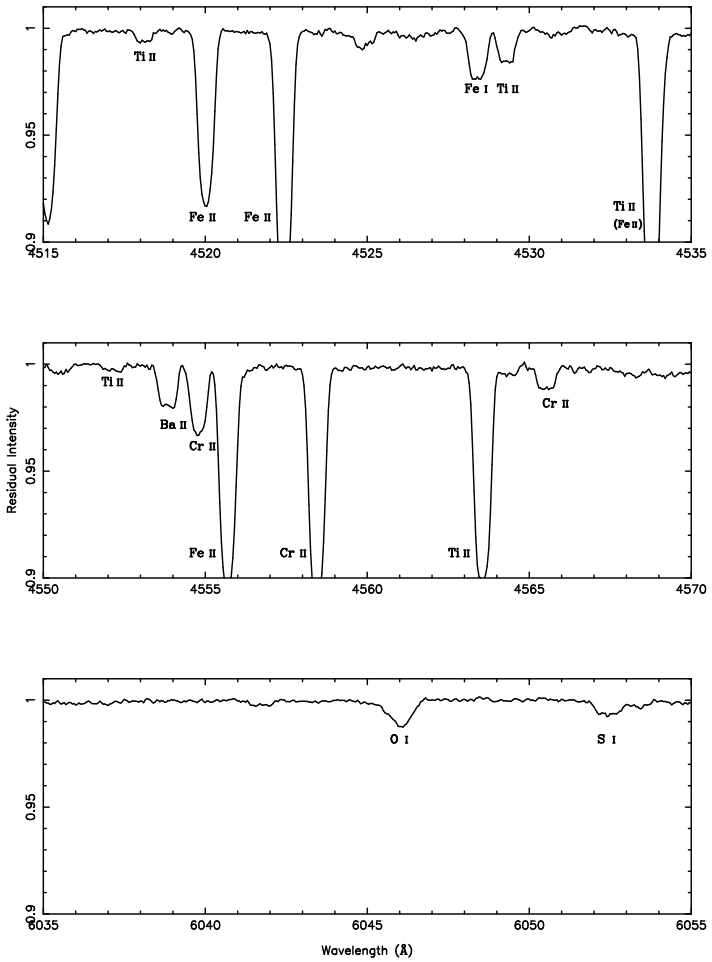


Figure 5.1 Shown are line profiles representative of the range of shapes encountered for weak lines in the ELODIE spectra of Vega. The shapes run from weakly "self-reversed" (e.g., Fe I $\lambda$ 4528 and Ba II $\lambda$ 4554) through flat-bottomed (Cr II $\lambda$ 4565 and S I $\lambda$ 6052) to "V"-shaped (O I $\lambda$ 6046). Where known, blends are indicated in parenthesis. Wavelengths are in the star's rest frame.

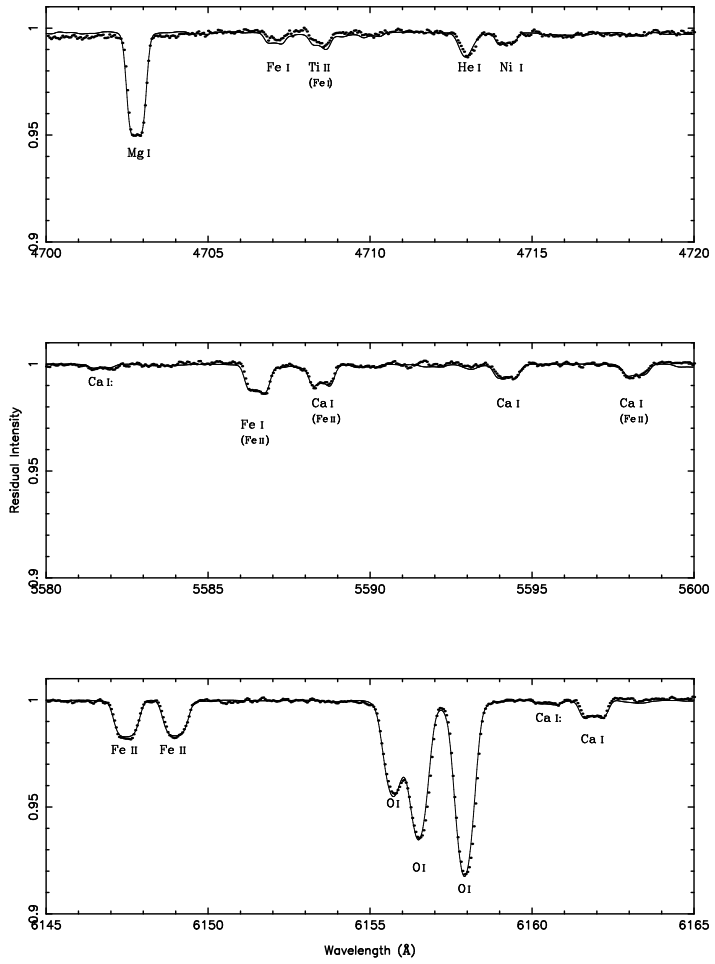


Figure 5.2 Plotted here are additional segments of spectra (dotted lines) showing the range of shapes of weak lines, as in Figure 5.1, only now overplotted with the synthetic spectra (continuous lines). Note particularly He I $\lambda$ 4713 which, with an excitation potential of 21 eV, is formed in a small region around the rotational pole and displays the corresponding "V" shape. At the other extreme Ca I $\lambda$ 6162 shows the weak double-horned ("self-reversed") shape reflecting its very low excitation potential, 1.9 eV; it is contributed exclusively by the cooler equatorial regions. Other lines showing this behavior are Ti II $\lambda$ 4708, Fe I $\lambda$ 5586, and Ca I $\lambda$ 5588, although all three are (weakly) blended. Two iron lines, Fe II $\lambda\lambda$ 6147 and 6149, at intermediate excitations of 3.9 eV above the 7.8 eV ionization potential of Fe I, show the expected flat-bottomed shapes, although seen against a slight variability in the background continuum. The weak Ca I lines indicated with ":" were not included in the abundance determination.

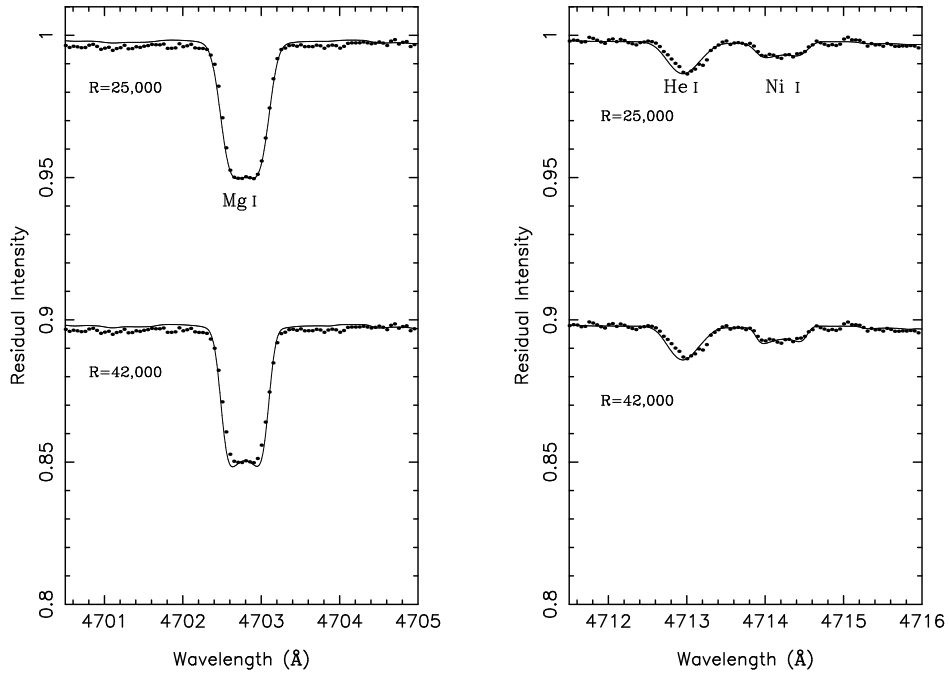


Figure 5.3 These figures plotted as in Figure 5.2 illustrate the need for line broadening in addition to rotation and microturbulence (in both panels the lower spectra are offset by 0.1). Mg I $\lambda$ 4702 shows the problem most clearly although it is also evident in Ni I $\lambda$ 4714. The nominal ELODIE resolution of 42,000 (assumed to be Gaussian) allows too much structure in the steep-sided line profiles. Reducing the resolution to 25,000 appears to be required, which we interpret as a contribution of about 10 km s$^{-1}$ of macroturbulence. The effect of adding this macroturbulence is to improve the fit dramatically in the bottoms of the weak, low-excitation lines while causing the line widths to be a bit wide. This suggests the actual projected rotation rate is below the adopted 21.7 km s$^{-1}$, as was suggested in the initial interferometric data reductions reported by Peterson et al. (2006b). Note that high excitation lines like He I $\lambda$ 4713 are not affected by the added macroturbulence.

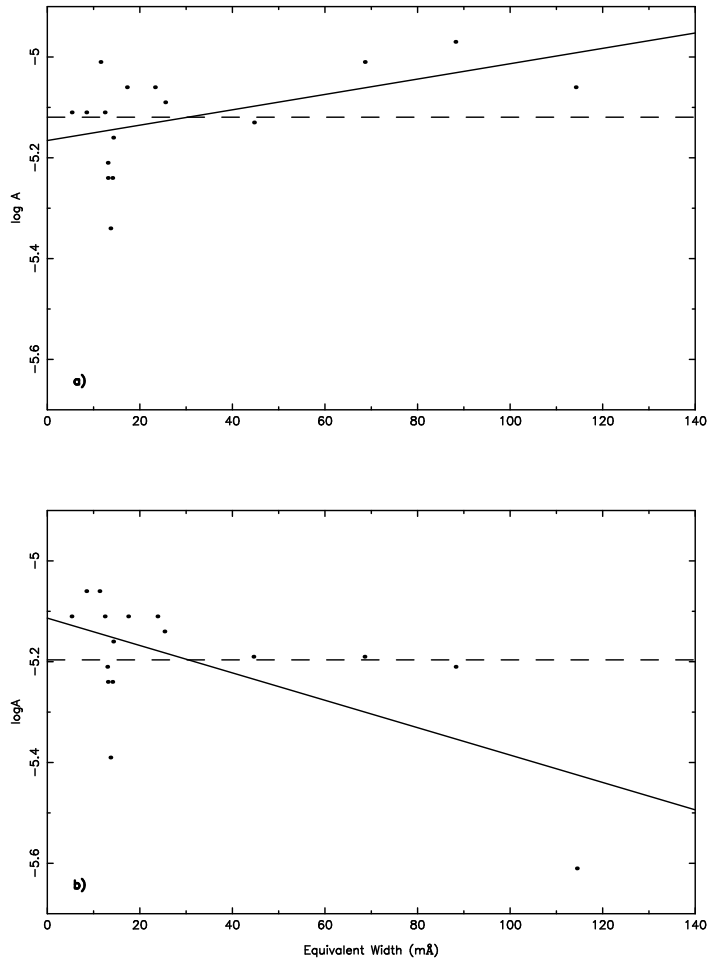


Figure 5.4 These plots show the derived abundances (data points) versus equivalent widths of Fe II lines for two different assumed values of the microturbulence. Panels a) and b) show the derived abundances for microturbulence values of $2\,\mathrm{km\,s^{-1}}$ and $4\,\mathrm{km\,s^{-1}}$, respectively. The dashed line shows the unweighted average abundances and the solid line shows the trend with equivalent width. We adopt a microturbulence of $2\,\mathrm{km\,s^{-1}}$ in our abundance determinations.

Table 5.1. The Abundance Analysis of Vega

| $\lambda$ (Å) | EP ($cm^{-1}$) | $w_\lambda$ ( mÅ) | $\log gf$ | $\log \frac{N_{el}}{N_{tot}}$ [a] | Blends |
|---|---|---|---|---|---|
| He I ($\frac{N_{He}}{N_{tot}}$ =0.072 ± 0.004 ) | | | | | |
| 4471.498 | 169087.008 | ··· | 0.052 | 0.070 | |
| 4713.139 | 169086.864 | 5 | -1.233 | 0.078 | Fe II λ 4713.193 |
| 4921.931 | 171135.000 | 8 | -0.435 | 0.060 | |
| 5015.678 | 166277.546 | ··· | -0.820 | 0.078 | Fe II λ 5015.755 |
| 6678.154 | 171135.000 | 5 | 0.329 | 0.070 | Fe II λ 6677.306 |
| C I ($\log \frac{N_C}{N_{tot}}$ = -4.14 ±0.04, $[N_C/N_{tot}]$[b]= -0.62) | | | | | |
| 4770.021 | 60352.639 | 7 | -2.052 | -4.16 | |
| 4771.730 | 60393.148 | 25 | -1.488 | -4.16 | |
| 4775.889 | 60393.148 | 7 | -2.013 | -4.16 | |
| 4932.050 | 61981.818 | 16 | -1.574 | -4.06 | |
| O I ($\log \frac{N_O}{N_{tot}}$ = -3.32 ± 0.04, $[N_O/N_{tot}]$ = -0.11) | | | | | |
| 5329.099 | 86625.757 | 34[c] | -1.730 | -3.31 | |
| 5329.690 | 86627.778 | ··· | -1.410 | -3.31 | |
| 5330.741 | 86631.454 | 24 | -1.120 | -3.31 | |
| 6046.438 | 88631.146 | 10 | -1.675 | -3.26 | |
| 6155.971 | 86625.757 | 77[d] | -1.051 | -3.36 | |
| 6156.778 | 86627.778 | ··· | -0.731 | -3.36 | |
| 6158.187 | 86631.454 | 59 | -0.441 | -3.36 | |
| Mg I ($\log \frac{N_{Mg}}{N_{tot}}$ = -5.12 ± 0.05, $[N_{Mg}/N_{tot}]$ = -0.66) | | | | | |
| 4702.991 | 35051.264 | 29 | -0.666 | -5.06 | |
| 5167.321 | 21850.405 | 81 | -1.030 | -5.06 | Fe I λ 5167.488 |
| 5172.684 | 21870.464 | 102 | -0.402 | -5.16 | |
| 5183.604 | 21911.178 | 119 | -0.180 | -5.16 | |
| 5528.405 | 35051.264 | 28 | -0.620 | -5.16 | |
| Mg II ($\log \frac{N_{Mg}}{N_{tot}}$ = -5.06 ± 0.04, $[N_{Mg}/N_{tot}]$ = -0.6) | | | | | |
| 4427.994 | 80619.500 | ··· | -1.210 | -5.06 | |
| 4433.988 | 80650.020 | ··· | -0.910 | -5.11 | Fe I λ 4433.782 |
| 4481.126 | 71490.190 | ··· | 0.740 | -5.01 | |
| Al II ($\log \frac{N_{Al}}{N_{tot}}$ = -6.22, $[N_{Al}/N_{tot}]$ = -0.65) | | | | | |
| 4663.046 | 85481.350 | ··· | -0.284 | -6.22 | |
| Si II ($\log \frac{N_{Si}}{N_{tot}}$ = -5.15 ± 0.05, $[N_{Si}/N_{tot}]$ = -0.66) | | | | | |
| 4128.054 | 79338.500 | 32 | 0.316 | -5.19 | Mn II λ 4128.129 |
| 4130.872 | 79355.020 | 54 | -0.824 | -5.19 | |
| 5055.984 | 81251.320 | 60 | 0.593 | -5.19 | |
| 6347.109 | 65500.470 | 118 | 0.297 | -5.09 | Mg II λ 6346.742 |
| | | | | | Mg II λ 6346.964 |
| 6371.371 | 65500.470 | 82 | -0.003 | -5.09 | |
| S I ($\log \frac{N_S}{N_{tot}}$ = -5.01, $[N_S/N_{tot}]$ = -0.3) | | | | | |
| 6052.674 | 63475.051 | 7 | -0.740 | -5.01 | |
| Ca I ($\log \frac{N_{Ca}}{N_{tot}}$ = -6.72 ± 0.12, $[N_{Ca}/N_{tot}]$ = -1.04) | | | | | |
| 4226.728 | 0.000 | ··· | 0.243 | -6.73 | |

Table 5.1—Continued

| $\lambda$ (Å) | EP ($cm^{-1}$) | $w_\lambda$ ( mÅ) | $\log gf$ | $\log \frac{N_{el}}{N_{tot}}$ [a] | Blends |
|---|---|---|---|---|---|
| 4434.957 | 15210.063 | ··· | -0.029 | -6.73 | |
| 4585.865 | 20371.000 | 1 | -0.386 | -6.68 | |
| 5588.749 | 20371.000 | 1 | 0.210 | -6.63 | |
| 5594.462 | 20349.260 | 5 | -0.050 | -6.63 | |
| 5598.480 | 20335.360 | 4 | -0.220 | -6.63 | Fe I $\lambda$ 5598.287 |
| 6162.173 | 15315.943 | 9 | 0.100 | -6.98 | |
| Sc II ($\log \frac{N_{Sc}}{N_{tot}}$ = -9.97 ± 0.05, $[N_{Sc}/N_{tot}]$ = -1.1) | | | | | |
| 4246.822 | 2540.950 | 5 | 0.320 | -10.02 | |
| 5526.79 | 14261.320 | 9 | 0.130 | -9.92 | |
| Ti II ($\log \frac{N_{Ti}}{N_{tot}}$ = -7.65 ± 0.09, $[N_{Ti}/N_{tot}]$ = -0.63) | | | | | |
| 4468.507 | 9118.260 | 70 | -0.600 | -7.82 | |
| 4529.474 | 12676.970 | 9 | -1.830 | -7.69 | |
| 4563.761 | 9850.900 | 57 | -1.010 | -7.51 | |
| 4589.958 | 9975.920 | 16 | -1.790 | -7.61 | Cr II $\lambda$ 4589.901 |
| 4708.665 | 9975.920 | 3 | -2.410 | -7.69 | |
| 4779.985 | 16515.860 | 12 | -1.420 | -7.59 | |
| 4805.085 | 16625.110 | 21 | -1.100 | -7.59 | |
| 5336.771 | 12758.110 | 12 | -1.700 | -7.72 | |
| Cr II ($\log \frac{N_{Cr}}{N_{tot}}$ = -6.91 ± 0.1, $[N_{Cr}/N_{tot}]$ = - 0.54) | | | | | |
| 4252.632 | 31117.390 | 6 | -2.018 | -6.97 | |
| 4261.847 | 25033.700 | 18 | -3.004 | -6.92 | Cr II $\lambda$ 4261.913 |
| 4554.988 | 32836.680 | 20 | -1.430 | -6.87 | |
| 4558.650 | 32854.310 | 61 | -0.660 | -6.87 | |
| 4565.740 | 32603.400 | 7 | -1.910 | -7.07 | |
| 4588.199 | 32836.680 | 48 | -0.830 | -6.87 | |
| 4592.049 | 32854.950 | 18 | -1.420 | -6.87 | |
| 4616.629 | 32844.760 | 16 | -1.530 | -6.87 | |
| 4618.803 | 32854.950 | 36 | -1.070 | -6.87 | |
| 4634.070 | 32844.760 | 29 | -1.220 | -6.82 | |
| 4812.337 | 31168.580 | 6 | -1.930 | -7.07 | |
| 4824.127 | 31219.350 | 39 | -1.220 | -6.72 | |
| 5334.869 | 32844.760 | 10 | -1.562 | -7.07 | |
| Mn I ($\log \frac{N_{Mn}}{N_{tot}}$ = -7.45, $[N_{Mn}/N_{tot}]$ = -0.8) | | | | | |
| 4783.405 | 18531.663 | 2 | 0.042 | -7.45 | |
| Fe I ($\log \frac{N_{Fe}}{N_{tot}}$ = - 5.51 ± 0.1, $[N_{Fe}/N_{tot}]$ =-0.97) | | | | | |
| 4132.058 | 12968.553 | 29 | -0.650 | -5.54 | Fe I $\lambda$ 4131.935 |
| | | | | | Fe I $\lambda$ 4131.971 |
| 4134.677 | 22838.321 | 8 | -0.490 | -5.54 | Fe I $\lambda$ 4134.42 |
| 4136.998 | 27543.001 | 4 | -0.540 | -5.54 | |
| 4250.119 | 19912.494 | 18 | -0.405 | -5.49 | Fe II $\lambda$ 4250.437 |
| 4250.787 | 12560.933 | 27 | -0.710 | -5.49 | Fe II $\lambda$ 4250.437 |
| 4260.474 | 19350.890 | 36 | -0.020 | -5.39 | |
| 4466.551 | 22838.321 | 9 | -0.590 | -5.36 | |
| 4476.019 | 22946.814 | 8 | -0.570 | -5.79 | Fe I $\lambda$ 4476.076 |
| 4528.614 | 17550.180 | 15 | -1.072 | -5.51 | |

Table 5.1—Continued

| $\lambda$ (Å) | EP ($cm^{-1}$) | $w_\lambda$ ( mÅ) | $\log gf$ | $\log \frac{N_{el}}{N_{tot}}$ [a] | Blends |
|---|---|---|---|---|---|
| 4918.994 | 23110.937 | 16 | -0.640 | -5.51 | Fe I $\lambda$ 4918.954 |
| 4920.502 | 22845.867 | 27 | -3.955 | -5.51 | Cr II $\lambda$ 4920.23 |
| 5324.179 | 25899.987 | 12 | -0.240 | -5.49 | |
| 5586.756 | 27166.818 | 11 | -0.210 | -5.59 | Fe II $\lambda$ 5587.114 |
| 5615.644 | 26874.548 | 15 | -0.140 | -5.44 | |
| Fe II ($\log \frac{N_{Fe}}{N_{tot}}$ = -5.12 ± 0.09, $[N_{Fe}/N_{tot}]$ = -0.58) | | | | | |
| 4258.154 | 21812.055 | 14 | -0.467 | -5.34 | Fe II $\lambda$ 4258.34 |
| 4520.224 | 22637.205 | 45 | -2.990 | -5.13 | |
| 4522.634 | 22939.358 | 69 | -2.700 | -5.01 | |
| 4576.340 | 22939.358 | 23 | -3.390 | -5.06 | |
| 4582.835 | 22939.358 | 17 | -3.570 | -5.06 | |
| 4583.837 | 22637.205 | 88 | -2.490 | -4.97 | Fe II $\lambda$ 4583.999 |
| 4596.015 | 50212.826 | ··· | -2.057 | -5.21 | Fe II $\lambda$ 4595.682 |
| 4620.521 | 22810.357 | 14 | -3.650 | -5.16 | |
| 4635.316 | 48039.090 | 13 | -1.650 | -5.21 | |
| 4656.981 | 23317.633 | 12 | -3.950 | -5.11 | Ti II $\lambda$ 4657.206 |
| 4663.708 | 23317.633 | 5 | -4.145 | -5.11 | |
| 4666.758 | 22810.357 | 11 | -3.700 | -5.01 | |
| 4670.182 | 20830.582 | 8 | -4.350 | -5.11 | Sc II $\lambda$ 4670.407 |
| 4923.927 | 23317.633 | 114 | -1.820 | -5.06 | |
| 5534.847 | 26170.181 | 25 | -2.930 | -5.09 | |
| 6147.741 | 31364.440 | 14 | -2.721 | -5.24 | |
| 6149.258 | 31368.450 | 13 | -2.724 | -5.24 | |
| Ni I ($\log \frac{N_{Ni}}{N_{tot}}$ = -6.79, $[N_{Ni}/N_{tot}]$ = -1.0) | | | | | |
| 4714.417 | 27260.894 | 3 | 0.160 | -6.79 | |
| Ba II ($\log \frac{N_{Ba}}{N_{tot}}$ = -11.21, $[N_{Ba}/N_{tot}]$ = -1.3) | | | | | |
| 4554.029 | 0.000 | 13 | 0.430 | -11.21 | |
| 4934.076 | 0.000 | 7 | -0.150 | -11.21 | Fe I $\lambda$ 4934.005 |

[a] For helium abundance, $\frac{N_{He}}{N_{tot}}$

[b] $[N_{el}/N_{tot}] = \log \frac{N_{el}}{N_{tot}} - \log (\frac{N_{el}}{N_{tot}})_\odot$

[c] The equivalent width is for the blend with O I $\lambda$ 5629.690.

[d] The equivalent width is for the blend with O I $\lambda$ 6156.778.

Table 5.2. Comparisons with the previous abundance studies

| Atomic Species | log M/H SN[a] | log M/H AG[b] | log $\frac{N_{\rm el}}{N_{\rm tot}}$ [c] This Work | $[N_{\rm el}/N_{\rm tot}]$[d] This Work |
|---|---|---|---|---|
| He I | ··· | -1.52 | -1.14 | -0.04 |
| C I | ··· | -3.81 | -4.14 | -0.62 |
| N I[e] | ··· | ··· | -4.03 | +0.09 |
| O I | ··· | ··· | -3.32 | -0.11 |
| Mg I | -4.61 | -5.07 | -5.12 | -0.66 |
| Mg II | -4.96 | -5.11 | -5.06 | -0.60 |
| Al II* | ··· | -6.33 | -6.22 | -0.65 |
| Si II | ··· | ··· | -5.15 | -0.66 |
| S I* | ··· | ··· | -5.01 | -0.30 |
| Ca I | -6.11 | -6.21 | -6.72 | -1.04 |
| Sc II | -9.42 | -9.62 | -9.97 | -1.10 |
| Ti II | -7.31 | -7.47 | -7.65 | -0.63 |
| Cr II | -6.90 | -6.76 | -6.91 | -0.54 |
| Mn I* | -6.87 | -7.16 | -7.45 | -0.80 |
| Fe I | -5.09 | -5.05 | -5.51 | -0.97 |
| Fe II | -5.09 | -5.12 | -5.12 | -0.61 |
| Ni I* | -5.94 | -6.38 | -6.79 | -1.00 |
| Ba II* | -10.25 | -10.58 | -11.21 | -1.30 |

Note. — The definition of the abundances we use differs from that adopted by SN and AG. For the helium abundance found here, the SN and AG abundances will be systematically larger than ours by 0.03 dex.

[a]Sadakane & Nishimura (1981)

[b]Adelman & Gulliver (1990)

[c]Abundances from Table 5.1

[d]Solar abundances have been taken from Grevesse & Sauval (1998)

[e]Abundance based on Venn & Lambert (1990) equivalent widths

*Based on only one line

# Chapter 6

# Updating Vega's Mass, Age, and Evolutionary Status

## 6.1 Introduction

We have described the abundance analysis of Vega by spectral synthesis in chapter 5, where we confirm that Vega is a $\lambda$ Boo star and argue that it is probably well mixed due to the meridional circulation induced by its rapid rotation. While another interferometric study (Aufdenberg et al., 2006) confirmed that Vega is rapidly rotating star, the recent spectral line shape studies (Hill, Gulliver, & Adelman, 2004; Takeda, Kawanomoto, & Ohishi, 2008) have suggested that Vega is rotating at only $\omega \sim 0.6$, very slowly compared with the interferometric values, leading to a rather different set of deduced parameters for the star.

It is necessary to resolve this inconsistency. For this purpose, we have expanded the code used to fit a gravity-darkened Roche models to NPOI interferometric data to include the ELODIE archival spectra. Because the high-resolution spectroscopy and high angular resolution interferometry provide significant constraints on the model, simultaneous fitting of both data sets provides us better estimates of the parameters.

The observational data for this study are described in the next section, and the Roche modeling is briefly summarized in § 6.3. In § 6.4, we describe the computations of the observables; the continuum flux, the hydrogen Balmer lines, the line profiles of Ca I $\lambda$ 6162 and Mg I $\lambda$ 4702 and the interferometric observables. For spectral synthesis, we adopt ATLAS12 model atmospheres specifically calculated for this purpose while we used ATLAS9 model atmospheres in Chapter 5. The ATLAS12 models has better opacity sampling than ATLAS9 models and explicitly allow for Vega's unusual composition. In the final section, we discuss the model fitting, compare this work with the previous

studies, note the abundance changes due to the new model parameters, and finally update our estimate of Vega's age and mass.

## 6.2 Observational Data

The interferometric data were taken by the NPOI (Armstrong et al., 1998) observation on 25 May 2001 in the visible (Peterson et al., 2006b). We focus here only on the closure phase data with a three element array (AW-AE-W7), which is very sensitive to asymmetries in the intensity distribution, for the reasons given by Peterson et al. (2006b). For details of the observations and much of the data reduction, see Peterson et al. (2006a).

Regarding the stellar absolute fluxes and energy distributions, we used the data in the visible/red (3300Å to 8000Å) from Hayes (1985). These data are not rigorously statistically independent, point to point, and to prevent the large number of data points from being given undue weight in the reductions we used only every fourth point as tabulated by Hayes (1985). In addition, we excluded the fluxes in the spectral regions affected by hydrogen lines or strongly contaminated by telluric lines. The hydrogen line profiles of $H_\alpha$, $H_\beta$, and $H_\gamma$ were taken from Peterson (1969). The Vega spectra used here are from the ELODIE archive (Moultaka et al., 2004), which contains high-resolution ($R \sim 42,000$) echelle spectra from the ELODIE spectrograph obtained at the Observatoire de Haute-Provence 1.93 m telescope. The details of the reduction of the coadded ELODIE spectra are given in § 5.2. For model fitting of individual spectral lines, Ca I $\lambda$ 6162 and Mg I $\lambda$ 4702 were used because those have low excitation potentials thus show clearly the double-horned shapes, are relatively free of blends, have a clean continuum, and good signal-to-noise.

## 6.3 Modeling

As already described in Chapters 2 and 5, we model Vega as a rapidly rotating star using a gravity-darkened Roche spheroid in solid-body rotation with a point mass gravitational potential, which induces a temperature gradient ($T_{eff}(\theta) \propto g_{eff}^{0.25}(\theta)$ where $\theta$ is co-latitude) over the surface (von Zeipel, 1924). Since intermediate mass stars have radiative envelopes and relatively small convective cores, solid-body rotation can be a good approximation for the external layers of early-type stars (Spiegel & Zahn, 1992; Reiners & Royer, 2004).

Roche modeling for isolated rotating early-type stars is described in Chapter 2, but a brief description is useful here. This Roche model requires six

parameters to describe the star, including the inclination angle, $i$, the position angle, P.A., surface gravity at pole, $g_p$ (or, equivalently mass, $M$), polar angular diameter, $\theta_p$ (or equivalently the radius, $R$, through the parallax, $p$), polar effective temperature, $T_{eff,p}$, and the fractional angular velocity, $\omega$ ($= \Omega/\Omega_B$ where $\Omega_B$ is the angular velocity at break-up). As noted in Chapter 2, we can calculate the effective surface gravity, $g_{eff}(\theta)$ at a given stellar latitude from Equation (2.2), and in turn, $T_{eff}(\theta)$ by gravity darkening law above. With these parameters we calculated the specific intensity over the surface assuming that LTE, hydrostatic equilibrium, and plane-parallel atmospheres apply locally.

One more model parameter, macroturbulent velocity, $V_{Mac}$, was added to complete the specification of our model. As already described in § 2.4, we consider here only isotropic macroturbulence and horizontal macroturbulence for broadening of spectral lines. The details of obtaining macroturbulence-broadened lines for fitting are described in § 6.4.4.

## 6.4 Computations

To determine the parameters of the Roche model several observables are calculated here. These include the absolute flux over the visible/red spectrum and the hydrogen Balmer line profiles, which constrain $T_p$ and $g_p$, the spectral line profiles of the Ca I and Mg I lines to obtain $v \sin i$ and $V_{Mac}$, and the NPOI closure phases which are sensitive to the fractional angular rotational velocity, inclination angle, position angle, and angular diameter.

The model parameters are fitted by minimizing the $\chi^2$ metric utilizing the Levenberg-Marquardt (LM) algorithm (Press et al., 1992), which is an iterative technique that locates the minimum of a multivariate non-linear function. Details of the theoretical calculations of the spectroscopic and interferometric observables for the fitting, follow.

### 6.4.1 Spectral Synthesis Method

As described in § 5.3, the synthetic spectrum was calculated by integrating the emergent flux over the apparent stellar disk. The emergent flux was obtained by the following steps. The flattened disk is constructed inside a square $256 \times 256$ grid. The stellar parameters were obtained at the center of each pixel containing part of the flattened disk and the specific intensity in each cell as a function of $\lambda$ was computed along with the projected velocity. ATLAS12 (Kurucz, 2005) models were used which provide specific intensities tabulated

at 17 values of $\mu$, which Kurucz (2007, private communication) provided using the deduced abundances in Table 5.2 and -0.6 dex down from solar values for other elements. We note that the abundance of nitrogen was also down by -0.41 dex from solar instead of the values are finally settled on but this should not change models except for a change in the mean molecular weight. The atomic line data were taken from the extensive compilation of Kurucz & Bell (1995). We adopted $2\,\mathrm{km\,s^{-1}}$ for the microturbulence as described in Chapter 5. The intensities provided by ATLAS12 models are different by 0.5% from those of ATLAS9 models.

### 6.4.2 Spectral Energy Distribution

Based on the synthetic spectra described above, the spectral energy distribution was calculated in the spectral bands of the subset of measured fluxes we have selected from the Hayes (1985) compilation. Boxcar averages of the fluxes over 25 Å wide segments centered on the wavelengths were computed. Here the Doppler shift due to projected rotational velocity at each cell is not considered because of the low resolution. This theoretical spectral energy distribution is compared with the observed spectrophotometric data (Hayes, 1985) as described in § 6.2.

### 6.4.3 Hydrogen Balmer Lines $H_\alpha$, $H_\beta$, and $H_\gamma$

The hydrogen Balmer lines provide us a direct mass estimate through their sensitivity to the surface gravity. We adopt the same procedure used in reducing the observed $H_\alpha$, $H_\beta$, and $H_\gamma$ profiles (Peterson, 1969) in calculating the synthetic profiles. That is, we limited our calculations to 160 Å segments centered on the lines and chose the regions at 70 Å from the line center to define the continuum. In this case the Doppler smearing due to rotation is included. Emergent fluxes at the symmetric wavelengths on both sides of the line centers were averaged to produce the predicted line profiles. For $H_\alpha$, the flux for the observed point nearest the line core is excluded because the sampling of the line core is too coarse to predict the rotational smearing effect accurately.

### 6.4.4 Spectral Lines: Ca I $\lambda$ 6161 and Mg I $\lambda$ 4702

The lines of Ca I $\lambda\,6162$ and Mg I $\lambda\,4702$ were synthesized with a sampling of $\lambda/\Delta\lambda = 500,000$ then convolved down to R = 42,000, which is the ELODIE spectrograph resolution. At projected velocities near 20 $\mathrm{km\,s^{-1}}$, Doppler smearing clearly dominates these line profiles.

There are two complications in fitting these spectral lines. First, it is necessary to additionally broaden the synthetic lines allowing for the effects of macroturbulent velocity as noted in § 5.4.2, unlike the cases of the continuum fluxes for the absolute calibration or the hydrogen line profiles. Macroturbulent broadening was introduced at every iteration of the fitting process by linearly interpolating among spectra calculated at 5 different resolutions: R = 20,000, 25,000, 30,000, 38,000, and 42,000.

The other difficulty is to match the line strengths of the synthetic lines to that of the observed lines. Rotation affects equivalent widths of the lines (refer to § 5.4.3) and thus the strengths of the computed lines must be adjusted (i. e., a new abundance estimated) on each iteration of the fitting. For this purpose, Ca I $\lambda$ 6162, as a weak line on the linear part of a curve of growth can be fitted more easily than an intermediate strength line, such as Mg I $\lambda$ 4702. The residual flux of a weak line can be adjusted to match the observed line by scaling the line depth with the ratio of the equivalent width of the synthetic line to that of the observed line. The scaled residual flux, $R'_\lambda$ is given by,

$$R'_\lambda = 1 - \frac{W_{synthetic}}{W_{observed}}(1 - R_\lambda) \tag{6.1}$$

where $R_\lambda$ is the residual flux calculated at given parameters before scaling and $W_{synthetic}$ and $W_{observed}$ are the equivalent widths of the synthetic line and the observed line respectively.

Mg I needs to be treated more carefully. Four spectra at different abundances (at least one less abundant and at least one more abundant than the required) are produced. A chi-squared quantity is then calculated by comparing the observed and synthetic fluxes produced for the different abundances. By parabolic interpolation we obtained the $\chi^2$ minimum and in turn, the corresponding abundance. We then calculated the spectrum by simple linear interpolation.

### 6.4.5 Complex Visibility Calculation

The interferometric observables, an amplitude and a phase of the complex visibility can be calculated as a Fourier transform of the "strip brightness distribution" which is calculated by integrating intensity perpendicular to the baseline (Born & Wolf, 1999). The intensities are also computed using the detailed limb angle dependence provided by the ATLAS12 model atmospheres(Kurucz, 2005). Here we use only the closure phase data as described in Peterson et al. (2006a). For details of fitting Roche models to the NPOI data see Peterson et al. (2006a).

## 6.5 Discussion

### 6.5.1 Model Fitting

Because of the concern that line widths might not be reliable indicators of actual projected velocity due to the substantial broadening caused by macroturbulence (5.4.2) we removed $v \sin i$ as a constraint in the fitting process.

As shown in Table 6.1, the best fitting model parameters are $\omega = 0.876 \pm 0.006$, $\theta_p = 2.833 \pm 0.008$ mas, $T_p = 10059 \pm 13$ K, $i = 4.975° \pm 0.081$, PA $= 11.41° \pm 2.08$, M $= 2.135 \pm 0.075\,\mathrm{M}_\odot$, and $\mathrm{V}_{Mac} = 7.65 \pm 0.45$ km s$^{-1}$ based on closure phase, spectrophotometric data, hydrogen line profiles ($\mathrm{H}_\alpha$, $\mathrm{H}_\beta$, and $\mathrm{H}_\gamma$), and metal line profiles (Ca I $\lambda$ 6162 and Mg I $\lambda$ 4702) which was obtained with the isotropic macroturbulence model. The derived parameters are also shown in Table 6.1. The correlation matrix for this case is given in Table 6.2.

Both macroturbulence models match the line profiles well. The plots of the (best fitting) isotropic macroturbulence model for the continuum flux, Balmer lines, spectral lines, and closure phases are shown in Figures 6.1, 6.2, 6.3, 6.4, 6.5, 6.6, and 6.7 respectively. The fits based on the horizontal macroturbulence yields very similar model parameters and line profiles compared to isotropic macroturbulence, and we show only the latter. One sees excellent fits of the theory to the observations, as evidenced by both the plots and $\chi^2$, given in Table 6.3, where we also tabulate how much each type of data contributes to the $\chi^2$.

### 6.5.2 Fitting Strong Lines

In the process of selecting lines to include in the final fitting we also considered lines with higher excitation/ionization energies, lines which are contributed more from the hotter polar regions. As with the low excitation lines practical considerations lead to selecting an Fe II line (4522 Å) and an O I triplet (6155 Å) for analysis. Both these lines are significantly stronger than the low excitation lines described earlier.

We adopted the same two macroturbulence models; isotropic and horizontal macroturbulence. Both models gave bad fits to the profiles with the isotropic model being slightly preferred. There was a clear conflict when attempting to simultaneously fit the weak and strong lines. The weak lines tend to require a higher temperature and faster rotation while the strong lines tend to be cooler and slower ($\omega \sim 0.84$). Because they should be less dependent on any inadequacies in the model atmospheres we decided to use only the weak Ca I line and the intermediate strength Mg I line in the final fits. The

reasons for the inconsistency between the two sets of lines are not clear at present. One possibility could be that the assumption of solid-body rotation might need to be relaxed. However we do not know what kind of figure the differential rotation would produce so we leave this as an intriguing issue to be resolved in the future.

### 6.5.3 Comparisons with Previous Studies

It is not straightforward to compare our results with those previously reported since the individual studies used different data sets (ELODIE, OAO, DAO and so on) and techniques (interferometry or spectroscopy). For example, the CHARA study (Aufdenberg et al., 2006) used visibility amplitude data and spectrophotometric fitting including UV and IR but did not fit the Balmer lines (instead simply adopting a mass, $M = 2.3\,M_{\odot}$ and a projected velocity). The NPOI interferometry (Peterson et al., 2006b) used only closure phase data with V magnitude and $v_{eq} \sin i$ constraints. In the most recent discussion by Hill, Gulliver, & Adelman (2004), the rotation parameter, $\omega$, was incorrectly calculated, as reported in Aufdenberg et al. (2006). Interestingly, another recent spectroscopic study (Takeda, Kawanomoto, & Ohishi, 2008) supports the parameters reported by Hill, Gulliver, & Adelman (2004).

However, some qualitative comparisons can be made. The situation is summarized in Table 6.5. The spectroscopic studies show significantly slower rotation than found here. We focus on the results by Takeda, Kawanomoto, & Ohishi (2008) as typical of the spectroscopic studies. As already noted (§ 5.4.2) they did not consider the possibility of macroturbulence. As a result, their deduced parameters are at odds with those based on interferometry, leading them (Takeda, Kawanomoto, & Ohishi, 2008) to suggest that Aufdenberg et al. (2006) in particular had accepted a false $\chi^2$ minimum. These lead us to wonder if we could reproduce the Takeda, Kawanomoto, & Ohishi (2008) results and if so, whether our fitting procedure, starting with the parameters given there, would nevertheless converge to the parameters we report here. For this purpose, the interferometric closure phase data and Balmer line profiles were removed and the constraints of $v_{eq} \sin i = 22\,\mathrm{km\,s^{-1}}$ and a mass of $2.3 M_{\odot}$ were added. The results are shown in Table 6.4. The resulting parameters are somewhat different from Takeda, Kawanomoto, & Ohishi (2008)'s results. Our result ($\omega \sim 0.75$) for the rotation rate somewhat higher than theirs ($\omega \sim 0.6$) and other parameters are correspondingly different. However, we should note that Takeda, Kawanomoto, & Ohishi (2008) used many weak lines but we used two lines and one of the lines is the intermediate strength line. Further, Takeda, Kawanomoto, & Ohishi (2008) made no effort to implement an optimization

procedure.

We next consider what the fitting algorithm yields when the interferometry coupled with the absolute spectrophotometry and the Balmer lines we modeled are added back, but we use the Takeda-like parameters found above and mass parameter of 2.3 $M_\odot$ (starting with a variety of position angles) as initial guesses for the parameters. From this procedure, we confirm that starting from Takeda-like parameters converges to our results (different by 0.07 in total $\chi^2$). We conclude that while we cannot speak to the results reported by Aufdenberg et al. (2006), there appear to be no issues with false $\chi^2$ minimums here nor in the results reported by Peterson et al. (2006b).

### 6.5.4 Abundance Changes

The parameter values for Vega obtained here are significantly different than those adopted for the abundance determination in Chapter 5 (Peterson et al., 2006b). Based on the new model, we reexamined the abundances of several chemical elements determined earlier. As expected, the elements which have moderately high excitation/ionization energies such as C I, and O I show almost no change in abundance (<= 0.05 dex). The abundance of Mg I an intermediate excitation energy element, increases by 0.1 dex. However, He I tends to show a slight decrease in abundance (0.065) but it is still nearly solar. Surprisingly, the Fe II abundance increases by 0.2 dex. These changes do not affect our conclusion in the last chapter that Vega is a mild $\lambda$ Boo star.

### 6.5.5 Updating Metallicity, Mass, and Age

As we already mentioned in Chapter 5, the previously assumed Vega's mass and age (e. g., Peterson et al., 2006b) were estimated by assuming the solar metallicity. However, the argument that Vega is well mixed due to its fast rotation leads to mass and age estimates of M = 2.09 $M_\odot$ and 536 Myr using metallicity (Z = 0.0093) from the surface composition.

The direct estimate of Vega's mass ($2.135 \pm 0.075$ $M_\odot$) obtained here using surface gravity (Balmer lines) and polar radius is consistent with the mass based on the abundance. This direct mass is much lower by $\sim 4\sigma$ than the mass of 2.40 $M_\odot$ that would be obtained assuming solar metallicity, but retaining the luminosity and polar radius derived here. Interestingly, given the luminosity, polar radius, and mass, we can estimate the metallicity and age using BASTI evolutionary grids[1]. For an $\alpha$-enhanced mixture, we obtain Z=0.0080±0.0033

[1] `http://www.te.astro.it/BASTI/index.php`

and 471±57 Myr for metallicity and age, completely consistent with Z∼0.0093 which we derived for the surface composition and significantly smaller than solar metallicity (Z = 0.020).

We conclude that Vega's bulk metallicity is consistent with its surface composition and in particular is significantly less than solar.

### 6.5.6 Optimal Mass and Age Estimates

While it is clearly important to estimate Vega's mass, composition, and age with as few assumptions as possible, this necessarly leads to rather larger estimated errors. If, instead, we assume Vega is chemically homogeneous, much more precise estimates of mass and age may be obtained from the location of its radius and luminosity in the evolutionary grids. The metallicity and mass based on the revised chemical composition are $0.0090 \pm 0.0006$ and $2.157 \pm 0.017\,M_{\odot}$ respectively. This in turn suggests an age of $454 \pm 13$ Myr, continuing the difficulty of identifying Vega as a member of the Castor moving group as we described in § 5.5.4.

For comparison (and convenience) we tabulate our various estimates of Vega's mass depending on estimating methods and metallicity in Table 6.6. The first two results (Peterson et al., 2006b; Yoon et al., 2008) are derived by adopting the model parameters based on NPOI interferometry where Peterson et al. (2006b) estimated mass by locating Vega on interior models (Girardi et al., 2000) of solar metallicity while Yoon et al. (2008) estimated mass based on the deduced surface abundance. As described here, the last two entries are based on the best fit parameters using both spectroscopy and interferometry but the mass in the third line was calculated directly using surface gravity and polar radius while the last mass was obtained by the updated chemical abundance reported in § 6.5.4.

The primary conclusions of this section are that Vega is substantially less massive and correspondingly older than previously assumed, and that its unusual composition appears to hold throughout its bulk.

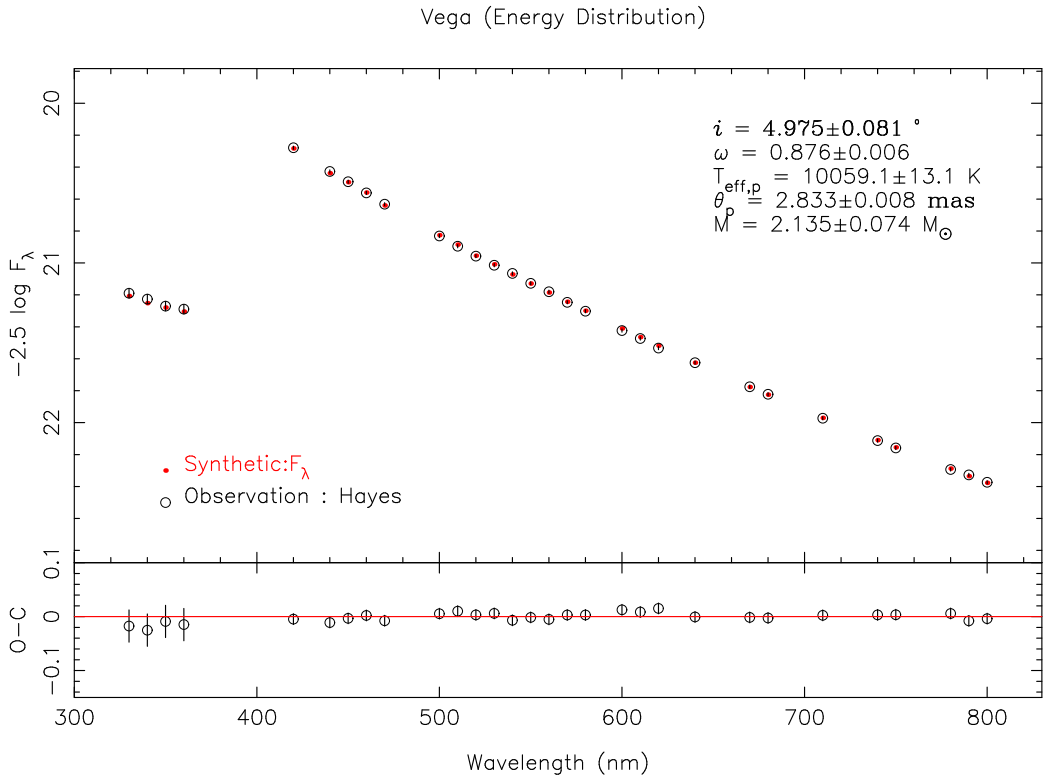


Figure 6.1 Shown is the energy distribution in the visual/red. The open circles represent the data points (magnitude) taken by Hayes (1985) and the error bars are also shown. We took 1 % error in the visual and 3 % error for the UV. The red dots represent the theoretical values. The theory, using the isotropic macroturbulence case parameters, fits the observation reasonably well. Residuals from the fit are shown below. Note the scale change for the residuals.

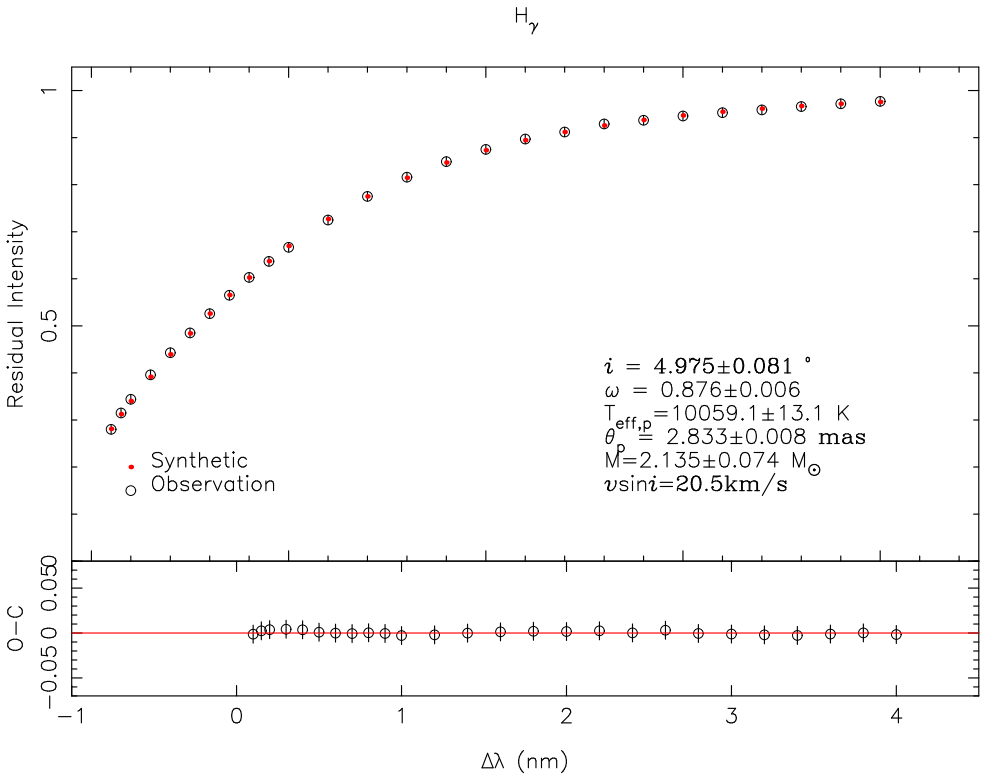


Figure 6.2 The $H_\gamma$ line fit using the model parameters for the isotropic macroturbulence case. Symbols are as in Figure 6.1. The abscissa, $\Delta\lambda = \lambda - \lambda_c$ is the distance from the line center ($\lambda_c$). The observational data of hydrogen Balmer lines and errors (0.01) are taken from Peterson (1969). The hydrogen Balmer lines constrain the temperature but mostly the surface gravity, allowing a direct estimate of mass.

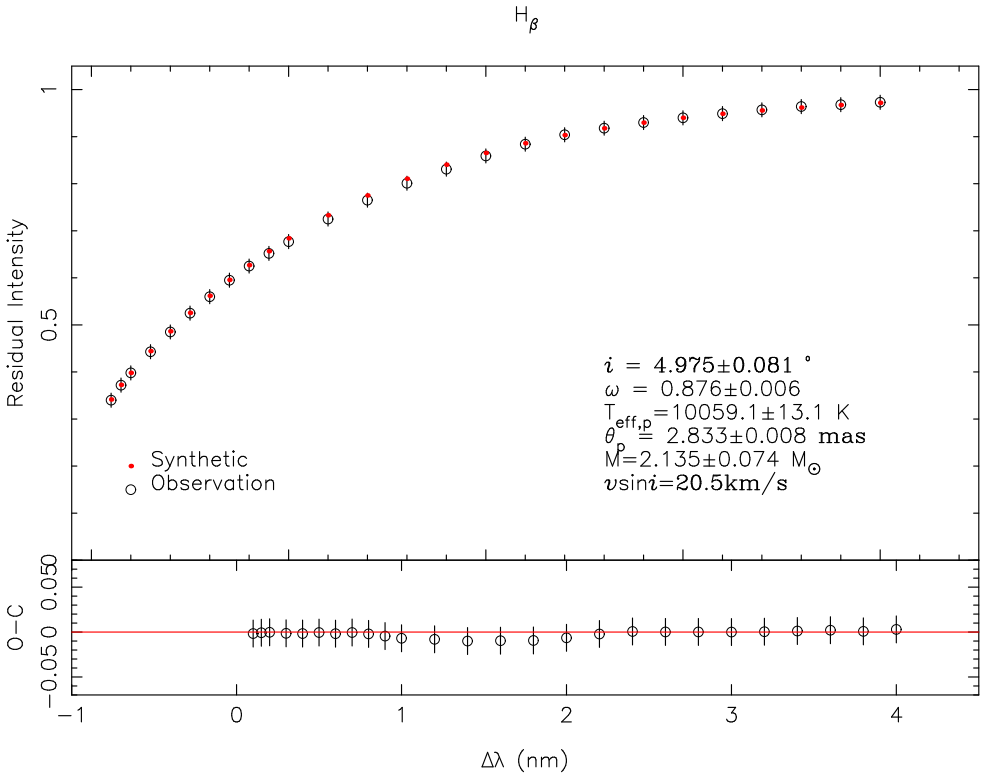


Figure 6.3 The $H_\beta$ line profile plotted as in Figure 6.2. The observational error was estimated to be 0.015 in residual intensity.

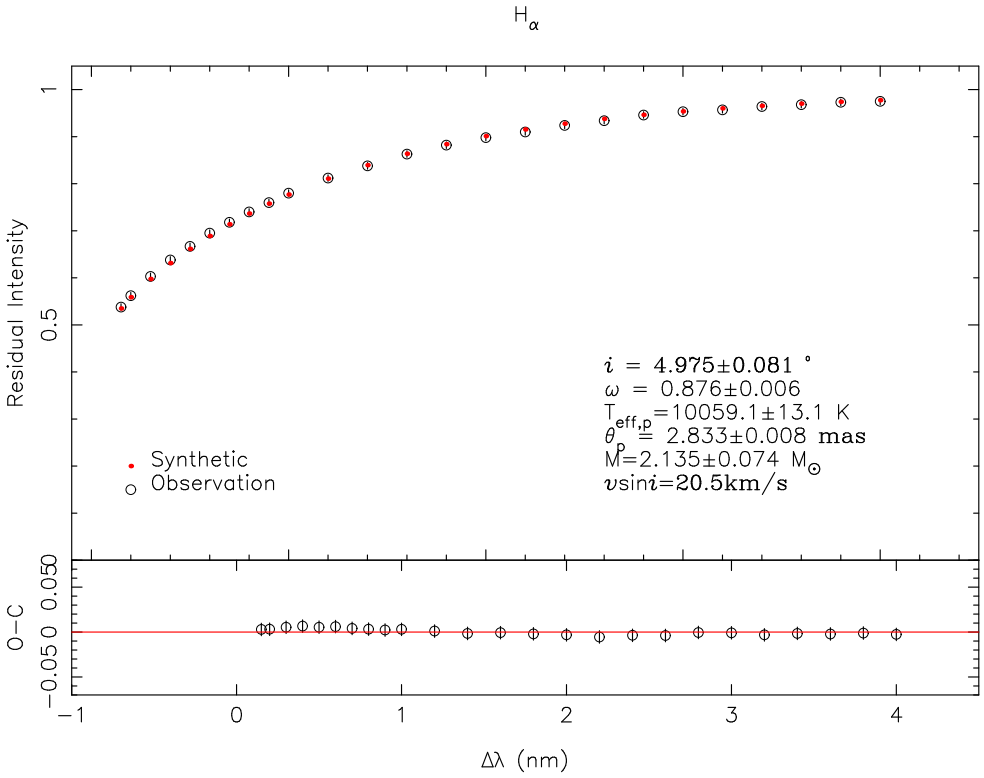


Figure 6.4 The $H_\alpha$ line profile, plotted as in Figure 6.2. Errors here were estimated to be 0.007 in residual intensity.

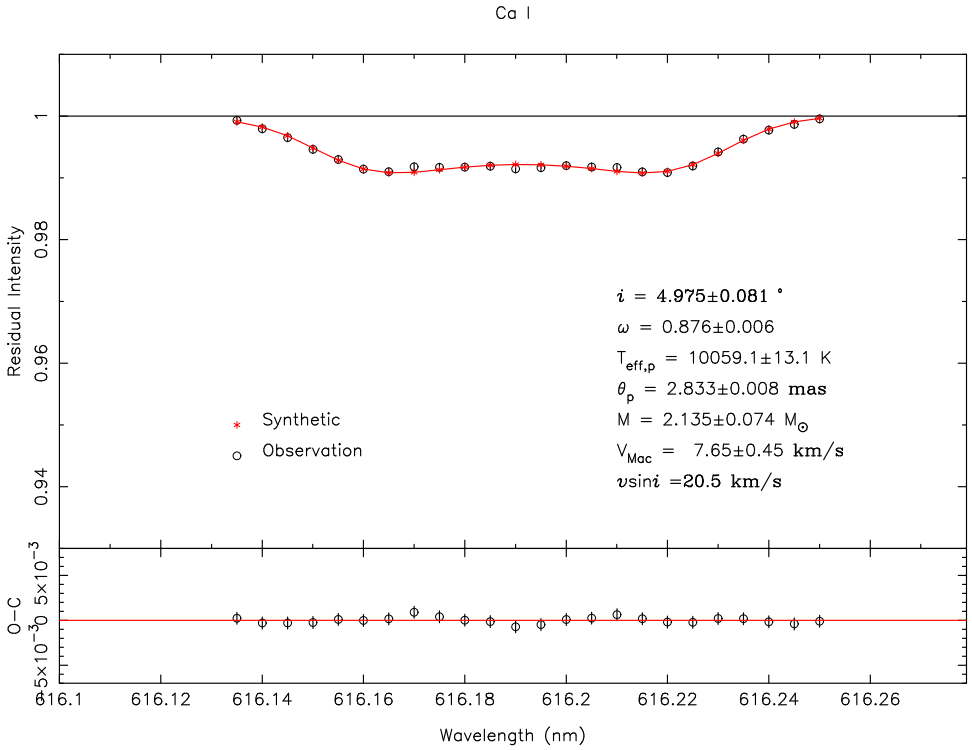


Figure 6.5 Shown is the line profile fit to a weak Ca I line ($\lambda$6162). The synthetic spectrum fits the observed profile very well. This self-reversed shape of this low excitation line constrains the macroturbulent velocity.

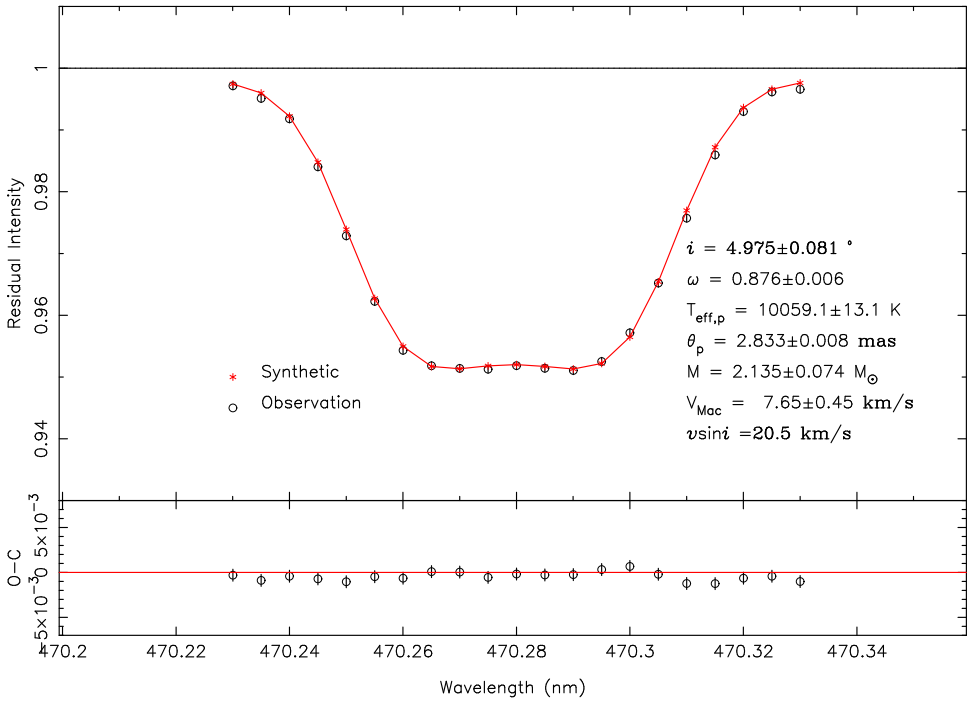


Figure 6.6 A model fit to an intermediate strength line profile of Mg I ($\lambda\,4702$). This fit, which is very good, is consistent with that for the weak Ca I ($\lambda\,6162$) line.

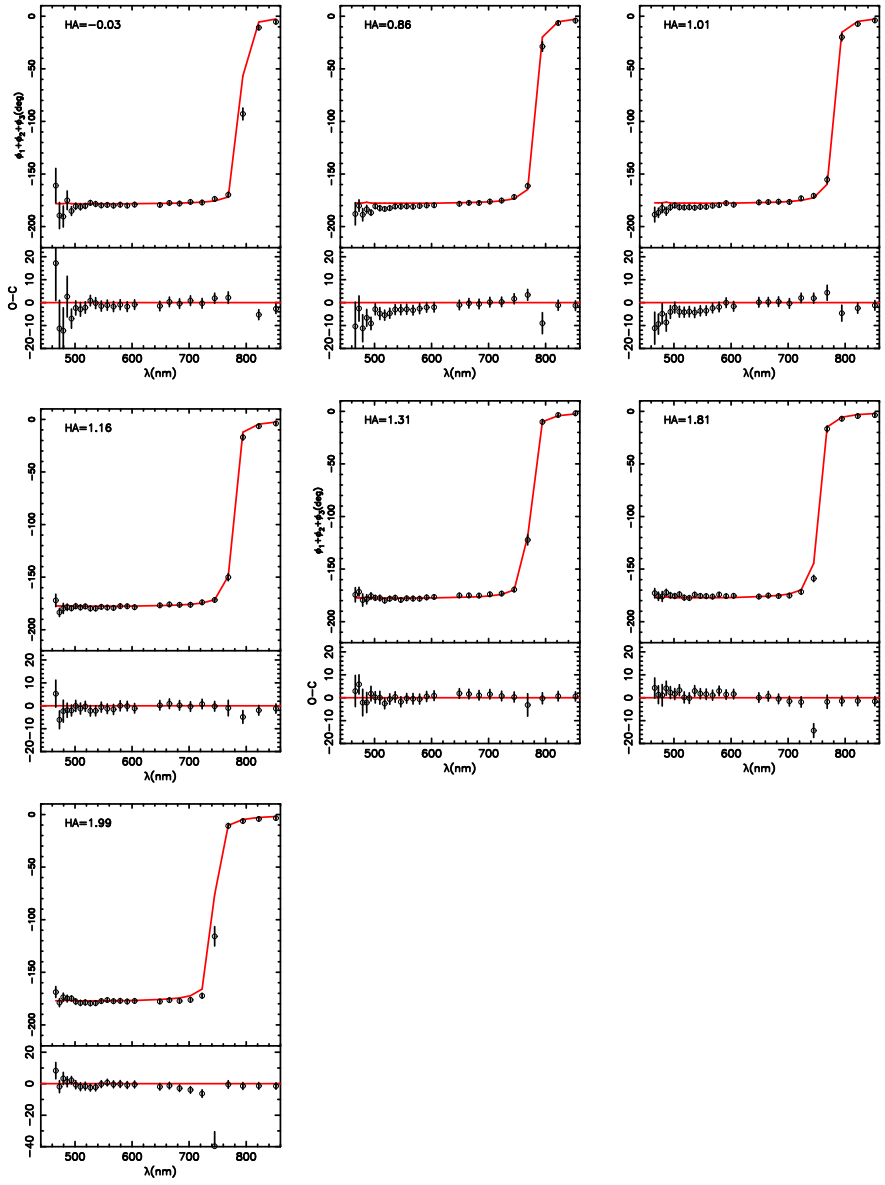


Figure 6.7 The NPOI observations (open circles) of closure phase, estimated error bars, and the model calculations (red solid lines) are plotted for each scan (labeled by hour angle). Residuals are shown directly below each of the scans. If an object is centro-symmetric, the closure phases take on only 0 °or 180 °(called as "top-hat" behavior). Significant departures from this simple top-hat behavior provide the detection of asymmetry in surface intensity distribution. The phases measured here clearly indicate Vega's intensity distribution is asymmetric. These data constrain the rotation rate, inclination angle, position angle, and angular diameter of Vega.

Table 6.1. The best fit parameters for Vega

| Quantity | Isotropic $V_{Mac}$[a] | Horizontal $V_{Mac}$[a] |
|---|---|---|
| Model parameters | | |
| $\omega = \Omega/\Omega_B$ | 0.876 ± 0.006 | 0.871 ± 0.004 |
| $\theta_p$ (mas) | 2.833 ± 0.008 | 2.840 ± 0.005 |
| $T_p$ (K) | 10059 ± 13 | 10050 ± 10 |
| $i$ (°) | 4.975 ± 0.081 | 5.066 ± 0.077 |
| PA (°) | 11.41 ± 2.08 | 11.27 ± 2.04 |
| M ($M_\odot$) | 2.135 ± 0.075 | 2.165 ± 0.075 |
| $V_{Mac}$ ( $\mathrm{km\,s^{-1}}$ ) | 7.65 ± 0.45 | 8.75 ± 0.56 |
| Derived parameters | | |
| $v_{eq}$ ( $\mathrm{km\,s^{-1}}$ ) | 236.19 ± 3.65 | 235.52 ± 3.52 |
| $v_{eq,B}$ ( $\mathrm{km\,s^{-1}}$ ) | 338.99 ± 5.62 | 340.98 ± 5.78 |
| $v_{eq} \sin i$ ( $\mathrm{km\,s^{-1}}$ ) | 20.48 ± 0.11 | 20.80 ± 0.11 |
| $\Omega(d^{-1})$ | 1.652 ± 0.023 | 1.653 ± 0.026 |
| $\Omega_B(d^{-1})$ | 1.891 ± 0.032 | 1.898 ± 0.033 |
| $T_{eq}(K)$ | 8152± 42 | 8184 ± 27 |
| $R_p$ ($R_\odot$) | 2.362± 0.012 | 2.367 ± 0.011 |
| $R_{eq}$ ($R_\odot$) | 2.818± 0.013 | 2.815 ± 0.012 |
| $\theta_{min}$ (mas) | 3.375± 0.005 | 3.372 ± 0.003 |
| $\theta_{max}$ (mas) | 3.380± 0.005 | 3.377 ± 0.003 |
| logL ($L_\odot$) | 1.603± 0.005 | 1.606 ± 0.004 |
| $\log g_p$ ($\mathrm{cm^2 s^{-2}}$) | 4.021± 0.014 | 4.024 ± 0.015 |
| $\log g_{eq}$ ($\mathrm{cm^2 s^{-2}}$) | 3.655± 0.021 | 3.668 ± 0.018 |
| Age (Myr) | 471.3± 57.3 | 448.6 ± 57.4 |
| Z | 0.0080± 0.0033 | 0.0093 ± 0.0033 |
| Number of data | 334 | 334 |
| $\chi^2$ | 223.89 | 224.64 |

[a]The parallax error is propagated in error estimates.

Table 6.2 The correlation matrix for the isotropic macroturbulence case

| Correl.[a] | $i$ | $\omega$ | $\theta_p$ | PA | $T_p$ | M | $V_{Mac}$ |
|---|---|---|---|---|---|---|---|
| $i$ | 1.0000 | -0.3032 | 0.3297 | -0.2205 | -0.5506 | -0.6283 | -0.1075 |
| $\omega$ | -0.3032 | 1.0000 | -0.9932 | -0.3141 | 0.8461 | -0.5015 | 0.1400 |
| $\theta_p$ | 0.3297 | -0.9932 | 1.0000 | 0.3268 | -0.8682 | 0.4746 | -0.1345 |
| PA | -0.2205 | -0.3141 | 0.3268 | 1.0000 | -0.1769 | 0.4300 | -0.0152 |
| $T_p$ | -0.5506 | 0.8461 | -0.8682 | -0.1769 | 1.0000 | -0.1752 | 0.0779 |
| M | -0.6283 | -0.5015 | 0.4746 | 0.4300 | -0.1752 | 1.0000 | -0.0986 |
| $V_{Mac}$ | -0.1075 | 0.1400 | -0.1345 | -0.0152 | 0.0779 | -0.0986 | 1.0000 |

[a]Correlation

Table 6.3 Individual $\chi^2$'s for the isotropic macroturbulence case

| Data | N.Obs.[a] | $\chi^2$ | References |
|---|---|---|---|
| Abs.Cal.[b] | 30 | 12.44 | Hayes (1985) |
| $H_\gamma$ | 26 | 1.05 | Peterson (1969) |
| $H_\beta$ | 26 | 2.13 | Peterson (1969) |
| $H_\alpha$ | 25 | 6.15 | Peterson (1969) |
| Ca I $\lambda$ 6162 | 24 | 5.15 | ELODIE |
| Mg I $\lambda$ 4702 | 21 | 5.98 | ELODIE |
| Triple phase | 182 | 191.00 | Peterson et al. (2006b) |
| Total | 334 | 223.89 | $\cdots$ |

[a]Number of observed data points

[b]Absolute calibration

Table 6.4 Takeda-like model parameters: Roche model fit parameters of our attempt to reproduce the Takeda, Kawanomoto, & Ohishi (2008) results

| | $i$ | $\omega$ | $\theta_p$ | $T_p$ |
|---|---|---|---|---|
| Value | 6.577 | 0.7452 | 3.032 | 9748 |
| $\sigma$ | 0.086 | 0.0055 | 0.008 | 11 |

Note. — The number of data points is 76 and the $\chi^2$ is 47.68.

Table 6.5 Comparison of this work with previous results

| Parameter | P2006[a] | A2006[b] | TKO2008[c] | This Work |
|---|---|---|---|---|
| $\omega = \Omega/\Omega_B$ | 0.926 ± 0.021 | 0.91 ± 0.03 | ··· | 0.876 ±0.006 |
| $R_p$ ($R_\odot$) | 2.306 ± 0.031 | 2.26 ± 0.07 | $2.52^{+0.05}_{-0.07}$ | 2.362 ± 0.012 |
| $T_p$ (K) | 9988 ± 61 | 10150 ± 100 | $9867^{+86}_{-79}$ | 10059 ± 13 |
| $i$ (°) | 4.54 ± 0.33 | 4.7 ±0.3 | $7.2^{+1.7}_{-1.2}$ | 4.975 ± 0.081 |
| $v_{eq}$ ( $\mathrm{km\,s^{-1}}$ ) | 274 ± 14 | 270 ± 15 | 175 ± 33 | 235.5 ± 3.5 |
| M ($M_\odot$) | 2.303 ± 0.024 | 2.3 ± 0.2 | 2.3 | 2.135 ± 0.075 |

[a]Peterson et al. (2006b)

[b]Aufdenberg et al. (2006)

[c]Takeda, Kawanomoto, & Ohishi (2008)

Table 6.6 Summary of mass and age estimates depending on the method used

| Reference | Z | Mass ($M_\odot$) | Age (Myr) | Method |
|---|---|---|---|---|
| P2006[a] | 0.019 | $2.303 \pm 0.024$ | $386 \pm 16$ | Interior Model |
| Y2008[b] | 0.0093 | $2.09 \pm 0.03$ | $536 \pm 29$ | Composition |
| This work | 0.0080 | $2.135 \pm 0.075$ | $471 \pm 57$ | Balmer Lines |
| | 0.0090 | $2.157 \pm 0.017$ | $454 \pm 13$ | Composition |

[a]Peterson et al. (2006b)

[b]Yoon et al. (2008)

# Chapter 7

# Closing Remark

Rotation obscures our interpretation of stellar physical properties and we do not know the actual rotation rate of individual stars at all well. Recent developments in high resolution spectroscopy and high angular resolution interferometry have substantially improved the prospects for studying the effects of stellar rotation on evolution.

In this dissertation, we have characterized the effect of rotation on A and F stars as ground-based interferometry calibrators and produced a list of potential targets for the NPOI observations so that will allow us a statistical study of stellar rotation and evolution. We have confirmed that Vega is a mild $\lambda$ Boo star based on the abundance analysis which allows for the fact that Vega is a rapid rotating star seen almost pole-on, through a simultaneous analysis of NPOI interferometric data and spectroscopy using ELODIE archive data. Because of the high rotation rate we have argued that Vega is probably well mixed because of its rapid rotation and thus its peculiar chemical abundance is not limited to the surface, that it is metal-poor throughout. By locating Vega on low-metallicity BASTI evolutionary tracks, we have deduced the new estimates of Vega's mass and age and concluded that Vega is older and less massive than the currently assumed, thus arguing against its membership of the Castor moving group. In addition, by incorporating metal profiles and Balmer line profiles, imposing the absolute calibration in the visible and using the most recent ATLAS12 models especially calculated for this project, we have determined the mass directly using surface gravity and polar radius, confirming that it is consistent with that derived above (deduced mass using chemical composition) and significantly less than expected for a solar composition. This confirmation represents a significant challenge to our current understanding of the star formation process.

## 7.1 Future Work

From this point there is much to do. The simultaneous reduction will be further improved through the addition of the CHARA data of Vega which will give more constraints on the fits thus more reliable estimates of the physical parameters such as angular rotation rate, angular diameter, position angle, and inclination angle. This work is well advanced toward publication.

Secondly, these techniques are applicable to the other potential targets. The obvious next target is Altair because interferometric data (the NPOI and the CHARA observations) and spectroscopic data (ELODIE) are already in hand. Altair has always been known to be a rapidly rotating star because its projected velocity is high ($245\,\mathrm{km\,s^{-1}}$). However, the high projected velocity makes the problem difficult because it causes severe blending in its spectrum. Only with a complete spectral synthesis can one model these effects.

Besides Vega and Altair, there are many other targets to be investigated for oblateness and asymmetry in the northern hemisphere as already discussed in Chapter 4. Especially, $\alpha$ Cep and $\beta$ Cas are the available stars for very near future investigations because they show detection probabilities of 92% and 60% with the NPOI 80 m baseline for asymmetry respectively.

Next, the study of rotating stars in southern hemisphere should be also done. The targets in southern hemisphere can be observed with the AMBER, the near-infrared focal instrument of the VLTI which is unique for southern hemisphere. It is able to measure visibility amplitude and triple phase and has long enough baselines to begin to effectively resolve a few A and F stars. We have simulated the capabilities of AMBER on all potential targets south of $+15^\circ$ on the currently offered triple phase configuration, A0-G1-K0 at $1.25\,\mu$m. Six targets (HR 591, 1666, 2550, 3685, 6380, and 8728) appear to have detectable oblateness. However, none of the targets will have measurable triple phase according to the simulations, with this baseline combination. Although the measurement of visibility amplitudes beyond the first zero in the Airy disk will indicate the angular rotation rate, combining this with line widths will not automatically lead to good values of the inclination according to our Vega investigation. If the VLTI implements the longest baseline of 202 m, then a triangle such as B5-J6-M0, we could detect triple phases for asymmetry in 4 or 5 objects such as $\alpha$ Eri, $\alpha$ Hyi, $\beta$ Car, $\eta$ Sco, and $\epsilon$ Sqr as well as increasing the number of targets with detectable oblateness. The VLTI is already implementing differential phase techniques and that will also increase the number of likely asymmetry detections.

Lastly, we note that HR 8576 (Holweger et al., 1986), an A0 star shows the kinds of line shapes we have investigated from Vega's spectrum. We consider

this object is a likely rapid rotator seen pole-on. An observation with the ANDICAM[1] instrument of the Small and Moderate Aperture Research Telescope System (SMARTS)[2] was already done and we are able to begin analysis of its rotational nature.

In addition to continuing these observational studies, we hope to assist with the developments of stellar rotation theory to include the effects of differential rotation because there are still many inconsistencies between the theory and observations to be resolved. Although such interior models are being calculated, they are not yet down at $2M_{\odot}$. These theoretical developments could be immediately challenged by using lines from different parts of the surface allowing us to map out rotation over the surface. In addition, stellar interior models should be also studied to support the argument of interior mixing due to rapid rotation. Through these theoretical approaches as well as the observational studies we have described, we can hope to reveal more about these star's true natures.

[1] `http://www.astronomy.ohio-state.edu`
[2] `http://www.astro.yale.edu/smarts`

# Bibliography


Abt, Helmut A., & Levy, Saul G. 1974, ApJ, 188, 291

Adelman, S. J., & Gulliver, A. F. 1990, ApJ, 348, 712

Allende Prieto, C., et al. 1999, ApJ, 527, 879

Armstrong, J. T., et al. 1998, ApJ, 496, 550

Aufdenberg, J. P., Ludwig, H. -G., & Kervella, P. 2005, ApJ, 633, 424

Aufdenberg, J. P., et al. 2006, ApJ, 645, 664

Barnes, T. G., Evans, D. S., & Moffet, T. J. 1978, MNRAS, 184, 285

Barrado y Navascués, D. 1998, A&A, 339, 831

Baschek, B., & Slettebak, A. 1988, A&A, 207, 112

Baschek, B. 1992, in The Atmospheres of Early-Type Stars, ed. U. Heber & C. S. Jeffery (Berlin: Springer), 224

Boden, A. F., Creech-Eakman, M. J., & Queloz, D. 2000, ApJ, 536, 880

Boden, A. F., & Lane, B. F. 2001, ApJ, 547, 1071

Bordé, P., et al. 2002, A&A, 393, 183

Born, M., & Wolf, E. 1999, Principles of Optics (7th ed.; Cambridge: Cambridge Univ. Press)

Bracewell, R. 1965, The Fourier Transform and Its Applications (New York: McGraw-Hill)

Carney, B. W. 1996, PASP, 108, 900

Carroll, B. W., & Ostlie, D. A. 2007, An Introduction to Modern Astrophysics (2nd ed.; Pearson Addison-Wesley)

Castelli, F., & Faraggiana, R. 1979, A&A, 79,174

Castelli, F., & Kurucz, R. L. 2003, in IAU Symp. 210, Modeling of Stellar Atmospheres, ed. N. E. Piskunov., W. W. Weiss, & D. F. Gray (San Francisco: ASP), A20 CD-ROM (astro-ph/040587)

Charbonneau, P. 1993, IAU Colloq. 138, Peculiar versus Normal Phenomena in A-type and Related Stars, ed. M. M. Dworetsky, F. Castelli, & R. Faraggiana (San Francisco: ASP), 474

Ciardi, D. R., et al. 2001, ApJ, 559, 1147

Claret, A. 2004, A&A, 424, 919

Colavita, M. M. 1999, PASP, 111, 111

Collins, G. W., II 1963, ApJ, 138, 1134 (erratum, 139, 1401[1964])

Collins, G. W., II 1970, in Stellar Rotation, ed. A. Slettebak (New York: Gordon and Breach), 85

Deutsch, A. J. 1970, in Stellar Rotation, ed. A. Slettebak (New York: Gordon and Breach), 207

Díaz-Cordovés, J., & Giménez, A. 1992, A&A, 259, 227

Domiciano de Souza, A., et al. 2005, A&A, 442, 567

Ekström, S., et al. 2008, A&A, 478, 467

ESA 1997, The Hipparcos and Tycho Catalogues, ESA SP-1200

Gigas, D. 1986, A&A, 165, 170

Girardi, L., et al. 2000, A&AS, 141, 371

Glindemann, A., et al. 2003, Proc. SPIE, Interferometry for Optical Astronomy II, ed. Wesley A. Traub, 4838, 89

Gratton, R., et al. 2004, ARA&A, 42, 385

Gray, R. O. 1988, JRASC, 82, 336

Gray, D. F. 2005, The observation and analysis of stellar photosphere (3rd ed.; Cambridge: Cambridge Univ. Press)

Grevesse, N., & Sauval, A. J. 1998, Space Sci. Rev., 85, 161

Gulliver, A. F., Hill, G., & Adelman, S. J. 1994, ApJ, 429, L81

Hanbury Brown, R., Davis, F., & Allen, L. R. 1974, MNRAS, 167,121

Hanbury Brown, R., et al. 1974, MNRAS, 167,475

Hardorp, J., & Strittmatter, P. A. 1968, ApJ, 151, 1057

Hayes, D. S. 1985, in Calibration of Fundamental Quantities, ed. D. S. Hayes, L. E. Pasinetti, & A. G. D. Philip (Dordrecht: Reidel), 225

Heiter, U. 2002, A&A, 381, 959

Hill, G., Gulliver, A. F., & Adelman, S. J. 2004, in IAU Symp. 224, The A-Star Puzzle, ed. J. Zverko, J. Ziznovsky, S. J. Adelman, & W. W. Weiss (Cambridge: Cambridge Univ. Press), 35

Hoffleit, D. & Warren, W. H., Jr 1991, Bright Star Catalogue (5th Rev. ed.; New Haven: Yale Univ. Obs.)

Holweger, H., et al. 1986, A&A, 155, 88

Holweger, H. 1992, in The Atmospheres of Early-Type Stars, ed. U. Heber & C. S. Jeffery (Berlin: Springer), 48

Holweger, H., & Stürenburg, S. 1993, in IAU Colloq. 138, Peculiar versus Normal Phenomena in A-type and Related Stars, ed. M. M. Dworetsky, F. Castelli, & R. Faraggiana (San Francisco: ASP), 356

Iben, I. J. 1967, ARA&A, 5, 571

Ilijić, S., et al. 1998, CoSka, 27, 461

Jennison, R. C. 1958, MNRAS, 118, 276

Johnson, J. A. 2002, ApJS, 139, 219

Kamp, I., & Paunzen, E. 2002, MNRAS, 335, L45

Kervella, P., et al. 2003, A&A, 408, 681

Kervella, P., et al. 2004, A&A, 413, 251

Kurucz, R. L. 1993, CD-ROM 13, ATLAS9 Stellar Atmosphere Programs and 2 km/s grid (Cambridge: SAO)

Kurucz, R. L., & Bell, B. 1995, CD-ROM 23, Atomic Line Data (Cambridge: SAO)

Kurucz, R. L. 2005, Mem. Soc. Astron. Italiana Suppl., 8, 14

Lane, B. F., Boden, A. F., & Kulkarni, S. R. 2001, ApJ, 551, L81

Maeder, A., & Meynet, G. 2000, ARA&A, 38, 142

Mérand, A., Bordé, P., & Coudé du Foresto, V. 2005, A&A, 433, 1155

Meynet, G., & Maeder, A. 1997, A&A, 321, 465

Monnier, J. D., et al. 2007, Science, 317, 342

Moultaka, J., et al. 2004, PASP, 116, 693

Mozurkewich, D., et al. 2003, ApJ, 126, 2502

Nordgren, T. E., et al. 1999, AJ, 118, 3032

Nordgren, T. E., Sudol, J. J., & Mozurkewich, D. 2001, AJ, 122, 2707

Paunzen, E., et al. 1999, A&A, 345, 597

Peterson, D. M. 1969, SAO Spec Rep, 391

Peterson, D. M., et al 2004, SPIE, 5491, 65

Peterson, D. M., et al. 2006a, ApJ, 636, 1087

Peterson, D. M., et al. 2006b, Nature, 440, 896

Petrie, R. M. 1964, Publ. Dom. Astrophys. Obs. Victoria, 12, 317

Pietrinferni, A., et al. 2006, AJ, 612, 168

Pietrinferni, A., et al. 2006, AJ, 642, 797

Pourbaix, D., et al. 2005, Catalogue of Spectroscopic Binary Orbits, 9th ed., `http://cdsweb.u-strasbg.fr/viz-bin/Cat?V/122`

Pradhan, A., et al. 1995, BAAS, 27, 841

Press, W. H., et al 1986, Numerical recipes in C (2nd ed.; Cambridge: Cambridge Univ. Press)

Reiners, A., & Royer, F. 2004, A&A, 428, 199

Richichi, A., Percheron, I., & Khristoforova, M. 2005 A&A, 431, 773

Robinson, F. J., et al. 2005, MNRAS, 362, 1031

Ryan, S., et al 1991, AJ, 102, 303

Sackmann, I. -J. 1970, A&A, 8, 76

Sadakane, K., & Nishimura, M. 1981, PASJ, 33, 189

Sandage, A. R., & Schwarzschild, M. 1952, ApJ,116, 463

Shao, M., et al. 1988, ApJ, 327, 905

Sneden, C. 2004, Mem. Soc. Astron. Italiana, 75, 267

Spiegel, E. A., & Zahn, J. P. 1992, A&A, 265, 106

Takeda, Y., Kawanomoto, S., & Ohishi, N. 2007, PASJ, 59, 245

Takeda, Y., Kawanomoto, S., & Ohishi, N. 2008, ApJ, 678, 446

Talon, S., et al. 1997, A&A, 322, 209

ten Brummelaar, T. A., et al. 2005, ApJ, 628, 453

Thévenin, F., & Idiart, T. P. 1999, ApJ, 521, 753

Torres, G., et al. 2002, AJ, 124, 1716

Vakili, F., et al. 1998, A&A, 335, 261

van Belle, G. T., et al. 2006, ApJ, 637, 494

Van Hamme, W. 1993, AJ, 106, 2069

Venn, K. A., & Lambert, D. L. 1990, ApJ, 363, 234

von Zeipel, H. 1924, MNRAS, 84, 655

Walker, N. 1965, Observatory, 85, 245

Yoon, J., et al. 2006, Proc. SPIE, Advances in Stellar Interferometry, ed. Monnier, J. D., Schöller, M., & Danchi, W. C., 6268, 626848

Yoon, J., et al. 2007, PASP, 119,437

Yoon, J., et al. 2008, ApJ, 681, 570

Zahn, J. -P. 1992, A&A, 256, 115